RELIABILITY AND MODE CONTROL OF (GaAl)As VISIBLE SEMICONDUCTOR LASERS

BY

TOSHIRO HAYAKAWA

APRIL 1984

RELIABILITY AND MODE CONTROL

OF

(GaAl)As VISIBLE SEMICONDUCTOR LASERS

BY

TOSHIRO HAYAKAWA

APRIL 1984

DOC
1984
9
電気系

ABSTRACT

This thesis describes on the fundamental properties, reliability and mode characteristics of (GaAl)As stripe-geometry double-heterostructure lasers emitting in the visible wavelength region. The main purpose of the present study is to extend the emission wavelength of semiconductor lasers to shorter wavelengths, and control mode characteristics of these devices.

Long-term reliability problems depending on the emission wavelength and the operating ambient are investigated by using conventional oxide-defined stripe-geometry devices. The facet oxidation, which proceeds faster in the shorter wavelength range, is examined in detail with a scanning Auger electron microscope. The utility of facet coating for suppressing the facet oxidation especially in the visible wavelength region and an improvement in mounting procedure are presented.

The v-channeled substrate inner stripe (VSIS) visible lasers on p-GaAs substrates are developed. In consequence of the transverse-mode stabilization by a built-in optical waveguide which is self-aligned with an internal current channel, VSIS lasers reproducibly provide a stable fundamental transverse and single longitudinal mode operation up to 20 mW/facet cw. The rather poor quality of the active layer grown on top of the Te-doped cladding layer is improved in the VSIS laser by the reverse growth sequence of the active and Te-doped cladding layers using p-type GaAs as a substrate for the first time; that is, the Te-doped cladding layer is grown "on top of" the active layer instead of "under" the active layer in conventional lasers on n-type substrates. This improvement suppresses the degradation and results in the high reliability of VSIS lasers. Results of accelerated life tests and the statistical characterization are presented for the devices emitting at 780 nm. The influences of the Te-doped cladding layer on the quality of the active layer and laser properties are discussed

based on the results of photoluminescence and Al-profiles in the active layer. Longitudinal-mode behavior which depends on the device structure is described.

The low-current-threshold behavior of VSIS lasers emitting below 750 nm, which agrees with the theoretical calculation, is presented. The cause of the increase in the threshold current of conventional lasers on n-GaAs substrates is discussed. The temperature dependence of the threshold current is measured for devices emitting in the wavelength range of 781-697 nm and is compared with the calculated results by the model of carrier leakage due to unconfined carriers in the active layer. The factors which determine the threshold-temperature sensitivity are examined based on the calculated results. It is shown that lifetimes of visible lasers emitting at 740 nm can be improved by setting the thicknesses of the cap layer and the substrate at appropriate values according to the calculation in order to reduce the active layer stress caused by the bonding process.

The dependence of mode characteristics on the built-in refractive index difference is studied for VSIS lasers by the introduction of a large-optical-cavity structure. The longitudinal mode and noise properties are investigated, and the effect of the current distribution upon the transverse mode is determined by measuring the temperature dependence of the far-field pattern.

Finally, conclusions of the present study are summarized.

ACKNOWLEDGMENT

The author whishes to thank Professor Hiroyuki Matsunami for his guidance and encouragement. He is grateful to Professor Akira Kawabata for his useful suggestions and criticism on the manuscript. He also acknowledges Professor Akio Sasaki for a critical reading of the manuscript and valuable comments.

Acknowledgment is made to Sharp Corporation for permission to publish this thesis. He would like to express his deep gratitude to senior management people of the company, especially Dr. Tadashi Sasaki, Senior Executive Vice President, Mr. Kohsaku Okano, Senior Executive Director, Mr. Minoru Miyuki, Corporate Director and General Manager of Central Research Laboratories, and Dr. Tomio Wada, Deputy General Manager of Central Research Laboratories for their continuous support and hearty encouragement. He is also grateful to Mr. Toshiki Hijikata, Department General Manager of the First Devices Research Department and Mr. Seiki Yano, Manager, for their guidance and fruitful advice during the course of this work.

Special thanks are due to Mr. Saburo Yamamoto for device fabrication and co-operation in various experiments as a leader of the device fabrication group. Thanks are also due to Mr. Hiroshi Hayashi for crystal growth and fabrication of laser diodes, and due to Mr. Nobuyuki Miyauchi and Takahiro Suyama for sample preparation and various measurements. He is grateful to all other research members of the First Devices Research Department for useful discussion and experimental support.

CONTENTS

ABSTRACT i
ACKNOWLEDGMENT iii

I. INTRODUCTION 1
References 5

II. IMPROVEMENTS IN LIFETIMES OF CONVENTIONAL OXIDE-DEFINED STRIPE-GEOMETRY LASERS 7
2-1. Introduction 7
2-2. Fabrication Procedure and Characteristics 8
2-3. Facet Degradations 10
2-3-1. Experimental 10
2-3-2. Dark defects formation at mirror facets 13
2-3-3. Facet oxidation 16
2-3-4. Auger analysis of the oxidized facets 20
2-4. Deterioration of In Solder 24
2-5. Summary 30
References 31

III. V-CHANNELED SUBSTRATE INNER STRIPE LASERS FOR VISIBLE EMISSION 33
3-1. Introduction 33
3-2. Structure and Fabrication Process 35
3-3. Modal Characteristics 37
3-4. Reliability 45
3-4-1. Degradation in conventional DH lasers due to the Te-doped n-(GaAl)As cladding layer 45
3-4-2. Accelerated reliability test 49
3-4-3. Modal stability with aging 56
3-4-4. Photoluminescence study 59
3-5. Summary 64
References 65

IV. PROPERTIES OF VISIBLE LASERS EMITTING BELOW 750 nm 67
4-1. Introduction 67
4-2. Threshold Current 69
4-2-1. Experimental Results 69
4-2-2. Influence of the Te-doped cladding layer 71
4-2-3. Theoretical calculation 72
4-2-4. Causes of the increase in threshold 77
4-3. Temperature Dependence of Threshold Current 80
4-3-1. Experimental results 80
4-3-2. Theoretical calculation 85
4-3-3. Discussion 90
4-4. Lifetime 94
4-5. Summary 99
References 101

V. MODE CHARACTERISTICS OF LARGE-OPTICAL-CAVITY V-CHANNELED SUBSTRATE INNER STRIPE LASERS 104
5-1. Introduction 104
5-2. Design and Fabrication 105
5-3. Mode Characteristics 110
5-4. Summary 121
References 122

VI. CONCLUSIONS 125

LIST OF PUBLICATION

I. INTRODUCTION

The first injection lasing in GaAs diodes was independently reported by Hall et al. of GE, Nathan et al. of IBM and Quist et al. of Lincoln Laboratory in 1962,[1-3] which followed the first demonstration of the Ruby and He-Ne lasers in 1960[4] and 1961,[5] respectively. These injection lasers which comprised of a single semiconductor have been designated as homostructure lasers. A drawback of the homostructure lasers was that the threshold current density J_{th} for lasing was extremely high ($>5\times10^4$ A/cm^2) at room temperature. Thus operation of homostructure lasers usually required low temperatures ($\lesssim 77$ K) and very short and low duty cycle current pulses.

Reduction in J_{th} at room temperature was accomplished by the introduction of the heterostructure in order to obtain close confinement of carriers and the optical field. The single-heterostructure (SH) lasers which consisted of n-GaAs, p-GaAs, and p-(GaAl)As resulted in low J_{th}(300 K) of $\sim10^4$A/cm^2 in 1969.[6-8] The higher energy gap and the lower refractive index of the p-(GaAl)As layer than the p-GaAs active region in the SH provides the energy barrier for injected electrons and prevent the optical field from spreading into the p-(GaAl)As layer.

In 1970, Hayashi, Panish, and their co-workers achieved further reduction in J_{th}(300 K) to 1.6×10^3 A/cm^2 and succeeded in continuous-wave (cw) operation at room temperature by using the double-heterostructure (DH), where the p-GaAs active layer was sandwiched by the n- and p-(GaAl)As cladding layers.[9,10] In the same year, Alferov et al. independently reported cw operation of a DH laser at 300 K.[11] The DH provides the effective confinement of both electrons and holes injected into the active layer, and the optical field confinement at the both sides of the active layer. Since this first success in cw lasing at room temperature, the (GaAl)As/GaAs DH lasers have been extensively investigated for putting semiconductor lasers into practical uses. A major application

of injection lasers in 1970's was a light source in fiber optic communication system.[12)]

Stripe geometry that restricts the current along the junction plane was incorporated into DH lasers for the purpose of reducing the operating current and obtaining the fundamental transverse mode operation. Consequently, the relatively low operating current (I_{th} <200 mA) and a single filament emission were realized. Stripe geometry was first applied to homostructure GaAs lasers by Dyment,[13)] and Dyment and D'Asaro[14)] in 1967, and many types of stripe-geometry DH lasers were developed in early 1970's.[15-20)]

There existed a serious problem to be solved before semiconductor lasers could be used in practical systems; that is, short lifetime. Lifetimes of diode lasers at the initial stage of development were less than 1 min. A lot of efforts had to be paid to extend operating lifetime since the operating condition of laser diodes is usually very severe: high current density (>10^3 A/cm^2) and high optical power density (>10^5 W/cm^2). As a result of extensive investigations, reliability of (GaAl)As DH lasers has been markedly improved to attain the extraporated room temperature lifetime exceeding 10^6 h until the end of 1970's.[21,22)] All the processes in the device fabrication from epitaxial growth to mounting procedure and also operating conditions may affect the reliability of laser diodes. Because of such a complex feature, detailed mechanisms of degradation are not fully elucidated even at present. In addition, reliable lasers have only been realized in the rather restricted infrared wavelength region of 810-850 nm. These devices have been developed for fiber-optic communication systems.[23)] The narrow emission wavelength range of light sources, however, limits the number of wavelengths which can be used in the wavelength-division multiplexing communication system. Therefore, it is important to study the reliability and degradation phenomena of lasers emitting at wavelengths other than those mentioned above and extend the available wavelength range of light sources.

In recent years, there arises an increasing demand for short

wavelength visible laser diodes to be used in information processing applications such as audio and video disk playback systems and laser beam printers. Since the collimated spot size of laser beam with a lens becomes smaller in proportion to wavelength,[24] shorter wavelength is more advantageous for some applications. The sensitivity of the photo-conductive material also increases with decreasing wavelength in laser beam printers. Thus shortening the emission wavelength of laser diodes is important and desired.

The first visible spectrum lasing at 710 nm was reported for Ga(AsP) homostructure lasers by Holonyak and Bevacqua in 1962.[25] Several III-V mixed crystals, such as (GaAl)As,[20,26-29] (InGa)(AsP)[30-32] and Ga(AsP),[33,34] have been studied for DH lasers to date. Among these mixed crystals, (GaAl)As is the most promising material for visible semiconductor lasers at present, since (GaAl)As closely lattice matches to GaAs for the whole composition range and does not have the miscibility gap, which has been reported in the (InGa)(AsP) system.[35] However, present (GaAl)As visible lasers emitting below 800 nm suffer from the significant decrease in lifetimes with decreasing emission wavelength.[28,29] Moreover, below 750 nm the threshold current considerably increases[27,29] and becomes more sensitive to ambient temperature.[36]

In addition to high reliability, transverse mode stability of laser diodes is required both in fiber-optic communications and information processing. It has been found that transverse mode are unstable in most of conventional stripe-geometry lasers in which light is confined to the current injected region due to gain distribution.[37-39] The waveguiding induced by gain distribution is reffered to as "gain guiding".[40] Various designs of stripe lasers have been developed in which a built-in two-dimentional dielectric waveguide is formed to provide optical guiding along the junction plane[41-46]; this is reffered to as "index guiding". These index-guided lasers operate in a stable fundamental transverse mode and can also provide a single longitudinal mode when devices are prop-

erly fabricated. However, their fabrication procedure usually includes sophisticated etching,[42] Zn diffusion,[41] or mask alignment.[43-46] The mask alignment process is required especially to align the current injection stripe with the built-in optical waveguide. Thus most of index-guided lasers reported so far are not considered to be suitable for mass production; the facility of mass production is an essential factor particularly in consumer electronics applications, such as audio and video disk playback systems.

Another problem in index-guided lasers is that those lasers which operate on a single longitudinal mode show instability with optical feedback.[47,48] It is desirable that the longitudinal mode properties of index-guided lasers can be controlled and optical feedback induced instability is suppressed.

In this thesis, study is carried out on the fundamental properties, reliability, and mode characteristics of (GaAl)As stripe-geometry DH lasers emitting in the visible wavelength region. Attention is paid mainly to the subjects which are pointed out to be investigated in this chapter. In Chapter II, reliability problem in (GaAl)As DH lasers is investigated for the wide range of emission wavelength of 760-880 nm using conventional oxide-defined stripe-geometry devices. An improvement in the mounting procedure is also presented. In Chapter III, the newly developed v-channeled substrate inner stripe (VSIS) lasers on p-GaAs substrates are described. Mode characteristics and reliability of devices emitting at 780 nm are studied in detail. Chapter IV describes the wavelength dependence of the threshold current and the threshold-temperature sensitivity in VSIS lasers emitting below 750 nm. These results are compared with the theoretical calculation. It is also shown that lifetimes of lasers emitting at 740 nm can be improved by reducing the active layer stress due to the bonding process. In Chapter V, the dependence of transverse and longitudinal mode characteristics on the built-in refractive-index difference is investigated for VSIS lasers by the introduction of the large-optical-cavity structure. Finally, conclusions of the present study are summarized in Chapter VI.

References

1) R.N.Hall, G.E.Fenner, J.D.Kingsley, T.J.Soltys and R.O.Carlson, Phys. Rev. Lett. 9, 366 (1962).

2) M.I.Nathan, W.P.Dumke, G.Burns, F.H.Dill,Jr., and G.J.Lasher, Appl. Phys. Lett. 1, 62 (1962).

3) T.M.Quist, R.H.Rediker, R.J.Keys, W.E.Krag, B.Lax, A.L. McWhorter, and H.J.Zeiger, Appl. Phys. Lett. 1, 91 (1962).

4) T.H.Maiman, Nature 187, 493 (1960).

5) A.Javan, W.B.Bernett,Jr., and D.R.Herriott, Phys. Rev. Lett. 6, 106 (1961).

6) M.B.Panish, I.Hayashi, and S.Sumski, IEEE J. Quantum Electron. QE-5, 210 (1969).

7) I.Hayashi, M.B.Panish, and P.W.Foy, IEEE J. Quantum Electron. QE-5, 211 (1969).

8) H.Kressel and H.Nelson, RCA Rev. 30, 106 (1969).

9) M.B.Panish, I.Hayashi, and S.Sumski, Appl. Phys. Lett. 17, 109 (1970).

10) I.Hayashi, M.B.Panish, P.W.Foy, and S.Sumski, Appl. Phys. Lett. 17, 109 (1970).

11) Zh.I.Alferov, V.M.Andreev, D.Z.Garbuzov, Yu.V.Zhilyaev, E.P. Morozov, E.L.Portnoi, and V.G.Trofim, Sov. Phys. Semicond. 4, 1573 (1971).

12) D.Botez and G.J.Herskowitz, Proc. IEEE 68, 689 (1980).

13) J.C.Dyment, Appl. Phys. Lett. 10, 84 (1967).

14) J.C.Dyment and L.A.D'Asaro, Appl. Phys. Lett. 11, 292 (1967).

15) L.A.D'Asaro, J. Lumin. 7, 310 (1973).

16) H.Kan, H.Namizaki, M.Ishii, and A.Ito, Appl. Phys. Lett. 27, 138 (1975).

17) J.C.Dyment, L.A.D'Asaro, J.C.North, B.I.Miller, and J.E.Ripper, Proc. IEEE 60, 726 (1972).

18) H.Yonezu, I.Sakuma, K.Kobayashi, T.Tamejima, M.Ueno, and Y. Nannichi, Jpn. J. Appl. Phys. 12, 1585 (1973).

19) T.Tsukada, H.Nakashima, J.Umeda, S.Nakamura, N.Chinone, R.Ito, and O.Nakada, Appl. Phys. Lett. 20, 344 (1972).

20) K.Itoh, M.Inoue, and I.Teramoto, IEEE J. Quantum Electron. QE-11, 421 (1975).

21) R.L.Hartman, N.E.Schumaker, and R.W.Dixon, Appl. Phys. Lett. 31, 756 (1977).

22) M.Ettenberg, J. Appl. Phys. 50, 1195 (1979).

23) T.G.Giallorenzi, Proc. IEEE 66, 744 (1978).

24) H.Kubota, Wave Optics, (Iwanami, Tokyo, 1971) (in Japanese).

25) N.Holonyak,Jr., and S.F.Bevacqua, Appl. Phys. Lett. 1, 82 (1962).

26) B.I.Miller, J.E.Ripper, J.C.Dyment, E.Pinkas, and M.B.Panish, Appl. Phys. Lett. 28, 403 (1971).

27) H.Kressel and F.Z.Hawrylo, Appl. Phys. Lett. 28, 598 (1976).

28) T.Kajimura, J. Appl. Phys. 51, 908 (1980).

29) M.Wada, K.Itoh, H.Shimizu, and I.Teramoto, IEEE J. Quantum Electron. QE-17, 776 (1981).

30) R.Chin, N,Holonyak,Jr., R.M.Kolbas, J.A.Rossi, D.L.Rossi, D.L. Keune, and W.O.Groves, J. Appl. Phys. 49, 2551 (1978).

31) S.Mukai, H.Yajima, and J.Shimada, Jpn. J. Appl. Phys. 20, L729 (1981).

32) M.Shimura, A.Fujimoto, H.Yasuda, and S.Yamashita, Jpn. J. Appl. Phys. 21, L338 (1982).

33) H.Kressel, G.H.Olsen, and C.J.Nuese, Appl. Phys. Lett. 30, 249 (1977).

34) R.Chin, N.Holonyak,Jr., H.Shichijo, W.O.Groves, D.L.Keune, and J.A.Rossi, J. Appl. Phys. 48, 3991 (1977).

35) G.B.Stringfellow, J.Cryst. Growth 58, 194 (1982).

36) T.Hayakawa, S.Yamamoto, H.Hayashi, T.Sakurai, and T.Hijikata, IEEE J. Quantum Electron. QE-17, 2205 (1981).

37) T.L.Paoli, IEEE J. Quantum Electron. QE-12, 770 (1976).

38) R.Lang, IEEE J. Quantum Electron. QE-15, 718 (1979).

39) N.Chinone, J. Appl. Phys. 48, 3237 (1979).

40) D.D.Cook and F.R.Nash, J. Appl. Phys. 46, 1660 (1975).

41) H.Namizaki, H.Kan, M.Ishii, and A.Ito, J. Appl. Phys. 45, 2785 (1974).

42) T.Tsukada, J. Appl. Phys. 45, 4899 (1974).

43) R.D.Burnham and D.R.Scifres, Appl. Phys. Lett. 27, 510 (1975).

44) K.Aiki, M.Nakamura, T.Kuroda, and J.Umeda, Appl. Phys. Lett. 30, 649 (1977).

45) P.A.Kirby and G.H.B.Thompson, J. Appl. Phys. 47, 4578 (1976).

46) D.Botez, Appl. Phys. Lett. 33, 872 (1978).

47) K.Peterman and G.Arnold, IEEE J. Quantum Electron. QE-18, 543 (1982).

48) G.Arnold, Proc. 7th Eur. Conf. Opt. Commun. 10.4-1 (1981).

II. IMPROVEMENTS IN LIFETIMES OF CONVENTIONAL OXIDE-DEFINED STRIPE-GEOMETRY LASERS

2-1. Introduction

Reliability of (GaAl)As DH lasers has been markedly improved to attain extrapolated room temperature lifetimes exceeding 10^6 h.[1,2] These long-lived lasers have been realized by eliminating dislocations in the active layer.[3] It has been also found that a dielectric facet coating suppressed the facet deterioration and was of great advantage in realizing stable operation of lasers.[4-6] Yonezu et al. investigated degradation phenomena of uncoated lasers in detail and demonstrated that the facet degradation played an important role at all stages of degradation in uncoated lasers.[7] On the contrary, Nash et al. reported that Al_2O_3 facet coatings were capable of eliminating an initial temporarily saturable mode of degradation, but were ineffective in preventing a long-term degradation.[8-10] Thus the degradation originating in the mirror facet still has ambiguous features.

It has been reported that the thermal and electrical resistances of (GaAl)As DH lasers increased during aging tests owing to the deterioration of In solder.[11-14] Fujiwara et al. have shown that the increase in thermal resistance could be eliminated by using Au-eutectic alloy solder instead of In solder.[13] However, they observed that the stress caused in the bonding process was larger in lasers bonded with Au-eutectic alloy solder than in lasers bonded with In solder. It is desirable to prevent both the stress due to the bonding process and the deterioration of In solder.

In this chapter, degradation phenomena of $Ga_{1-x}Al_xAs$/$Ga_{1-y}Al_yAs$ DH lasers with AlAs mole fraction x of 0-0.17 in the active layer are investigated using scanning electron microscope

(SEM) and scanning Auger electron microscopy. Results of life tests conducted in an ambient of both dry and humid nitrogen are compared. There are few reports on the native oxide of (GaAl)As although many studies have been made of the native oxides of GaAs, which are formed by different techniques such as the thermal, anodic, and plasma oxidation.[15-18] Since Al can affect the oxidation process, an anodic oxide of $Ga_{0.8}Al_{0.2}As$ is prepared and the composition profiles of the anodic oxide and the native oxide formed at facets are compared. The process of the facet oxidation is examined on the basis of the results of these Auger experiments. Finally, the author demonstrates that long-lived lasers bonded with In solder can be produced by eliminating the deterioration of In solder during aging in addition to by using Al_2O_3 facet coatings.

2-2. Fabrication Procedure and Fundamental Characteristics

Laser diodes employed here are conventional oxide-defined stripe-geometry DH lasers. The structure of the device is schematically illustrated in Fig.1. At first, by usual liquid phase epitaxy (LPE) technique, DH layers consisting of an n-$Ga_{1-y}Al_yAs$ (Si doped, $n \sim 0.5\text{-}1\times10^{18}$ cm^{-3}, $\sim$1 μm thick), an n-$Ga_{1-x}Al_xAs$ (Si doped, $n \sim 1\times10^{18}$ cm^{-3}, $\sim$0.2 μm thick), a p-$Ga_{1-y}Al_yAs$ (Ge doped, $p \sim 0.5\text{-}1\times10^{18}$ cm^{-3}, $\sim$1 μm thick), and a p-GaAs cap layer (Ge doped, $p \sim 1\times10^{18}$ cm^{-3}, $\sim$0.5 μm thick) were grown successively on an n-GaAs substrate (Si doped, $n \sim 2\times10^{18}$ cm^{-3}) with dislocation density less than 10^3 cm^{-2}. Then Al_2O_3 was deposited on the cap layer by chemical vapor deposition and a stripe was opened by standard photolithographic technique. Next, a shallow Zn diffusion ($\sim$0.2 μm in depth) through the stripe was carried out, followed by metallization. The metallization is described in detail in §2-4. The stripe width was 6 μm and

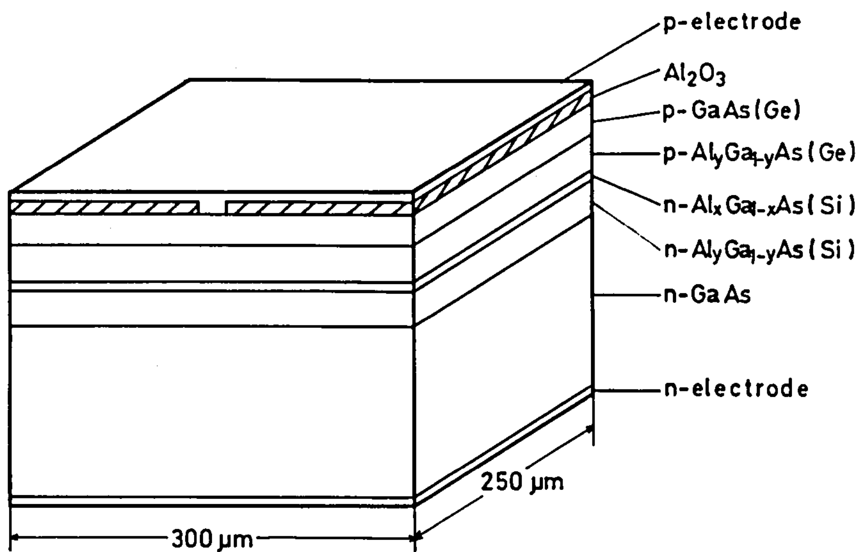

Fig. 1 Schematic structure of oxide-defined stripe-geometry laser.

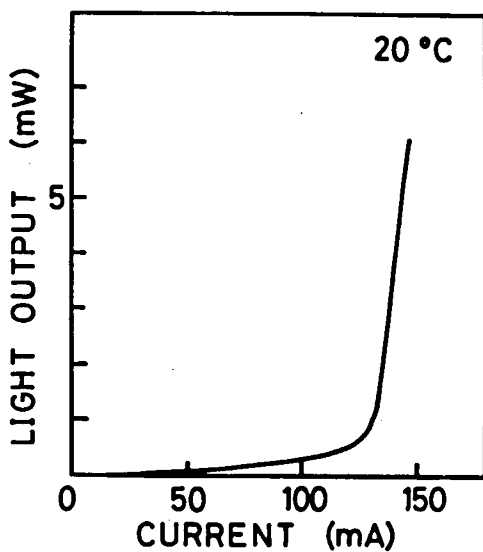

Fig. 2 Light output versus current characteristic.

the cavity length was 250 μm. A diode chip was mounted on a copper heat sink with In solder in an n-side-up style. AlAs mole fraction in the active layer was varied from 0 to 0.17 keeping the heterojunction step height ($\Delta x = y - x$) approximately constant at ∿0.3. Some lasers were fabricated with Al_2O_3 facet coatings deposited by electron beam evaporation.

cw threshold currents are in the range of 120±20 mA at 20°C. Figure 2 shows a typical light output-current curve, which exhibits good linearity up to 6mW/facet. The transverse mode is fundamental as shown in Fig.3. Side lobes observed in the far-field pattern parallel to the junction plane are due to the index-antiguiding nature in the gain-guided stripe-geometry lasers,[19] such as the oxide defined stripe structure. Oxide-stripe lasers used in the present study usually operate on multimodes with several longitudinal modes above 2 mW/facet as depicted in Fig.4. Multimodes operation is common to gain-guided lasers.[20]

2-3. Facet Degradations

2-3-1. Experimental

Life tests of laser diodes were carried out in a dry nitrogen ambient at 20°C. Some lasers were operated in a humid nitrogen ambient containing 100% RH water vapor at 20°C. cw output power was maintained at 5 mW/facet during operation. Crystalline defects formed in the stripe region were examined with a SEM in the electron beam induced-current (EBIC) mode. In the EBIC measurement, the primary electron beam energy and current were 15 kV and 10^{-6} A, respectively, which generates ∿10^{18} cm^{-3} electron-hole pairs. Deteriorated laser facets were observed with a Nomarski differential interference-contrast microscope and a SEM.

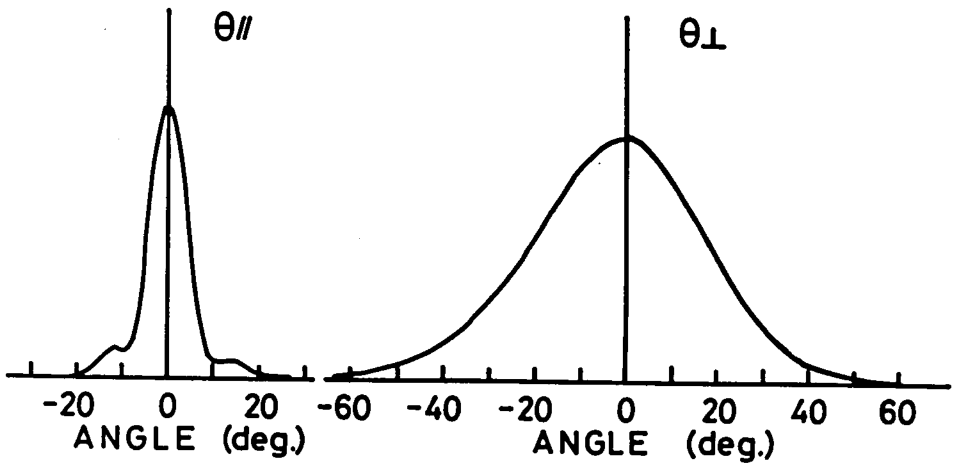

Fig. 3 Far-field distributions for parallel (//) and perpendicular (⊥) directions to the junction plane.

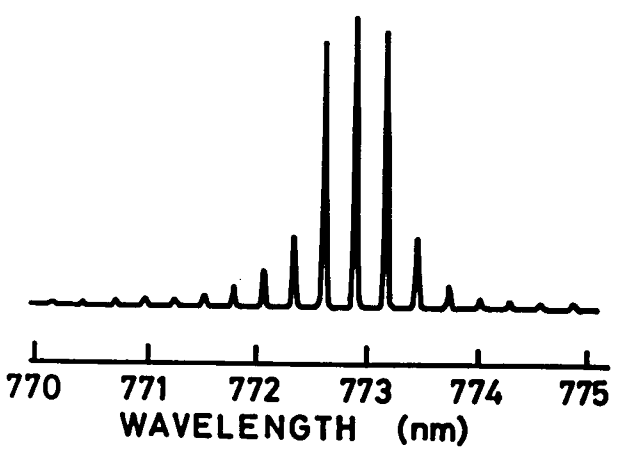

Fig. 4 Emission spectrum at 5 mW/facet.

Detailed analysis was performed with a scanning Auger electron microscope combined with in situ Ar sputter etching. The primary electron beam energy, current, and size were 10 kV, $3\text{-}5\times10^{-8}$ A, and 50 nm, respectively. In the case of depth-profiling measurement, a primary beam was scanned within the area of $0.2\times5\ \mu m^2$ ($\perp J\times //J$). These parameters were carefully determined in order to attain high spatial resolution less than the active layer thickness (~0.2 μm) and avoid electron beam damages introduced in a sample. The modulation amplitude of the detector was set at 10 eV, the time constant at 0.3 sec, and the scanning rate at 2 eV/sec. The absorbed electron image (AEI) was employed to determine the position of the deteriorated region, since the deteriorated region can be observed as a dark region in the AEI.[21] Peak-to-peak values of Auger signals of KLL transitions for O (507 eV) and Al (~1400 eV), LMM transitions for Ga (~1070 eV) and As (~1230 eV) were used for the depth profiling. These peak-to-peak values were normalized and corrected for Auger sensitivity and differential sputtering, using the peak-to-peak signal ratios of the constituent elements in Ga_2O_3, GaAs, and $Ga_{0.67}Al_{0.33}As$ measured under the same conditions as those set for the depth profiling. During the depth profiling, minute Auger lines of Ga, Al, and As were measured at the modulation amplitude of 2 eV, the time constant of 3 sec, and the scanning rate of 0.1 eV/sec, after reducing the sputtering rate to 1/20 of that for the depth profiling. By changing the equipment parameters, it became possible to observe chemical shifts of Auger lines and obtain a depth profile at the same time.

For the purpose of comparing the composition profiles of deteriorated facets of lasers with that of anodically oxidized layer, an anodic oxide was grown on a LPE n-$Ga_{0.8}Al_{0.2}As$ layer, which was deposited on an n-GaAs substrate. $Ga_{0.8}Al_{0.2}As$ was anodized in an electrolytic solution (1% phosphoric acid buffered to pH=7.0 with a saturated solution of KOH) at a constant voltage of 25 V.

2-3-2. Dark defects formation at mirror facets

Figure 5 shows the dependence of degradation rate on AlAs mole fraction x in the active layer. Life tests were performed for lasers with x=0 ($\lambda \sim 890$ nm), 0.05 (~ 850 nm), 0.08 (~ 830 nm), 0.12 (~ 800 nm), and 0.17 (~ 770 nm), and revealed that the driving current increased approximately in proportion to the square root of operating time for uncoated lasers in all cases. Results of life tests demonstrate that the average degradation rate takes minimum value at x=0.08. It is shown in the following sections that the dominant degradation mechanism in the lasers with larger x is different from that in the lasers with smaller x.

Some lasers were examined with EBIC images of a SEM at different operating times more than 5×10^2 h. In the lasers with x larger than or equal to 0.05, no "dark defects" were observed in the stripe region. In the case of x=0, on the other hand, dark region defects (DRD's) and dark line defects (DLD's) were observed in the vicinity of the mirror facet, as shown in Fig.6. These dark defects were found in all EBIC images of the lasers with x=0 after more than 5×10^2 h operation, and appeared to extend with operating time. As seen in Fig.6, DLD's stretch from the DRD's formed in the stripe at the facet, and their directions are not always <100> or <110>; <100>- and <110>- oriented DLD's are usually observed in the rapidly degraded lasers.[3,22] In the lasers with x=0, Al_2O_3 facet coating has little effect on reducing the degradation rate, and the moisture does not enhance the degradation, as depicted in Fig.7. Dark defects were also observed in the EBIC images of these Al_2O_3-coated lasers after more than 5×10^2 h operation. Since Al_2O_3 facet coating is capable of preventing the facet from the oxidation and moisture enhances the facet oxidation, as will be demonstrated in the next section, dark defects at the mirror facet do not originate from the point defects due to the facet oxidation. Therefore, the mechanical damage introduced at the time of cleaving is possibly the origin of dark defects.

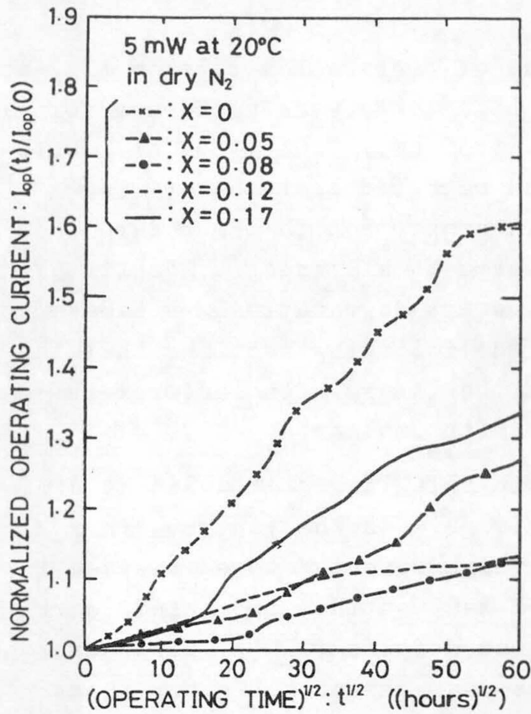

Fig. 5 Typical example of the change in operating current in uncoated lasers under 5-mW constant-optical-power operation at 20°C in a dry nitrogen ambient. Each curve represents an average degradation rate for different values of x, and operating currents are normalized by the initial values.

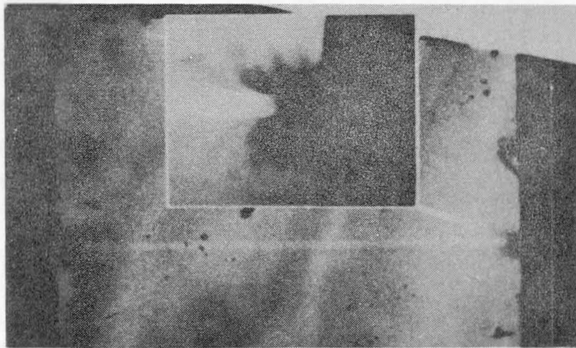

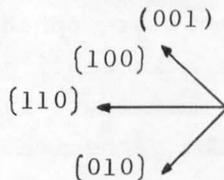

Fig. 6 An EBIC image of the laser with x=0 after 4×10^3 h-operation. A magnified image is also shown.

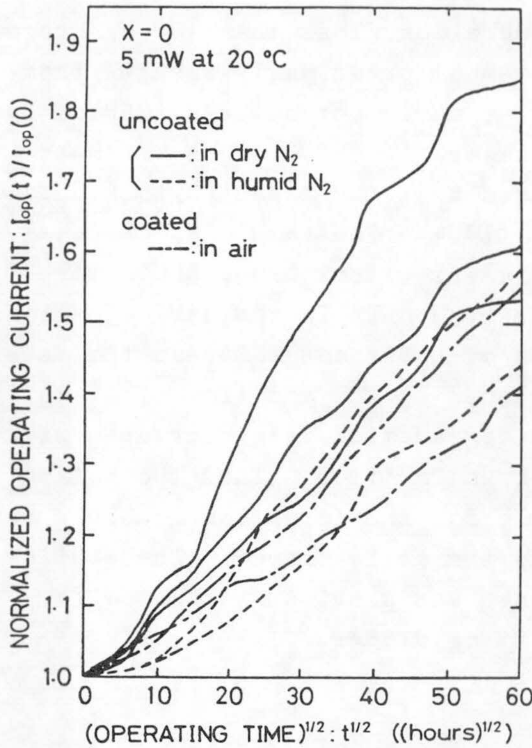

Fig.7 Typical examples of increase in operating currents of the lasers with x=0. Data are shown for uncoated lasers operated in an ambient of both dry and humid nitrogen, and lasers with Al_2O_3 facet coatings operated in air.

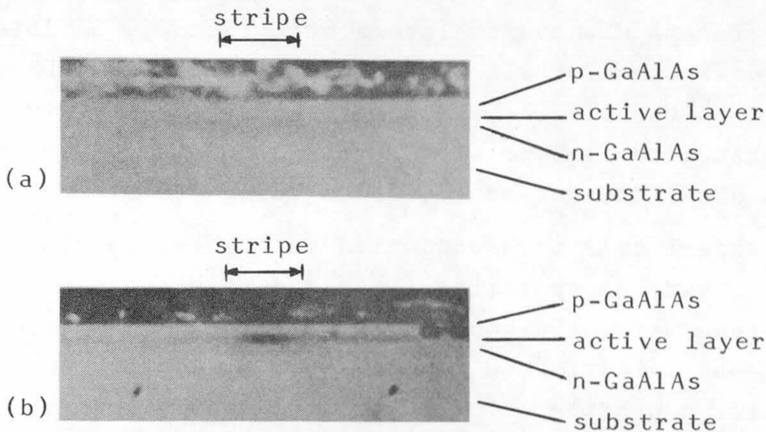

Fig.8 Photomicrographs of deteriorated facets of uncoated lasers with (a) x=0 and (b) x=0.17 after about 10^3-h operation at 5 mW/facet in a 20°C dry nitrogen ambient.

In addition, we found that the number of devices failing rapidly at the initial stage of operation, less than 10^2 h, decreased with increasing x. This improvement principally results from the decrease in the number of native dark spot defects (DSD's) by the addition of Al to the active layer.[3] EBIC images of these rapidly degraded lasers demonstrated that the lasers with x=0 failed mainly due to the formation of <100>-oriented DLD's.[3,22] However, in the rapidly degraded lasers with x$\geqq$0.08, DLD's were seldom observed and DSD's were observed only in the stripe region. In a similar manner, the formation of DLD's and DRD's at the facet in long-term degradation is suppressed by the addition of Al to the active layer and as a result, the degradation rate decreases with increasing x from 0 to 0.08, as shown in Fig.5. Thus the motion of dislocation which is responsible for the formation of DLD's and DRD's is prevented by adding Al to the active layer. The similar effect of Al for improving lifetimes was previously repoted for (GaAl)As heterojunction light emitting diodes.[23]

2-3-3. Facet oxidation

Mirror facets of uncoated lasers were found to be deteriorated after 10^3 h operation for all values of x. Facet deterioration was, however, more noticeable for the lasers with larger x, as shown in Fig.8. Deteriorated regions were dark brown in color but flat, without any mechanical damage, as confirmed using a SEM.

Auger experiments were conducted on the lasers with x=0, 0.08, and 0.17 after various operating times and revealed that the deteriorated regions were oxidized, as is well known[6,21] (see Fig.11). Thickness of the oxide formed at the facet was estimated from the depth composition profile, about which detailed discussion will be presented in §2-3-4. For this estimation, we took the sputtering rate of the deteriorated layer as that of the anodic oxide layer on GaAs; the sputtering rate of the anodically oxidized GaAs was measured to be 18 Å/min under the same conditions as those used in

the depth composition profiling. As depicted in Fig.9, the facet oxidation proceeds faster for larger x. Nevertheless, there still remains a doubt upon a causal relationship between the facet oxidation and the degradation in the device, such as an increase in the threshold current. Therefore, to ascertain the degree of responsibility of the facet oxidation for the laser degradation, life tests in a humid nitrogen ambient were conducted. The oxide formation is enhanced by about a factor of 10^2 in humid nitrogen. In addition, the lasers with Al_2O_3 facet coatings were also aged in air. These life tests were made on lasers with x=0, 0.08, and 0.17.

Aging curves are shown in Figs.7, 10(a), and 10(b) for x=0, 0.08, 0.17, respectively. As described in §2-3-2, both the moisture and facet coating exert little influence upon the degradation rate of x=0. An amazing result is that the degradation rate in a humid ambient is lower than that in a dry ambient in the case of x=0.08. Almost no degradation is observed in life test data for x=0.08 in a humid ambient, with the exception of a slight initial saturable mode of degradation. In the case of x=0.17, degradation was greatly accelerated by the moisture in the ambient. Al_2O_3 facet coatings almost perfectly suppress the degradation for x=0.08 and 0.17. It is clear from the above-mentioned results that the facet oxidation is responsible for the long-term degradation, and Al_2O_3 facet coatings have the remarkable effect of preventing the facet from the oxidation, in the lasers with x larger than 0.08.

However, the results for x=0.08 exhibit rather complicated aspects of degradation due to facet oxidation. In this case, the thickness of the oxide formed on the facet after 2×10^2 h operation in a humid ambient was found to be more than 1.3 μm. Thus the facet oxidation is enhanced by a factor of 10^2 or more by increasing the humidity in the operating ambient. For all that, the long-term degradation is suppressed by increasing the humidity and only the initial degradation, saturable less than 10^3 h, remains, as seen in Fig.10(a). Since the "thick" oxide formation is not responsible for the long-term degradation, the refractive index of the

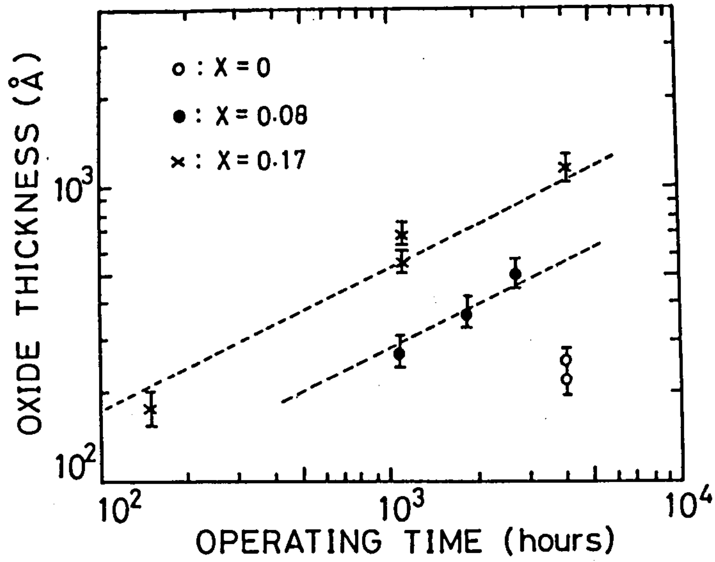

Fig.9 Estimated oxide thicknesses formed at the mirror facets of lasers with x=0, 0.08, and 0.17 as a function of operating time.

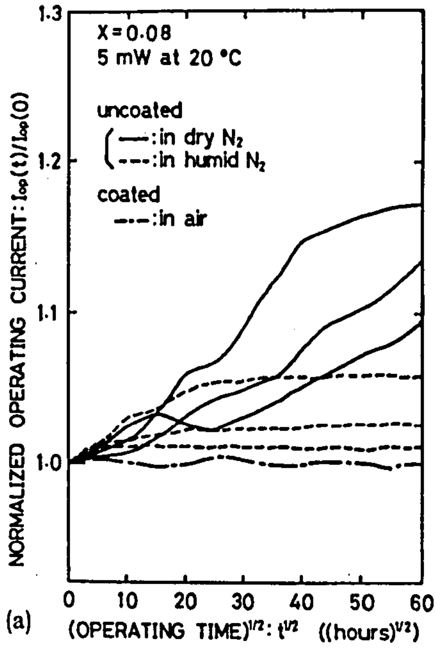

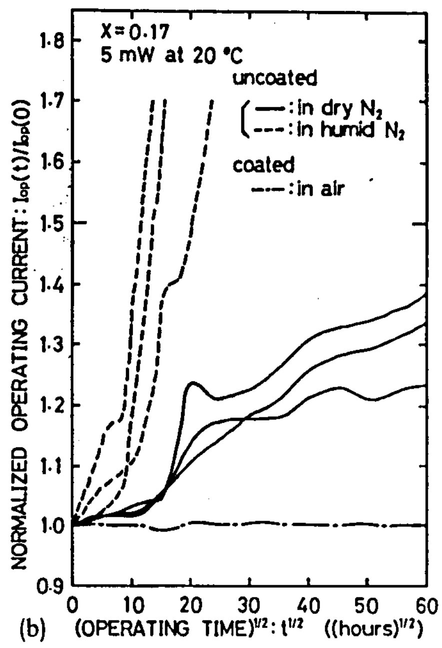

Fig.10 Typical examples of increase in operating currents of the lasers with (a) x=0.08 and (b) x=0.17. Data are shown for uncoated lasers operated in an ambient of both dry and humid nitrogen, and lasers with Al_2O_3 facet coatings operated in air.

native oxide which has been formed at the facet in lasers with x=0.08 through operation in a humid ambient, must be equal or very close to that of the active layer crystal $Ga_{0.92}Al_{0.08}As$, because the difference in refractive index between the oxide formed at the facet and the active layer crystal causes the increase in mirror transmission loss. The initial degradation possibly results from an increase in the nonradiative interface state density between the grown oxide and the active layer crystal[7] and therefore, saturates after the interface has been completely formed. Although the author could not find the compositional differences between the oxide formed in a dry ambient and that formed in a humid ambient by Auger experiments, it should be noted that the degradation due to the facet oxidation is considerably affected by the humidity of the operating ambient, as described above. Concerning the long-term degradation, almost all studies have been made of the lasers with x=0.05-0.08. Thus the difference in the humidity between the testing ambients may have drawn the contradictory conclusions on the role of facet oxidation in the long-term degradation, as previously reported by the several authors.[4-10]

2-3-4. Auger analysis of the oxidized facets

Depth composition profiles were investigated on the oxidized facets of lasers with x=0, 0.08, and 0.17. Depth profiles of the deteriorated regions in the lasers with x=0.08 and 0.17, operated for 2800 and 1100 h, respectively, are shown in Fig.11. The peak-to-peak Auger signal of O does not decrease to zero in the unoxidized crystal due to the limitation of the signal-to-noise ratio of the measuring system. However, the AlAs mole fraction in the unoxidized crystal seen in Fig.11 shows good agreement with that of the active layer crystal determined by electron probe microanalysis. This agreement demonstrates that a major portion of Auger signal comes from the active layer. The oxide thicknesses shown in Fig.9 are determined as the depths where the Auger signals of O decrease

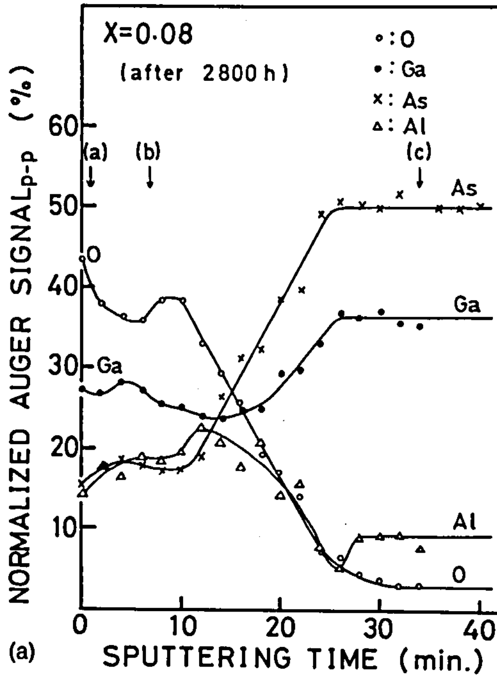

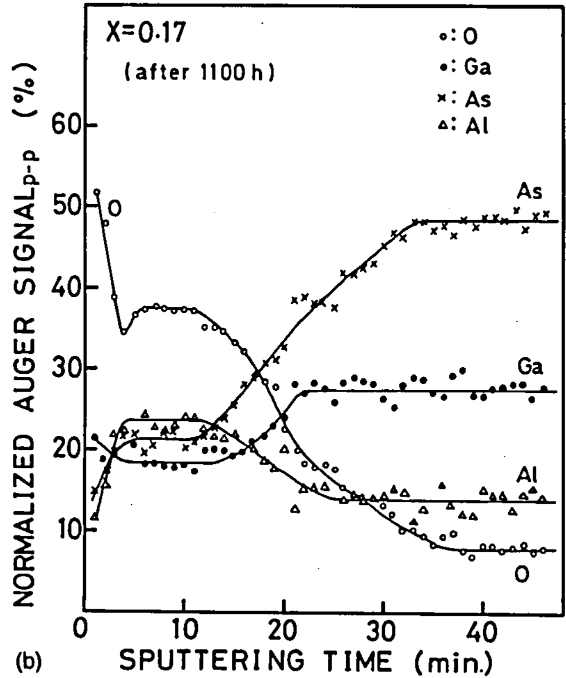

Fig.11 Auger depth profiles of the deteriorated mirror facets of the lasers with (a) x=0.08 and (b) x=0.17. Auger signals are normalized and quantitatively corrected, as described in §2-3-1.

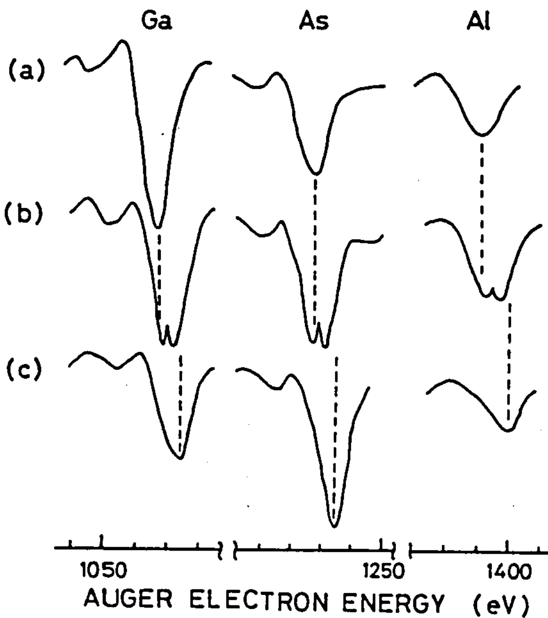

Fig.12 Auger lines of Ga, As, and Al corresponding to the points indicated by the marked arrows in Fig.11(a).

to the noise level.

The Auger lines corresponding to the points indicated by the arrows marked in Fig.11(a) are shown in Fig.12. It is clear from the chemical shifts that all the constituent elements are fully oxidized due to adsorbed O, from the surface to depths of several angstroms. Since all the lines are doublets as seen in Fig.12(b), all the elements are only partially oxidized in the oxide. Furthermore, the oxidized layer is As-deficient, as seen in Fig.11. These features were commonly observed in all lasers operated in both dry and humid ambients, independently of x.

The depth profile and the Auger lines of anodically oxidized $Ga_{0.8}Al_{0.2}As$ are shown in Fig.13. Since the depth profile is extremely similar to those of the oxidized laser-facets shown in Fig.11, the oxidation proceeds similarly in both cases. This comparative results is due to the fact that the Auger depth profiling was conducted only on active layer; by avoiding the effects of non-uniformity of the oxide thickness outside the active layer, we could obtain compositional profiles with high resolution in depth. It is seen from the chemical shifts in Auger lines shown in Fig.13 (b) that in the anodic oxide, As is not oxidized with the exception of adsorption of O at the surface, and Ga and Al are fully oxidized through the oxide. Highly oxidized As (possibly As_2O_5) might leach out of the oxide leaving Ga_2O_3, Al_2O_3, and residual unoxidized As. Excepting Al, similar phenomenon was reported on the thermally oxidized GaAs.[15] In the case of the facet oxidation, not only As but also Ga and Al are not fully oxidized and some portion of oxidized As leaches out of the oxide. This is attributed to a lack of an electrolyte and a relatively low temperature at which the facet oxidation proceeds. The process of the oxidation of (GaAl)As active layer can be explained by similarity to that for anodic or thermal oxide formation.[16]

One possible model is as follows. The oxide thickness increases approximately in proportion to the square root of the operating time in the range of oxide thickness more than 10^2 Å, as shown

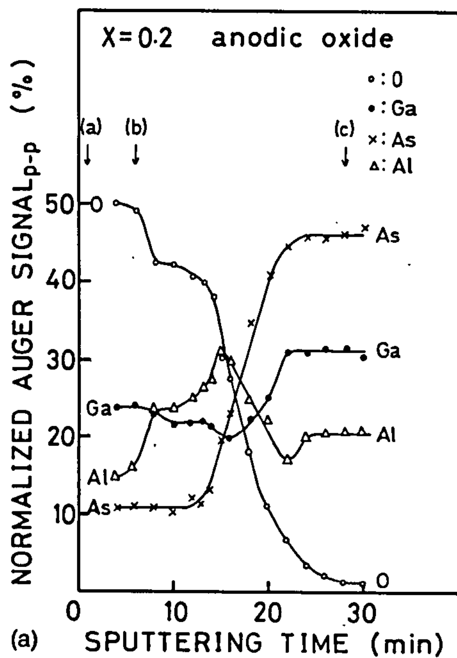

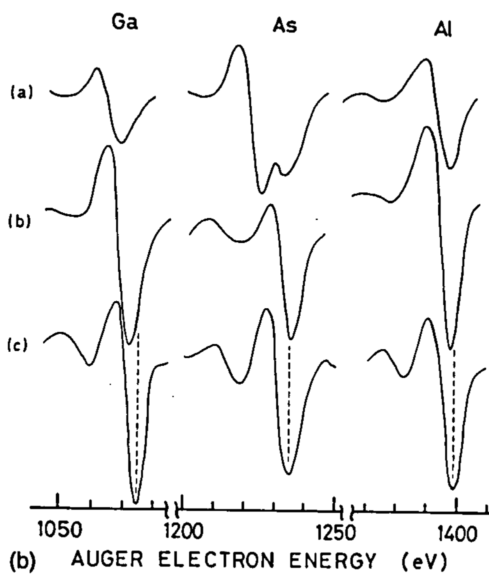

Fig.13 (a) An Auger depth composition profile and (b) Auger lines of an anodically oxidized $Ga_{0.8}Al_{0.2}As$.

in Fig.9, for the lasers with x=0.08 and 0.17. This indicates that the oxidation process is diffusion controlled in the oxide after more than a 10^2 Å thick oxide is formed. Since the slope of the oxide thickness versus operating time curves are almost the same for both x=0.08 and 0.17, the dependence of the oxide thickness on x has its origin in the initial stage of oxidation.[24] The oxidation rate is controlled by the interfacial reaction rate at the initial stage of oxidation, and Al is more readily oxidized than Ga. Consequently, the oxidation proceeds faster in lasers with larger x until the oxide thickness reaches $\sim 10^2$ Å.

Concerning the transition region from the oxide to the active layer crystal, a noticeable difference is observed between the lasers with x=0 and 0.08, and those with x=0.17. In the lasers with x=0 and 0.08 and also in the anodic oxide, the widths of transition region are almost equal for all the elements as shown in Figs.11(a) and 13(a), respectively. However, in the lasers with x=0.17, the transition regions are observed to be wider for As and O than Ga and Al, as shown in Fig.11(b). This difference may affect the nonradiative recombination rate at the transition region and as a result, may influence the initial saturable mode of degradation. With respect to these features further investigations are required.

2-4. Deterioration of In Solder

The p-side of the device used in the present study was metallized by evaporating Mo/Au onto it. These devices were bonded p-side down on Mo/Au evaporated Cu heat sinks using In solder. The structure of the device including the solder and heat sink is illustrated in Fig.14. Molybdenum was used as a barrier metal for preventing the In solder from reacting with GaAs and the Cu heat

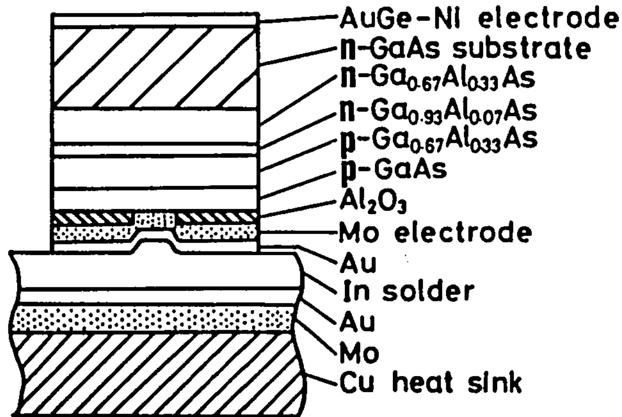

Fig.14 Schematic cross-section of device employed in the present study.

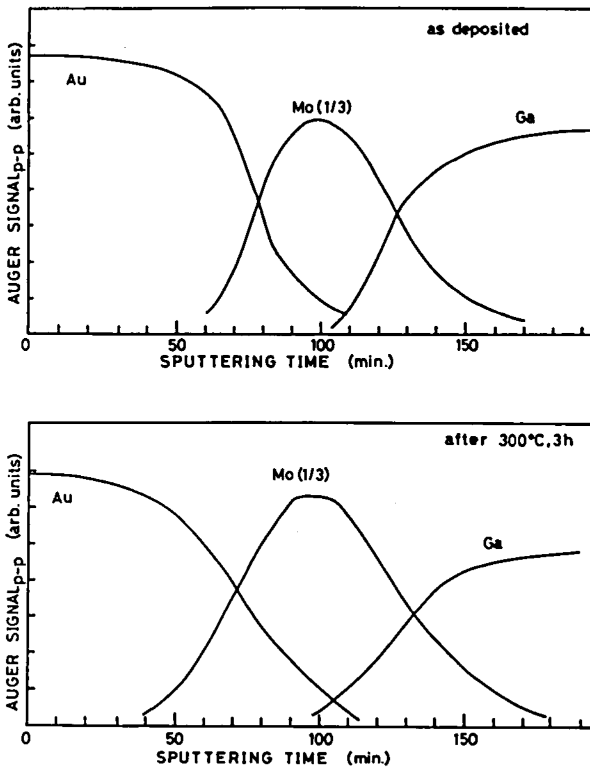

Fig.15 Auger depth compsi-tion profiles of Mo(~500 Å) /Au(~1000 Å) evaporated on GaAs (a) before and (b) after a heat treatment at 300°C for 3 h.

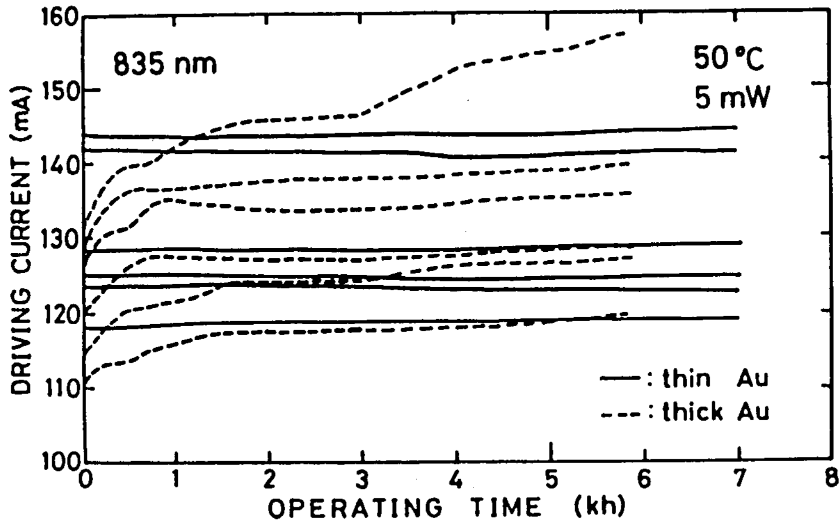

Fig.16 Aging results on devices with thin and thick Au on Cu heat sinks.

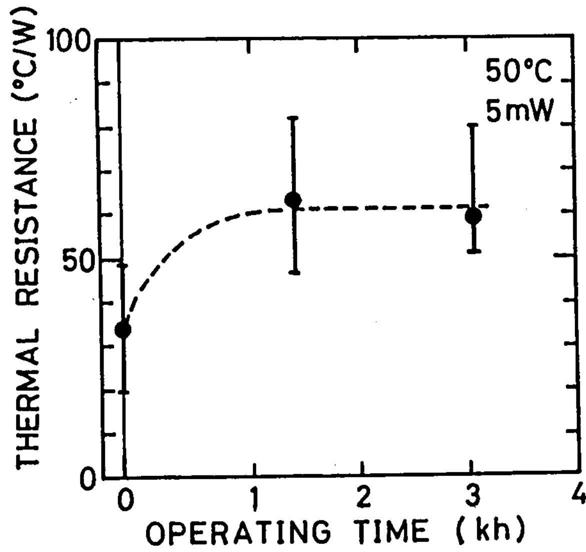

Fig.17 Change in thermal resistance of devices with thick Au on Cu heat sinks. Closed circles denote average values.

sink. The stability of Mo as a barrier metal is confirmed by the unchanged composition profile after a heat treatment at 300°C for 3 h in $\sim 10^{-6}$ torr vacuum as depicted in Fig.15.

Although it is necessary to evaporate Au onto Mo to prevent the oxidation of the Mo surface before bonding and wetting Mo with In, this Au forms intermetallic species with In. The author has eliminated the formation of intermetallic species between In and Au during aging by making the total thickness of Au evaporated onto Mo on both the GaAs cap layer and the Cu heat sink less than 1/10 of the thickness of the In solder. In this "thin Au" case, all Au dissolves into the In solder while the In is in the molten state during the bonding process, and therefore no further intermetallic species are formed.

For comparison, devices with " thick Au" on Cu heat sinks were prepared. In this case, the thickness of AU on Cu heat sinks was almost the same as that of the In solder, while the thickness of Au on the laser chip was kept small. The two types of devices with thin and thick Au on the Cu heat sinks were operated at 50°C in air. Both mirror surfaces of the devices used for this life test were coated with Al_2O_3 by electron beam evaporation. Emission wavelengths were ~ 835 nm. During the aging, the optical output was maintained at 5 mW/facet. Typical changes in the driving current are shown in Fig.16. The driving currents of the devices with thick Au increase significantly for the first 10^3 h and then increase more slowly. In contrast, the devices with thin Au show almost no degradation for more than 5×10^3 h.

The thermal resistance of the lasers was measured during the life test and no change was observed in the devices with thin Au. The thermal resistance of the devices with thick Au increased by a factor of 2 in the initial 10^3 h and did not change after that, as shown in Fig.17. The observed increase in the driving current can be attributed to the increase in junction temperature due to the increase in thermal resistance. In addition, the average increase in junction temperature of about 9°C in the initial 10^3 h of aging

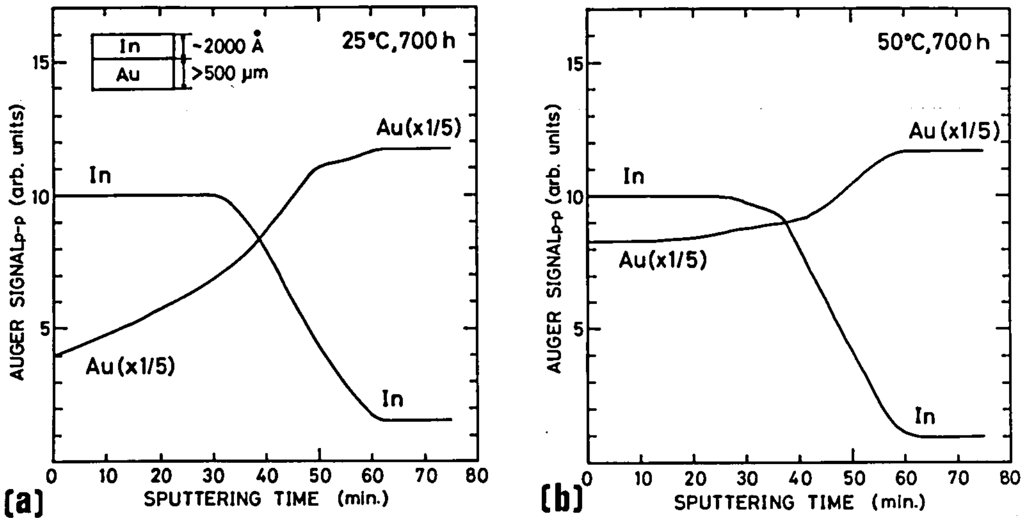

Fig.18 Auger depth composition profiles of samples for simulation after storage for 700 h at (a) 25 and (b) 50°C. Auger signals were corrected for Auger sensitivity and differential sputtering of Ar ion etching used in measurements.

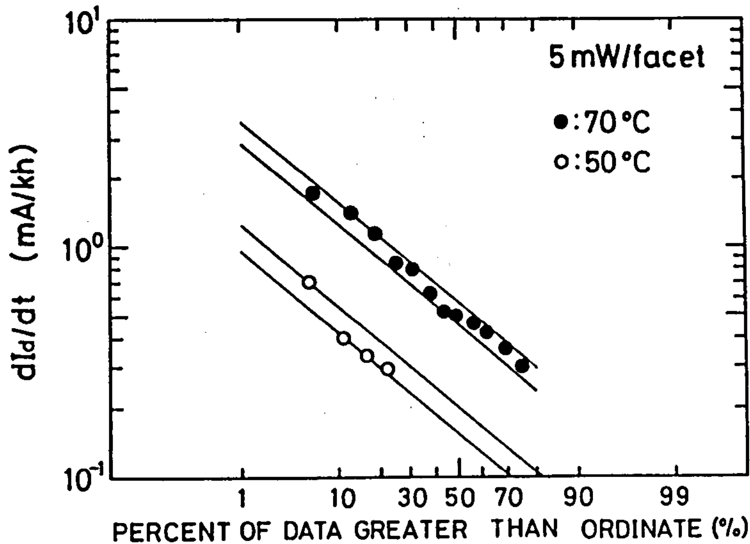

Fig.19 Log-normal plots of rate of increase of driving current during 5 mW/facet operation at 50 and 70°C.

accelerates the degradation. Thus, the degradation rates of the devices with thick Au are greater than the devices with thin Au even after thermal resistance stops increasing. The degradation of thermal resistance described above occured during storage at 50°C without operation.

The author also examined the depth composition profiles of the In solder on thick Au after 10^3 h's storage at 50°C. It was found that Au diffused into In and the composition of the solder was In:Au$\cong$2:1 in the vicinity of the solder surface. In this case, it would take a long time for the diffusion of Au to end because of the thick In (~2.4 μm). Thus, a simulation method was employed for further investigating the formation of intermetallic species between In and Au. The samples were Au foils (more than 500 μm thick) on which 2000 Å thick In was evaporated at room temperature. These samples were stored for 700 h at 25 and 50°C and then their depth composition profiles were examined. These profiles shown in Fig.18 lead to the following conclusions.

(1) The formation of intermetallic species between In and Au takes place by the diffusion of Au into In.

(2) This diffusion of Au proceeds faster as the temperature is raised,i.e., it is thermally activated.

(3) The formation of intermetallic species proceeds until the ratio of Au to In becomes about 4, at least at 50°C. However, thermal resistivity of the solder is considered to increase until the ratio of Au to In becomes 1/2, after which it remains constant.

To estimate operating lifetime, 17 and 15 laser diodes with thin Au on the Cu heat sinks were operated at 5 mW/facet at 50 and 70°C, respectively. Unlike the uncoated lasers described in §2-3-1, the driving current of these improved lasers with Al_2O_3 facet coatings increases in proportion to operating time. The rate of increase in the driving current dI_d/dt were measured over 5×10^3h. The degradation rate, which is smaller than 0.3 mA/kh, cannot be measured because of the limit of accuracy of the aging system. Log-normal plots of dI_d/dt are shown in Fig.19. The median values

of dI_d/dt are 0.175 and 0.52 mA/kh and the mean values of dI_d/dt are 0.13 and 0.38 mA/kh, for operations at 50 and 70°C, respectively. These values give an activation energy of 0.52 eV, which is very close to the values of 0.56 and 0.57 eV reported for (GaAl)As light emitting diodes[25] and 0.5 eV recently reported for (GaAl)As laser diodes.[26] When the operating lifetime is defined as the time at which the increase in the driving current reaches 50 mA, the mean time to failure at 25°C is estimated to be 1.9×10^6 h.

2-5. Summary

The Author has shown that the degradation rate of uncoated lasers took minimum value at x=0.08. The degradation in the lasers with x below 0.08 is mainly caused by the dark defects formation in the vicinity of the mirror surfaces. These defects possibly originated in the mechanical damage by cleaving, and the defect motion which causes these macroscopic defects is suppressed by adding Al to the active layer. The dominant degradation mechanism in the region of x=0.08-0.17, thus including visible spectrum range, is facet oxidation, which is enhanced with increasing x. Auger analysis revealed that the native oxide formed at the facet was only partially oxidized and the enhanced oxidation for larger x resulted from an initial stage of oxidation, where the oxidation was controlled by the interfacial reaction rate. The faster oxidation rate of Al than Ga has an influence on the oxide thickness at this initial stage, and the oxidation is diffusion controlled in the oxide after more than 10^2 Å of oxide is formed. The degradation by facet oxidation is also affected by the humidity of the operating ambient, and this effect may have caused the contradictory results of the role of the facet oxidation previously reported. Degradation in the region of x=0.08-0.17 is effectiveiy suppressed with the Al_2O_3 facet coatings. The author has produced long-lived

(GaAl)As DH lasers bonded with In solder by eliminating the deterioration of In solder during aging together with Al_2O_3 facet coatings. As a result of the accelerated reliability tests at 50 and 70°C, the mean time required for a 50 mA increase in the driving current of these long-lived devices emitting at ∿835 nm was estimated to be 1.9×10^6 h at 25°C in operation at 5 mW/facet.

References

1) R.L.Hartman, N.E.Schumaker, and R.W.Dixon, Appl. Phys. Lett. 31, 756 (1977).

2) M.Ettenberg, J. Appl. Phys. 50, 1195 (1979).

3) H.Yonezu, T.Kamejima, M.Ueno, and I.Sakuma, Jpn. J. Appl. Phys. 13, 1679 (1974).

4) I.Ladany, M.Ettenberg, H.F.Lockwood, and H.Kressel, Appl. Phys. Lett. 30, 87 (1977).

5) Y.Shima, N.Chinone, and R.Ito, Appl. Phys. Lett. 31, 625 (1977).

6) T.Yuasa, M.Ogawa, K.Endo, and H.Yonezu, Appl. Phys. Lett. 32, 119 (1978).

7) H.Yonezu, K.Endo, T.Kamejima, T.Torikai, Y.Yuasa, and T.Furuse, J. Appl. Phys. 50, 5150 (1979).

8) F.R.Nash, R.L.Hartman, N.M.Denkin, and R.W.Dixon, J. Appl. Phys. 50, 3122 (1979).

9) F.R.Nash and R.L.Hartman, J. Appl. Phys. 50, 3133 (1979).

10) F.R.Nash, R.L.Hartman, T.L.Paoli, and R.W.Dixon, Appl. Phys. Lett. 35, 905 (1979).

11) H.Kressel, M.Ettenberg, and I.Ladany, Appl. Phys. Lett. 32, 305 (1978).

12) S.Ritchie, R.F.Godfrey, B.Wakefield, and D.H.Newman, J. Appl. Phys. 49, 3127 (1978).

13) K.Fujiwara, T.Fujiwara, K.Hori, and M.Takusagawa, Appl. Phys. Lett. 34, 668 (1979).

14) K.Fujiwara, H.Imai, T.Fujiwara, K.Hori, and M.Takusagawa, Appl. Phys. Lett. 35, 861 (1979).

15) I.Shiota, N.Miyamoto, and J.Nishizawa, J. Electrochem. Soc. 124, 1405 (1977).

16) C.W.Wilsen, R.W.Kee, and K.M.Geib, J. Vac. Sci. Technol. 16, 1434 (1979).

17) C.C.Chang, B.Schwarz, and S.P.Murarka, J.Electrochem. Soc. 124, 922 (1977).

18) R.P.H.Chang, A.J.Polak, D.L.Allara, C.C.Chang, and W.A. Landford, J. Vac. Sci. Technol. 16, 888 (1979).

19) W.Streifer, R.D.Burnham, and D.R.Scifres, IEEE J. Quantum Electron. QE-18, 856 (1982).

20) W.Streifer, D.R.Scifres, and R.D.Burnham, Appl. Phys. Lett. 40, 305 (1982).

21) T.Kajimura, J. Appl. Phys. 51, 908 (1980).

22) P.Petroff and R.L.Hartman, Appl. Phys. Lett. 23, 469 (1973).

23) M.Ettenberg, H.Kressel, and H.F.Lockwood, Appl. Phys. Lett. 25, 82 (1974).

24) B.E.Deal and A.S.Grove, J. Appl. Phys. 36, 3770 (1965).

25) S.Yamakoshi, T.Sugahara, O.Hasegawa, Y.Toyama, and H. Takanashi, IEDM Tech. Digest 642 (1978).

26) H.Imai, K.Hori, M.Takusagawa, and K.Wakita, J. Appl. Phys. 52, 3167 (1981).

III. V-CHANNELED SUBSTRATE INNER STRIPE LASERS FOR VISIBLE EMISSION

3-1. Introduction

In recent years, visible light emitting semiconductor lasers in the 700-nm wavelength region are beginning to be used as light sources in a variety of information processing systems, such as audio-disk players and laser printers. For these applications, a laser diode is required to have a low threshold current, provide a fundamental transverse mode operation, and be guaranteed high reliability. Low threshold current and a fundamental transverse mode operation have been realized in transverse junction stripe (TJS) structures[1] and in terraced substrate (TS) structures,[2] in the 700-nm wavelength region. It is not difficult to fabricate (GaAl)As visible lasers using techniques employed for (GaAl)As infrared lasers because of the close lattice matching between (GaAl)As and GaAs for the whole composition range x in the $Ga_{1-x}Al_xAs$ system. Thus, reliability is a key factor for the practical use of (GaAl)As visible lasers. However, the statistical characterization of the reliability of visible lasers has not yet been sufficiently performed. In addition, long-term stable operation without any significant change in optical and electrical performances is necessary for practical applications.

In this chapter, the author describes on the highly mode-stabilized performance and high reliability of newly developed v-channeled substrate inner stripe (VSIS) lasers emitting in the visible wavelength range.

Transverse mode of the VSIS laser is stabilized by a built-in optical waveguide, which is self-aligned with an internal current confining channel. There have been many reports on both theore-

tical[3-6] and experimental[7-11] studies of longitudinal-mode behavior in transverse-mode stabilized semiconductor lasers. Gain suppression in nonlasing resonant modes[7-11] and hysteresis phenomena in the lasing-wavelength-versus-dc-current or temperature characteristics[7,8,11] have been observed in several transverse-mode stabilized lasers which operate on a single longitudinal mode. These phenomena may be explained by the inhomogeneous gain profile in the spectral region, as demonstrated by Yamada et al.[3-6] It is also possible that gain suppression occurs due to the spatial hole burning effect, which depends on the structure of laser diode, as discussed by Seki et al.[7] In particular, with respect to the gain suppression in TJS lasers, contradictory experimental results were reported, that is, no gain suppression (Ref.3) and gain suppression (Ref.8). Therefore, longitudinal-mode behavior in transverse-mode stabilized semiconductor lasers still has not been fully elucidated. In this chapter, the author presents the longitudinal-mode behavior in VSIS lasers, which depends on the structural factor of the device.

In the VSIS laser, the degradation which arises from the rather poor quality of the Te-doped cladding layer[12,13] is suppressed by growing the Te-doped cladding layer on the active layer using the p-type substrate, which is different from conventional lasers where it is grown on the n-GaAs substrate followed by the growth of the active layer. Improved lifetimes of VSIS lasers emitting at 780 nm are evaluated statistically based on the results of accelerated reliability tests. Stability of modal characteristics with operating time is also examined during the life test. Photoluminescence study is performed in order to clarify the effects of the Te-doped cladding layer on the quality of the active layer.

3-2. Structure and Fabrication Process

A schematic view and a cross sectional SEM photograph of a VSIS laser are shown in Fig.1. The VSIS laser is fabricated by a two-step liquid-phase epitaxy technique. In the first growth, an n-GaAs (Te-doped, $n\sim6\times10^{18}$ cm^{-3}, 0.6 μm thick), which acts as an internal current confining layer, is grown on a (100) oriented p-GaAs substrate (Zn-doped, $p\sim1\times10^{18}$ cm^{-3}). After the first growth, a v-shaped channel (4 μm wide and 1 μm deep) is etched in the <110> direction by using conventional photolithography. In the second growth, DH layers consisting of a p-$Ga_{1-y}Al_yAs$ (Mg or Zn doped, $p\sim1\times10^{18}$ cm^{-3}, 0.15 μm thick outside the v-channel), a $Ga_{1-x}Al_xAs$ active layer (0.08 μm thick), and an n-$Ga_{1-y}Al_yAs$ (Te-doped, $n\sim1\times10^{18}$ cm^{-3}, 1 μm thick), and an n-GaAs cap layer are grown successively, followed by the metallization. An Al_2O_3 coating is made to both mirror surfaces by electron beam evaporation. Laser chips are mounted on Mo/Au coated Cu heat sinks with In solder n-side down.[14)]

The internal current confinement is provided by the p-n-p structure outside the v-channel. This p-n-p structure behaves like a phototransistor since the n-GaAs current confining layer absorbs the emitted light from the active layer. If the confining layer were p-GaAs, the minority carriers (electrons) generated by optical absorption would diffuse away from the confining layer unless the thickness of the confining layer were thicker than the electron diffusion length (>1 μm).[15)] Thus, the confining layer would be charged with majority carriers, and the n-p-n structure would turn on. Therefore, p-GaAs would not work as a current confining layer.

On the other hand, if the confining layer is a heavily doped n-GaAs as in the VSIS laser, the confining layer is not charged up since the diffusion length of the minority carrier holes in n-GaAs is several times smaller than the thickness of the confining layer.

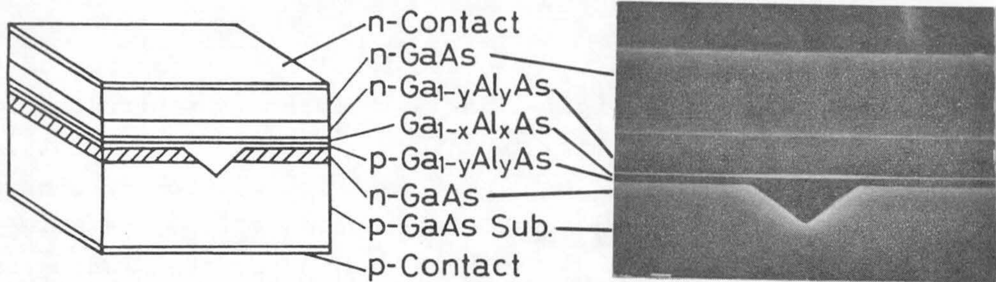

Fig. 1 Schematic view and cross sectional SEM photograph of VSIS laser.

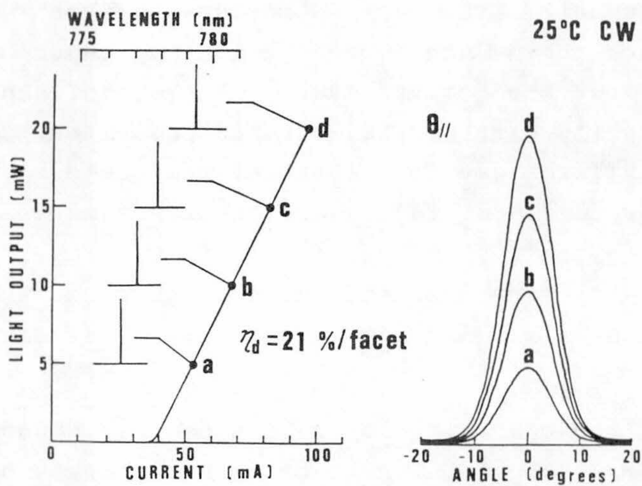

Fig. 2 cw light output-current curve and the corresponding lateral far-field patterns and spectra.

Thus, internal current confinement is readily realized in the VSIS laser although optical absorption takes place. (GaAl)As with appropriate AlAs mole fraction is transparent to the lasing light and therefore, would be more effective as the confining layer. However, when (GaAl)As is used for the confining layer, the more sophisticated structure is necessary[16] since the second growth upon (GaAl)As is very difficult due to the oxidation of (GaAl)As.

3-3. Modal Characteristics

In the VSIS laser, the transverse mode is stabilized by the built-in "complex" refractive-index difference parallel to the junction plane, in a manner similar to a channeled substrate planar (CSP) laser,[17,18] where the built-in refractive-index difference is caused by the fact that outside the channeled region, the evanescent tails of the lasing light reach the current confining layer, which is absorptive and has higher refractive index than DH layers. In the VSIS laser, however, the real part of the built-in refractive-index difference rather than loss difference makes a major contribution to the mode stabilization since the external differential quantum efficiency is higher than that of a CSP laser with a wider channel width (>5 μm)[19] than that of the VSIS laser (4 μm), shown in Fig. 2. In a laser with a narrower channel, a larger fraction of light spreads out into the absorptive region outside the channel in the lateral direction. Thus, when the transverse mode is mainly stabilized by the loss difference, the external differential quantum efficiency decreases with decreasing channel width. It is of great advantage that a narrow channel of about 2 μm is self-aligned with a built-in optical waveguide without a mask-alignment process in the VSIS laser. As a result, the current is more strongly confined than the CSP laser. The distribution of the injected carrier density in the waveguide, which causes the gain

distribution, is considered to be one of the causes for the relatively high external differential quantum efficiency.

The cw threshold current of the VSIS laser with a cavity length of 250 μm and emission wavelength in the range of 725-790 nm is typically in the range of 40±5 mA at room temperature. The near-field half-width in the parallel direction is as narrow as 2 μm, and the laser beam is nonstigmatic, resulting from the index guiding. Fundamental transverse and single longitudinal mode operation can be maintained up to 20 mW/facet cw, as shown in Fig.2. In consequence of the self-aligned structure, the yield and reproducibility of the highly mode-stabilized devices, shown here, are remarkably high.

A hysteresis is observed in the lasing-wavelength-versus-dc-current characteristics at constant heat sink temperature, as demonstrated in Fig.3. As the driving current is increased, the lasing wavelength traces a different path than when the driving current is decreased. This hysteresis phenomena have been reported for several lasers, such as a CSP laser,[7)] a buried heterostructure (BH) laser,[10)] and a plano-convex waveguide (PCW) laser.[11)]

Figure 4 shows a typical example of variation in intensities of lasing and nonlasing modes with dc current in a regular VSIS laser emitting at 780 nm. Here, these regular VSIS lasers are denoted as type I devices. AlAs mole fractions in the active and cladding layers of these regular lasers are 0.15 and 0.45, respectively. The thickness of the active layer is 0.08 μm and that of the cladding layer outside the v-channel is 0.15 μm. These are important factors which determine the magnitude of refractive-index difference parallel to the junction plane. The thickness of cladding layer outside the v-channel also affect the degree of lateral current spreading in the p-type cladding layer, which determines the effective width of the current channel. The active layer is doped with Mg ($p=1-2\times10^{18}\ cm^{-3}$). For nonlasing modes in Fig.4, +1 and -1 denote the nearest neighboring modes whose wave-

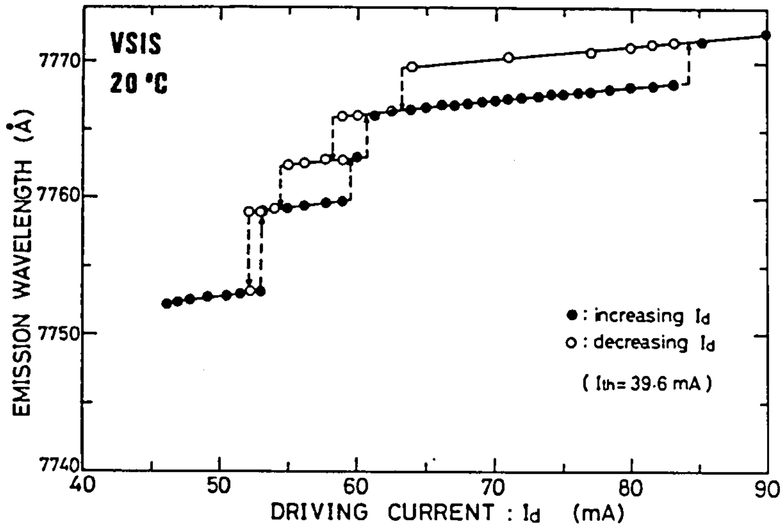

Fig. 3 Hysteresis observed in the lasing-wavelength-versus-dc-current characteristic under constant heat sink temperature.

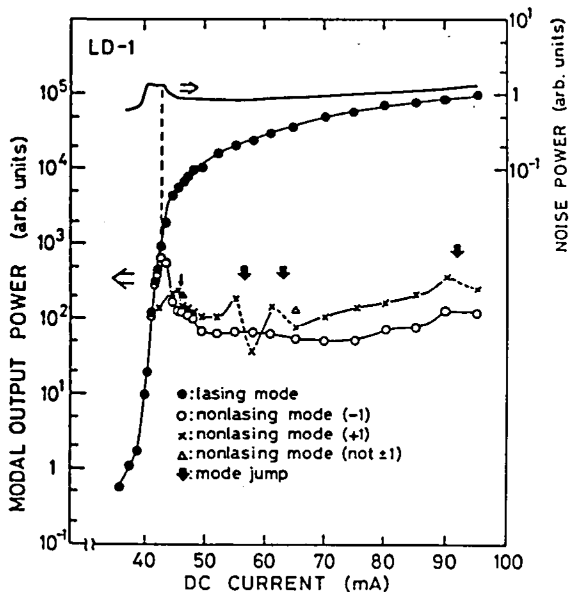

Fig. 4 One example of intesities of lasing and non-lasing modes as a function of dc current for a type I device. Intensity of intrinsic spectral noise at 1.5 MHz is also shown in the figure.

lengths are longer and shorter than the lasing wavelength, respectively. Other nonlasing modes are also indicated when they are stronger than +1 and -1 modes.

As seen in Fig.4, the intensity of the strongest nonlasing mode decreases above $1.08 \times I_{th}$, where the light output power is 0.93 mW/facet. This suppression of the nonlasing mode is as strong as in the 1.6-μm (InGa)(AsP)/InP laser reported by Itaya et al.[9] and stronger than already reported in (GaAl)As lasers.[3,7,8] It should be noted that Figs.3 and 4 are results for lasers with a heavily doped p-type active layer (Mg=$1-2 \times 10^{18}$ cm^{-3}), and similar phenomena were observed in VSIS lasers with an undoped active layer like the CSP laser.[3] It is important to note that the strong gain suppression and hysteresis phenomena occur in the laser with a heavily doped active layer. Gain suppression was also reported in a TJS laser, which has a heavily doped active layer.[8] The hysteresis phenomena and the suppression of nonlasing modes shown in Figs.3 and 4 are evidences of a highly mode-stabilized laser.

Suppression of the nonlasing modes was found to be incomplete in the VSIS laser around the longitudinal mode jump, as shown in Fig.4. This feature is illustrated in Fig.5, where the strongest nonlasing mode is indicated by an arrow. A considerable decrease of the nonlasing mode intensity at the short wavelength side of the lasing mode is observed at a certain current level (Fig.5(a)). As the driving current is increased, the position of the strongest nonlasing mode shifts to longer wavelengths until it reaches the nearest long wavelength neighbor of the lasing mode (Figs.5(a) and 5(b)). The intensity of the strongest nonlasing mode gradually increases with current until the mode jump takes place, whereupon it suddenly decreases. In the VSIS laser, similar to the BH laser,[10] the lasing wavelength jumps to the nearest neighboring mode above the current at which the ratio of the intensity of the lasing mode to that of the strongest nonlasing mode is about 100. In addition, the decrease of the nonlasing mode intensity near the lasing mode

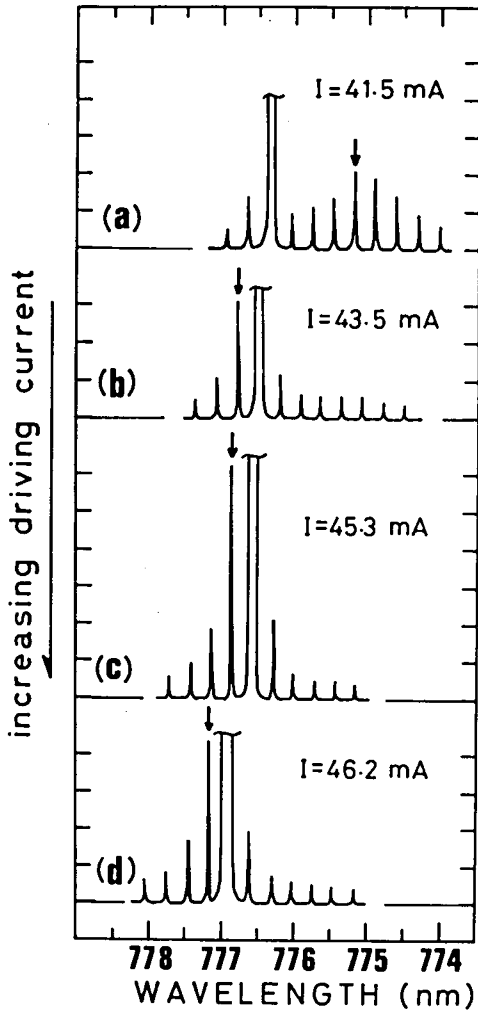

Fig. 5 Change in spectra of nonlasing modes around the lasing peak with increasing driving current. The strongest nonlasing mode is indicated by an arrow.

is observed only in the short wavelength side of the lasing mode. These characteristics are different from the CSP laser, in which the lasing mode jumps to the fourth nearest neighboring mode even at the high current levels where the ratio of the intensity of the lasing mode to that of strongest nonlasing mode is more than 100, and the decrease of the nonlasing mode is observed in both sides of the lasing mode, as shown in Fig.6 of Ref.7. These characteristics suggest that spectral hole burning, when it appears, mainly occurs in the shorter wavelength region than the lasing mode in the VSIS laser. In addition, when the driving current is increased, gain suppression is weakened for the longer wavelength region just before the mode jump. Actually, the spectral hole burning in the spectra of nonlasing mode is rarely observed in VSIS lasers. In Fig.4, Δ represents the position of the spectral hole burning where the nearest neighboring modes (±1) are not strongest, and at almost all currents, the nearest long wavelength neighboring mode is strongest, as shown in Fig.5. This means that the spectral hole burning does not exist or the width of the hole is narrower than the longitudinal mode spacing, which is also different from the CSP laser.[7]

In the upper portion of Fig.4, the intrinsic spectral noise intensity measured at 1.5 MHz is also shown. The excess noise does not appear even at the mode jump due to the hysteresis characteristic mentioned above, in contrast to the lasers without the hysteresis characteristic.[22] It should be noted that the excess noise around the threshold consists of two peaks, whereas both gain-guided[20,21] and index-guided[23] lasers already reported showed a single noise peak. The second noise peak is stronger than the first one in some devices, as demonstrated in Fig.6. In the case of gain-guided lasers, the noise peak at the threshold is principally attributed to the quantum shot noise.[21,24] In the case of index-guided lasers, the noise peak at the threshold is due to the mode-competition noise as well as the quantum shot noise.[23,24] In the VSIS laser, the quantum shot noise and the mode-competition noise take their maxima at two different currents; the first peak at the threshold is due to the quantum shot noise

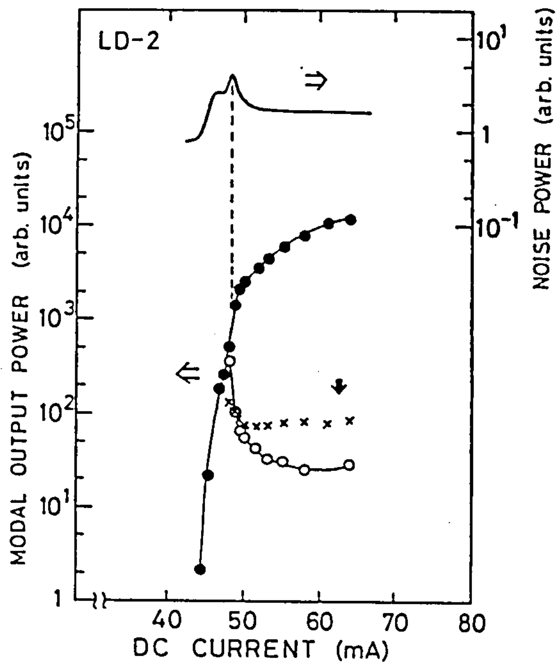

Fig. 6 Another example of intensities of lasing and non-lasing modes and of intrinsic spectral noise as a function of dc current for a type I device.

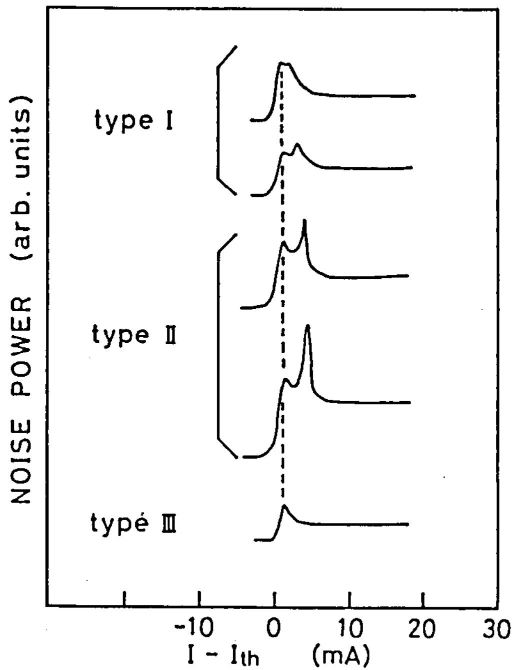

Fig. 7 Typical examples of noise-power-versus-current characteristics of different types of devices.

and the second peak is due to the mode-competition noise.

LD-1 shown in Fig.4 operates on two longitudinal modes and LD-2 shown in Fig.6 operates on three longitudinal modes when the second noise peak appears; then modes except the main lasing mode are suppressed with increasing current. The intensity of the second noise peak due to the mode competition depends on the number of longitudinal modes lasing at the second noise peak. Multimode oscillation slightly above the threshold causes the apparent strong gain suppression in nonlasing modes shown in Figs.4 and 6.

The author examined noise-power-versus-current characteristics on 112 regular devices from 6 lots, and 101 devices showed the above mentioned two noise peaks. Thus, the multimode oscillation slightly above the threshold is inherent in the structure of the VSIS laser. To clarify the effect of built-in refractive-index difference on the longitudinal-mode behavior, two different types of devices were fabricated. In one device denoted as type II, the AlAs mole fraction of the p-type cladding layer is 0.5 and that of the n-type cladding layer is 0.45. Other parameters are the same as those in regular devices (type I). In another device denoted as type III, the thickness of the p-type cladding layer is less than 0.1 μm and other parameters are the same as those in type I. The refractive-index difference parallel to the junction plane is smaller in type II and larger in type III than in type I.

Typical noise-power-versus-current characteristics of each type of devices are compared in Fig.7. It is clear that the multimode oscillation slightly above the threshold is more noticeable in devices with smaller built-in refractive-index difference. The second noise peak appears at outputs of 0.5-1 mW in type I and at outputs of 1-1.3 mW in type II. By contrast, the second noise peak does not appear in type III as in usual index-guided devices, such as the CSP laser.[22] These experimental results qualitatively agree with the thoretical results by Seki et al.[6] In theirs,

many modes easily oscillate at the same time in weakely index-guided lasers, especially silghtly above the threshold in the devices with a narrow current channel. The refractive-index in the VSIS laser is not as large as that in lasers with a buried active layer[10,25] or with the thickness variation of active or waveguide layers parallel to the junction plane.[11,26] The width of current confining channel (∿2 μm) is narrower than that of built-in optical waveguide (∿4 μm). These structural features are considered to lead to the various types of longitudinal-mode behavior demonstrated above.

It is considered that the inhomogeneities in both spatial and spectral regions are necessary to completely explain experimentally obtained differences in longitudinal-mode characteristics in devices with different structure and doping in the active layer.[3,7,8,10] Further experimental and theoretical investigations will be needed to thoroughly clarify the above mentioned behaviors in index-guided lasers.

3-4. Reliability

3-4-1. Degradation in conventional DH lasers due to the Te-doped n-(GaAl)As cladding layer

For (GaAl)As visible lasers, Te is used as the dopant for the n-type cladding layer in order to obtain high carrier concentrations.[1,2,27,28] The author found that in oxide-defined stripe-geometry lasers emitting at 770 nm described in Chap.I, in which Si and Ge were used as dopants in the cladding layer, the near-field half-width at the facet increased and the "kink" in the light output-current curve moved to lower output levels with operating time even under the moderate operating condition of 3 mW/facet at 25°C. These instabilities presumably result from the

inhomogeneous change in the resistivity of the cladding layer, which causes a change in the gain distribution in the lateral direction. However, when Te, Zn, or Mg were used as dopants in the cladding layers, no change in time was observed for the near-field pattern and the light output-current curve. The symmetric gain profile in the lateral direction resulting from the uniform and low resistive cladding layers are essential factors for the stable fundamental-mode operation in index-guided lasers as well as gain-guided lasers.

Tellurium in the cladding layer was, however, found to lower the reliability of conventional oxide-stripe lasers grown on n-GaAs substrates. EBIC images of the oxide-stripe lasers in Fig.8 demonstrate that the Te-induced terracing of the n-type cladding layer enlarges as the Te concentration is increased. The contrast of the EBIC image represents the surface morphology of the n-type cladding layer. The nonplanarity of the heterostructure interface causes the increase in the threshold current due to the scattering loss at the interface. Furthermore, when the Te concentration is increased to 10^{18} cm^{-3}, the lifetime of a conventional oxide-stripe laser decreased to less than 10^{3} h under 3 mW/facet operation at 50^{0}C, as shown in Fig.9. The same figure also illustrates that the yield of long-lived devices is very low even when the Te concentration is as low as 5×10^{17} cm^{-3}, although Te-induced terracing is not observed in this case. This suggests that Te has another influence more than just making terraces.

In contrast to conventional lasers, the Te-doped n-type cladding layer is grown "on" the active layer in the VSIS laser by using the p-type substrate. As a result of this reverse growth sequence of the active and Te-doped cladding layers, the degradation arising from the rather poor quality of the Te-doped "first grown" cladding layer is suppressed, as demonstrated in §3-4-2. Although the Te concentration in the n-type cladding layer is as high as 1×10^{18} cm^{-3} in the VSIS laser, long-lived devices are reproducibly obtained with considerably high yields. The photolumi-

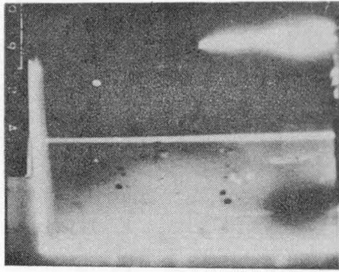

Te ~ 3×10^{17} cm^{-3}

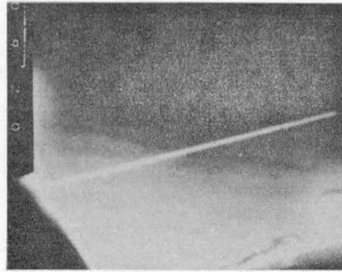

Te ~ 8×10^{17} cm^{-3}

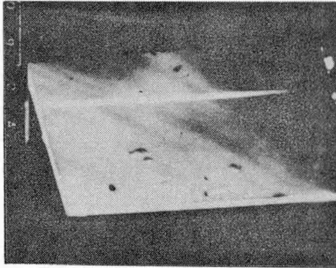

Te ~ 1×10^{18} cm^{-3}

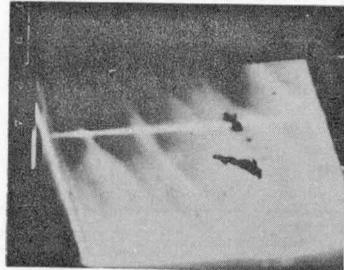

Te ~ 1.5×10^{18} cm^{-3}

Fig. 8 EBIC images of the conventional oxide-stripe lasers grown on the n-GaAs substrate with various Te concentrations in the n-type cladding layer.

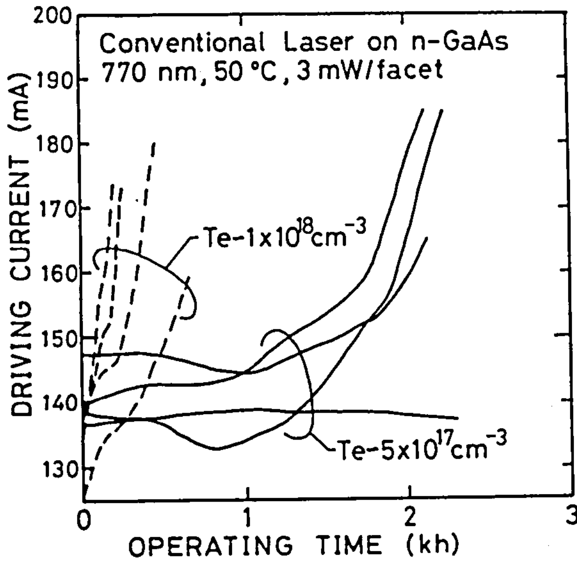

Fig.9 Aging results of the conventional oxide-stripe lasers grown on the n-GaAs substrate with Te concentrations in the n-type cladding layer of 5×10^{17} and 1×10^{18} cm^{-3}.

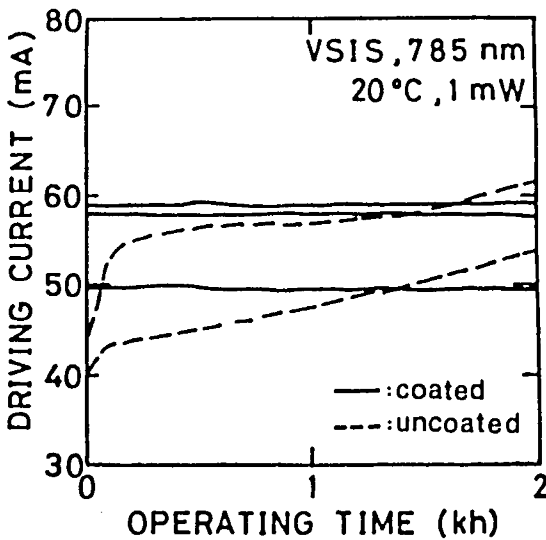

Fig.10 Comparison of aging results of VSIS lasers emitting at 785 nm with and without Al_2O_3 facet coating under 1 mW/facet operation at 20°C.

nescence study presented in §3-4-4 confirms the improved quality of the active layer due to reverse growth sequence.

The present results on laser lifetimes suggest that Te-induced defects or nucleating agents, such as Al_2Te_3, are formed in the vicinity of the surface of the n-type cladding layer during the growth.[12,13] These defects or nucleating agents themselves must lower the reliability of devices or affect the defect formation in the succeeding active layer growth.

3-4-2. Accelerated reliability test

Several reports are published concerning the reliability of (GaAl)As visible lasers, and reliable lasers have been reported at wavelengths of about 780 nm.[2,29,30] However, the lifetimes of conventional visible lasers emitting at about 780 nm are much shorter than infrared lasers emitting above 810 nm, which are widely used in fiber-optic communications. A few tens of nanometer decrease in the emission wavelength considerably decreases the lifetime of (GaAl)As visible lasers even for devices emitting at about 780 nm.

The devices both with and without Al_2O_3 facet coatings were aged under the very moderate operating condition of 1 mW/facet at 25°C. It is confirmed from aging results shown in Fig.10 that the facet coating is an essential factor for the stable operation of visible lasers

The author conducted accelerated reliability tests on regular VSIS lasers lasing at 780 nm and evaluated the reliability statistically. Aging tests were performed at 5, 10, and 15 mW/facet at 50°C, and at 5 mW/facet at 70°C. Typical aging results are shown in Fig.11. In the case of 5 mW/facet operation at 70°C, degradation was not observed in any of tested devices, and the driving current slowly decreases with operating time (Fig.11(d)). Therefore, it is impossible to estimate the activation energy at pres-

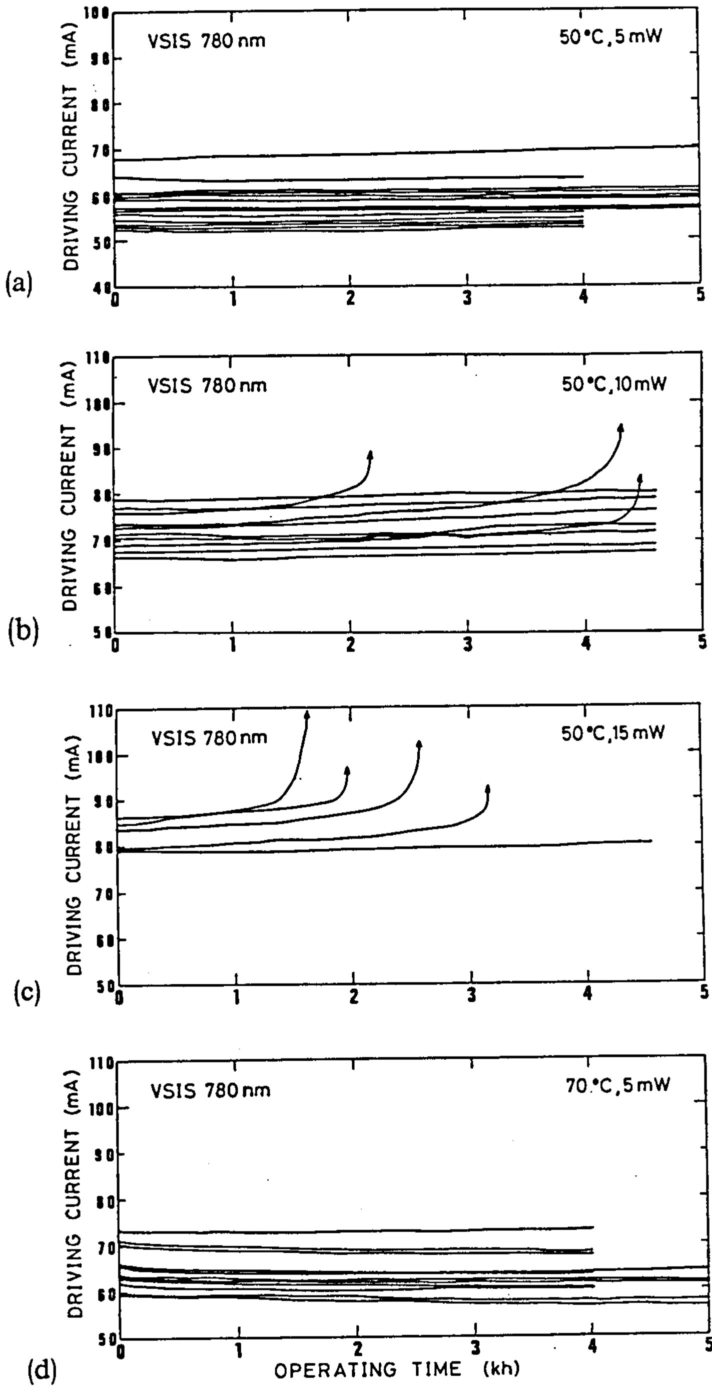

Fig. 11 Aging results of the VSIS lasers emitting at 780 nm under various operating conditions of (a) 5 mW/facet, (b) 10 mW/facet, (c) 15 mW/facet at 50°C, and (d) 5 mW/facet at 70 °C.

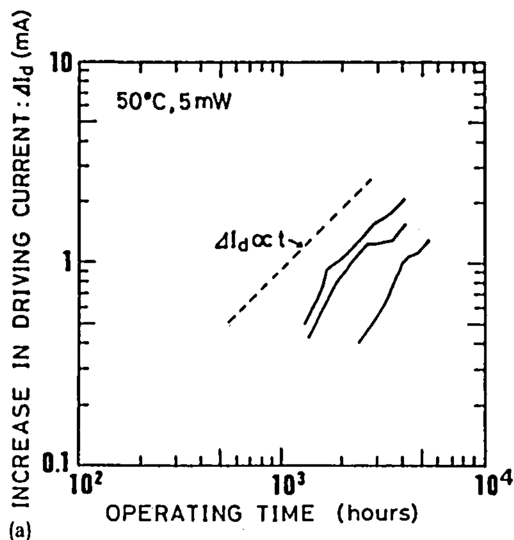

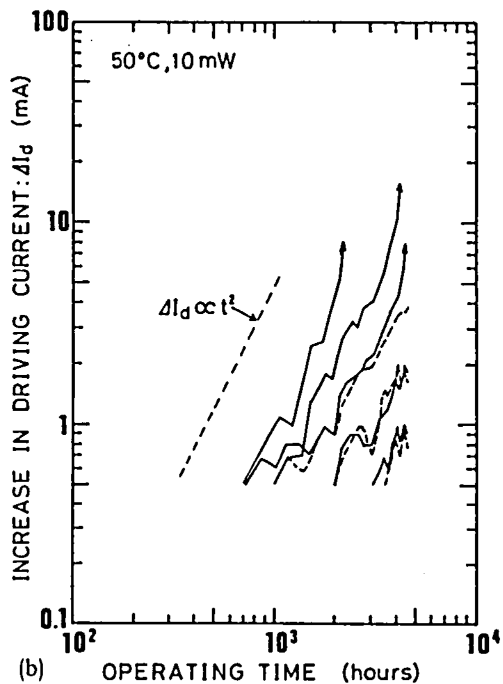

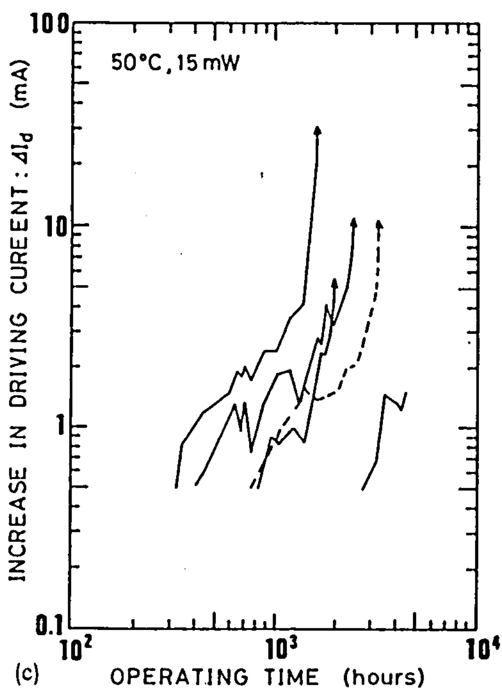

Fig.12 Log-log plot of increase in driving current of the VSIS lasers emitting at 780 nm under various operating conditions of (a) 5 mW/facet, (b) 10 mW/facet, and (c) 15 mW/facet at 50°C. Data are plotted for the devices with relatively high degradation rate in (a) and (b).

ent. This decreasing rate of driving current decreases with operating time. A large decrease in driving current more than 20 mA was observed for lasers emitting at 725 nm even at room temperature operation. The decrease in driving current stopped after 1 h in that case. The amount of decrease in driving current is larger in those 780-nm lasers with higher Te concentration in the n-type cladding layer. Thus, it is likely that some kind of complex defect relating to Te and Al is annealed in the aging. Figures 11(a)-11(c) demonstrate that as the light output is increased, the rate increase of driving current increases. The degradation rate is, however, relatively low even in 10 and 15 mW/facet operations.

Increases in driving current of the lasers whose degradation rates are relatively high are log-log plotted in Fig.12. The driving current increases almost linearly with operating time in the lasers operated at 5 mW/facet (Fig.12(a)). This linear degradation mode was also observed in the oxide-stripe infrared lasers operated 5 mW/facet at 70°C, as shown in Fig.13.[14] By contrast, the driving current increases approximately as the square of operating time in the lasers operated at 10 and 15 mW/facet (Figs.12(b) and 12(c)). This difference suggests that the degradation mechnism is different between the high power-density operation and the low power-density operation.

A noticeable feature is that in the high power-density operation, the limit of the increase in driving current at which the driving current starts runaway, is lower than that in the low power-density operation. In 10 and 15 mW/facet operations, as indicated in Figs.12(b) and 12(c), only about a 5 mA increase in driving current causes driving current runaway, and the lasing terminates soon after. In the case of the low power-density operation (5 mW/facet), it is difficult to estimate the end of the linear degradation with time from the aging data of 780-nm lasers as shown in Figs.11(a) and 12(a), because the degradation rate is very low and the operating time is not long enough at present. The degradation rate is higher in the lasers emitting at shorter

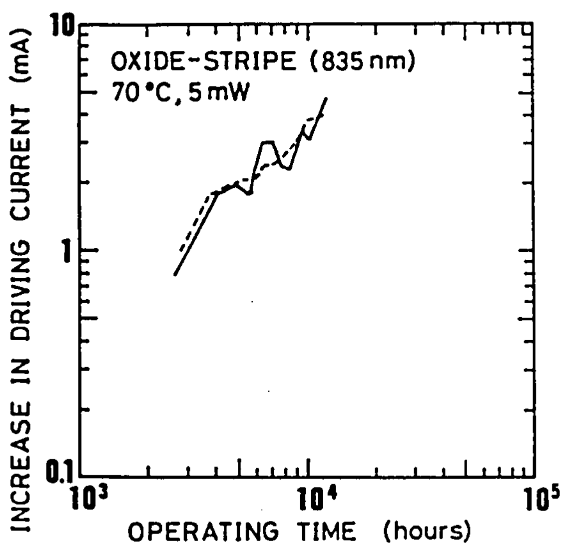

Fig.13 Increase in driving currents of the oxide stripe lasers emitting at 835 nm under 5 mW/facet operation at 70 °C. Data are presented for the devices with relatively high degradation rate.

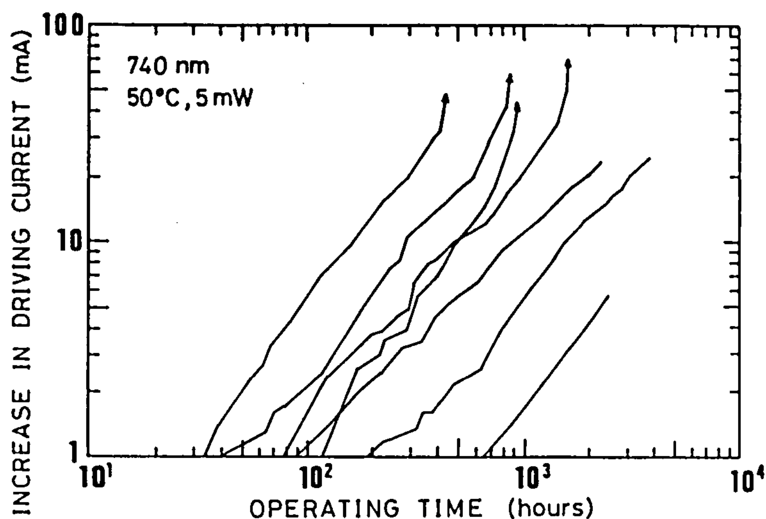

Fig.14 Increase in driving currents of VSIS lasers emitting at 740 nm under 5 mW/facet operation at 50 °C. Data are presented for the devices with relatively high degradation rate.

wavelengths.[29] Therefore, in order to estimate the time of termination, devices emitting at 740 nm were fabricated and were operated at 5 mW/facet at 50°C. Aging results of the devices whose degradation rates are comparatively high, shown in Fig.14, indicate that the limit of the linear increase in driving current before runaway is more than 20 mA for the low power-density operation.

Figure 15 compares the log-normal plots of estimated lifetimes for different output power operating conditions at 50°C. Here, lifetime is defined as the time when the increase in driving current reaches 20 mA in the case of 5 mW/facet operation and 5 mA in the case of 10 and 15 mW/facet operations. Due to the limit of accuracy of the aging system, it is impossible to estimate lifetimes longer than 2×10^5 h in the case of linear degradation mode and 1×10^4 h in the case of square degradation mode.

The relation between the estimated median lifetime and the light output power is shown in Fig.16. Lifetime of the VSIS laser strongly depends on the output power, approximately in proportion to the inverse fourth power of the output power. This result is different from the inverse square dependence of lifetime on the output power, previously reported for the infrared planar-stripe lasers with relatively wide stripe width (15 μm).[31] This difference would arise from the following two factors. The first is the difference in the emission wavelength: 780 and 830 nm. The second is the difference in the density of output power, and this is probably the principal factor. In the VSIS laser, the near-field half-width in the parallel direction is about 2 μm, and, therefore, the power density at the facet is as high as 5 mW/μm in the parallel direction for 10 mW/facet operation. The thickness of the active layer is about 0.08 μm and the full-width at half-power (FWHP) of the far-field pattern in the perpendicular direction is typically 35°. In this case, the near-field half-width in the perpendicular direction is calculated to be about 0.25 μm. Thus, the power density in the perpendicular direction is higher than

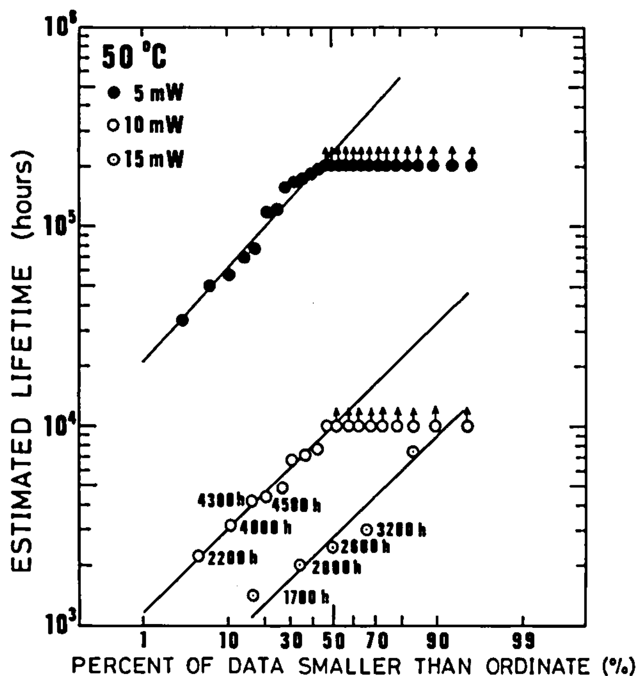

Fig.15 Distribution of estimated lifetime of the VSIS lasers operated under the conditions of various light output powers at 50°C. Data with arrows mean that estimated lifetimes are longer than indicated values. For the devices which stopped lasing, actual time of failure is also indicated.

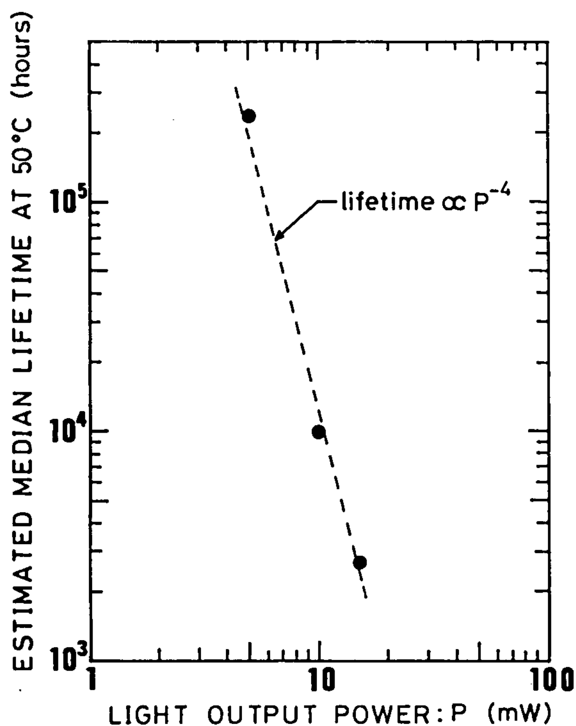

Fig.16 Estimated median lifetime at 50°C vs light output power.

lasers with the large-optical-cavity (LOC).[10,32,33] The power density at the facet is calculated to be as high as 2×10^6 W/cm^2 for 10 mW/facet operation. Here, it should be noted that in spite of the operation at extremely high power density near the catastrophic optical damage (COD) level,[34] lifetime is fairly long in the 10 mW/facet operation. This could result from the improvement of the active layer itself by growing it on a p-type cladding layer.

By use of the previously obtained activation energy of 0.52 eV,[14,35] the median lifetimes at 25°C are estimated to be 1.1×10^6 h for 5 mW/facet, 4.8×10^4 h for 10 mW/facet, and 1.3×10^4 h for 15 mW/facet operations. Lifetimes of visible VSIS lasers for 5 mW/facet operation are as long as or longer than those of conventional infrared lasers emitting above 810 nm.[36,37]

3-4-3. Modal stability with aging

From a viewpoint of practical applications, the stability of modal characteristics is very important. The author measured (1) the far-field pattern, (2) dc signal to rf noise (S/N) ratio of emitted light, and (3) polarization ratio of emitted light, on VSIS lasers emitting at 780 nm. Measurements were carried out at an output power of 5 mW/facet at room temperature before and after 5 mW/facet operation at 50°C. In the measurement of S/N ratio, the noise power was measured at 1.5 MHz with a bandwidth of 10 kHz. Polarization ratio was measured using the Glan-Thompson prism as an analyzer. Measurements were performed on 19 samples.

The far-field pattern in the lateral direction did not change after 4000 h as demonstrated in Fig.17(a). Relative change of FWHP from values at 0 h, as shown in Fig.17(b), are almost within the limit of measuring accuracy (±1°). Thus, the transverse mode is highly stable in VSIS lasers, as compared to gain-guided lasers.[38]

The S/N ratio and the polarization ratio of emitted light are

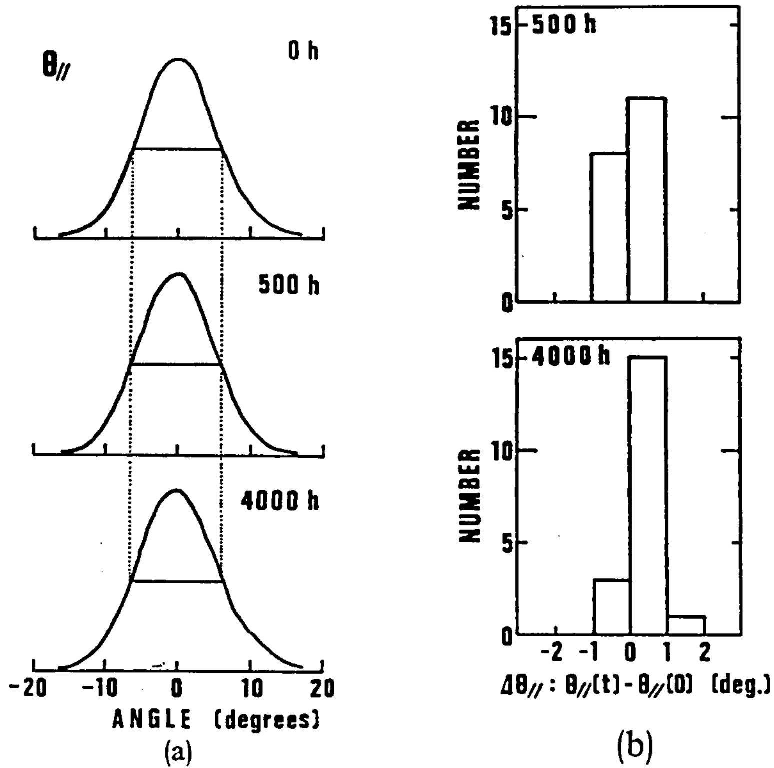

Fig.17 (a) A typical example of lateral far-field patterns measured before (0 h) and after the agings of 500 and 4000 h under 5 mW/facet at 50°C.
(b) Relative change of full-width at half-power (FWHP) of far-field pattern from 0 h after aging.

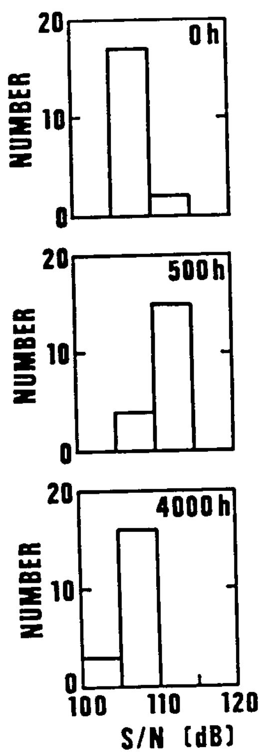

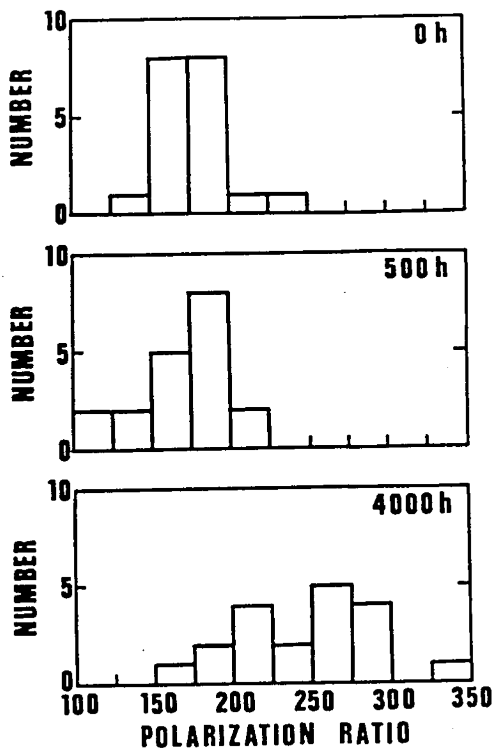

(a) (b)

Fig.18 Distributions of (a) S/N ratio and (b) polarization ratio of emitted light before (0 h) and after 5 mW/facet operation at 50°C. rf noise power was measured at 1.5 MHz with a bandwidth of 10 kHz.

required to be higher than specified values for some information processing applications, such as an optical-disk playback system. Distribution of the S/N ratio and the polarization ratio are shown in Fig.18. Figure 18(a) shows that the S/N ratio slightly increases from 0 to 500 h and moderately decreases from 500 to 4000 h. The polarization ratio slightly decreases from 0 to 500 h and increases from 500 to 4000 h, as shown in Fig.18(b). These small changes in modal characteristics are considered to be acceptable in almost all practical applications.

3-4-4. Photoluminescence study

The photoluminescence was measured to clarify the influences of the Te-doped cladding layer on the active layer and laser properties. Measurements were carried out at 77 K by excitation with 632.8-nm light from a He-Ne laser and with weak uv light from a high pressure mercury lamp. Samples listed in Table I are DH layers grown by LPE. Thickness of the second layer, which simulates the active layer, is thicker than that of the actual active layer of less than 0.1 μm in order to get enough photoluminescence intensity even at low excitation intensities. In particular, when the sample is excited by 632.8-nm light, the substrate is also excited and the short wavelength luminescence component from the substrate hides any luminescence from the second layer at low excitation intensities. Thus, excitation with weak uv light from a high pressure mercury lamp was conducted in order to obtain photoluminescence spectra at low excitation intensities. In this case, a substrate is not excited because uv light is almost completely absorbed in the DH layers. The third layer simulates the cladding layer, through which the light emitted from the second layer penetrates without absorption. The third layer, which is thinner than that of the real cladding layer of 1 μm, also makes it possible to excite the sample by short wavelength light which is partly absorbed by it.

Table I Doping of samples for photoluminescence measurements.

Sample No.	Substrate: GaAs		1st layer: $Ga_{0.4}Al_{0.6}As$		2nd layer: $Ga_{0.85}Al_{0.15}As$	3rd layer: $Ga_{0.4}Al_{0.6}As$	
	Conduction type	Impurity (10^{18} cm^{-3})	Conduction type	Impurity (10^{18} cm^{-3})	Undoped	Conduction type	Impurity (10^{18} cm^{-3})
PL-1	n	Si ∿ 2	n	Te ∿ 0.4	•••••	p	Mg ∿ 1
PL-2	n	Si ∿ 2	n	Te ∿ 2	•••••	p	Mg ∿ 1
PL-3	n	Si ∿ 2	p	Mg ∿ 1	•••••	n	Te ∿ 1
PL-4	p	Zn ∿ 10	p	Mg ∿ 1	•••••	n	Te ∿ 1

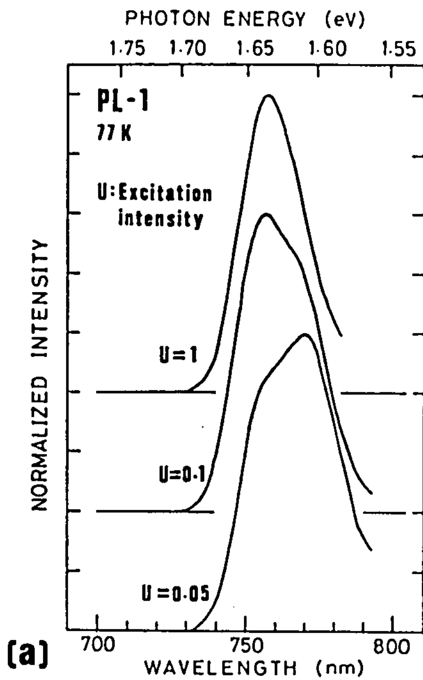

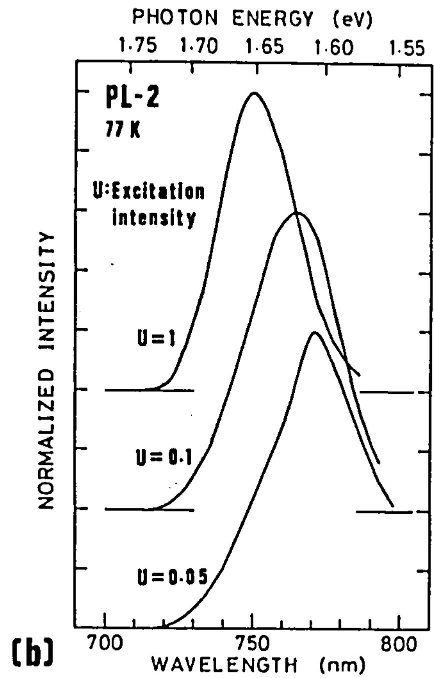

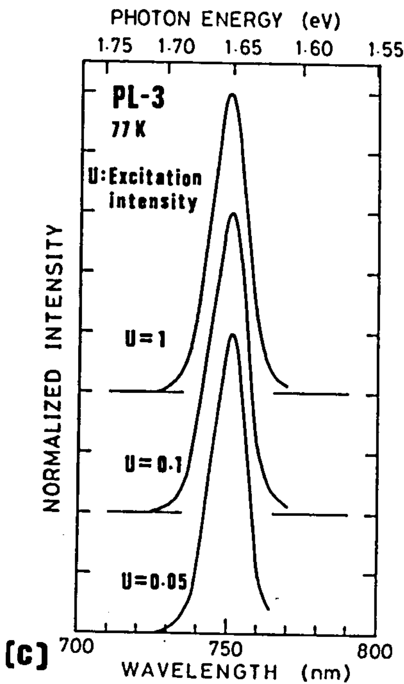

Fig. 19 Variation in photoluminescence spectra with excitation intensity of (a) PL-1, (b) PL-2, and (c) PL-3 at 77 K. Measurements were carried out by excitation with 632.8-nm light from a He-Ne laser.

Photoluminescence spectra of PL-1, -2, and -3 by excitation with a He-Ne laser are shown in Fig.19. With decreasing excitation intensity, a new peak appears in the case of PL-1; the peak shifts to longer wavelengths and changes its shape in the case of PL-2. The photoluminescence spectrum of PL-2 excited by weak uv light, as shown in Fig.20, consists of two peaks. In contrast to these results, the photoluminescence spectra of PL-3, shown in Fig.19(c), and those of PL-4 (not shown) demonstrate that the spectrum does not change with decreasing excitation intensity when the first layer is not doped with Te. These results indicate that a radiative center is formed in the second layer when the second layer is grown on top of the Te-doped first layer.

The peak intensity, half-width, and photon energy of the spectrum of each sample at the highest excitation intensity, U=1, are summarized in Table II. For PL-1 and -2, the peak photon energies at the lowest excitation intensity, U=0.05, are also listed in Table II. Comparison among peak intensities clearly reveals that the luminescence efficiency of the second layer grown on the Te-doped first layer is lower than that of the second layer grown on the Mg-doped first layer approximately by a factor of 5.

The scatter in the peak energies at the highest excitation in Table II arises from the difference in Al contents in growth solutions. In particular, in PL-4, the AlAs mole fraction of the second layer is larger than other samples and is about 0.17. From the spectra in Fig.19, it is deduced that the photoluminescence peaks of PL-1 and -2 at the highest excitation as well as those of PL-3 and -4 are due to band-edge transitions. Peak half-widths of PL-1 and -2 are more than twice as wide as those of PL-3 and -4. This suggests that either the compositional grading of Al severely occurs at the interface between the first and second layers when the first layer is doped with Te, or the disorder or imperfection of the second layer on the Te-doped first layer. With regard to these points Al profiles are examined in §4-2-2.

From above mentioned results, it is clear that the Te-doped

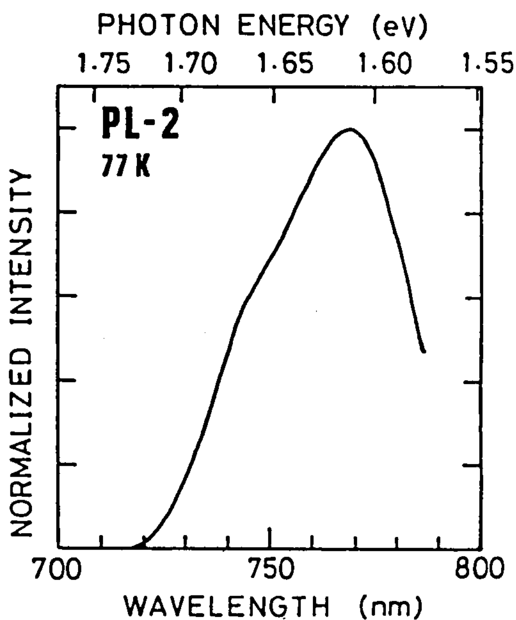

Fig. 20 Photoluminescence spectrum of PL-2 excited by weak uv light from a high pressure mercury lamp at 77 K.

Table II Intensity, half-width, and photon energy of PL peaks for individual samples.

Sample No.	PL peak intensity[a] (arb. units)	Half-width of PL peak[a] (nm)	Peak photon energy[b] (eV)	
PL-1	0.18	26	1.637	1.609
PL-2	0.16	30	1.650	1.607
PL-3	0.98	14	1.652	.....
PL-4	1.0	13	1.697	.....

[a] At the highest excitation intensity (U=1).
[b] For PL-1 and -2, values at the highest (U=1) and lowest (U=0.05) excitation are listed.

cladding layer reduces the quality of the active layer and/or that of interface between the active and cladding layers when the active layer is grown on the Te-doped cladding layer. These faults are eliminated by reverse growth sequence of the active and Te-doped cladding layers. It should be noted that the effect of the subtrate difference is negligible since the results of PL-3 grown on n-GaAs and PL-4 grown on p-GaAs are almost the same.

3-5. Summary

Highly mode-stabilized and reliable operation is realized in newly developed VSIS lasers emitting in the visible wavelength region. Modal characteristics are investigated in detail and longitudinal-mode behaviors depending on the structural factor are demonstrated. The degradation which arises from the rather poor quality of the Te-doped cladding layer is suppressed in the VSIS laser by the reverse growth sequence of the active and Te-doped cladding layers using p-type GaAs as a substrate; i.e., the Te-doped cladding layer is grown on the active layer, rather than under the active layer in conventional lasers fabricated on n-GaAs. Photoluminescence study on DH layers revealed that the Te-doped cladding layer "under" the active layer impairs the quality of the active layer and the quality of the active layer is improved when it is grown upon a p-cladding layer followed by the growth of the Te-doped cladding layer "on" the active layer. Accelerated life tests and the statistical characterization of reliability were performed on VSIS lasers emitting at 780 nm. The median lifetime is estimated to be 1.1×10^{6} h for 5 mW/facet operation at 25°C, which is comparable or superior to reported lifetimes for infrared lasers. In addition, almost no degradation in modal characteristics has been observed in the devices operated at 5 mW/facet at 50°C for 4000 h.

References

1) H.Kumabe, H.Namizaki, and W.Susaki, IECE Japan Tech. Group Electron. Dev., Rep. ED79-79, 61 (1979) (in Japanese).

2) M.Wada, K.Itoh, H.Shimizu, and I.Teramoto, IEEE J. Quantum Electron. QE-17, 776 (1981).

3) M.Yamada and Y.Suematsu, Jpn. J. Appl. Phys. Suppl.18-1, 347 (1979).

4) M.Yamada and Y.Suematsu, IEEE J. Quantum Electron. QE-15, 743 (1979).

5) M.Yamada and H.Nagato, Trans. Inst. Electron. & Commun. Eng. Jpn. E64, 770 (1981).

6) K.Seki, T.Kamiya, and H.Yanai, IEEE J. Quantum Electron. QE-17, 706 (1981).

7) M.Nakamura, K.Aiki, N.Chinone, R.Ito, and J.Umeda, J. Appl. Phys. 49, 4644 (1978).

8) H.Kawanishi and P.E.Petersen, IEEE J. Quantum Electron. QE-17, 823 (1981).

9) Y.Itaya, T.Tanbun-Ek, K.Kishino, S.Arai, and Y.Suematsu, Jpn. J. Appl. Phys. 19, L141 (1980).

10) K.Saito and R.Ito, IEEE J. Quantum Electron. QE-16, 205 (1980).

11) Y.Ide, T.Furuse, I.Sakuma, and K.Nishida, Appl. Phys. Lett. 36, 121 (1980).

12) W.R.Wagner, J. Appl. Phys. 49, 173 (1978).

13) R.A.Logan, N.E.Schumaker, C.H.Henry, and F.R.Merritt, J. Appl. Phys. 50, 5970 (1979).

14) T.Hayakawa, S.Yamamoto, S.Matsui, T.Sakurai, and T.Hijikata, Jpn. J. Appl. Phys. 21, 725 (1982).

15) L.Figueroa and S.Wang, Appl. Phys. Lett. 31, 45 (1977).

16) H.Ishikawa, N.Takagi, O.Ohsaka, K.Hanamitsu, T.Fujiwara, and M.Takusagawa, Appl. Phys. Lett. 36, 520 (1980).

17) K.Aiki, M.Nakamura, T.Kuroda, and J.Umeda, Appl. Phys. Lett. 30, 649 (1977).

18) T.Kuroda, M.Nakamura, K.Aiki, and J.Umeda, Appl. Opt. 17, 3264 (1978).

19) K.Aiki, M.Nakamura, T.Kuroda, J.Umeda, R.Ito, N.Chinone, and M.Maeda, IEEE J. Quantum Electron. QE-14, 89 (1978).

20) T.L.Paoli, IEEE J. Quantum Electron. QE-11, 276 (1975).

21) Y.Takanashi, S.Takahashi, T.Kobayashi, and Y.Furukawa, Jpn. J. Appl. Phys. 16, 2217 (1977).

22) S. Horiuchi, K.Ohtaki, K.Yamanaka, H.Kumabe, S.Takamiya, and K.Shirahata, Pro. 7th European Conf. Optical Communication 10.3-3 (1981).

23) R.O.Miles, A.Dandridge, A.B.Tveten, T.G.Giallorenzi, and H.F. Taylor, Appl. Phys. Lett. 38, 848 (1981).

24) G.H.B.Thompson, Physics of Semiconductor Laser Devices (John Wiley & Sons, Chichester, 1980) p.467.

25) K.Shima, K.Hanamitsu, T.Fujiwara, and M.Takusagawa, Appl. Phys. Lett. 38, 605 (1981).

26) R.D.Burnham and D.R.Scifres, Appl. Phys. Lett. 27, 510 (1975).

27) T.Kajimura, T.Kuroda, S.Yamashita, M.Nakamura, and J.Umeda, Appl. Opt. 18, 1812 (1979).

28) H.Kressel and F.Z.Hawrylo, appl. Phys. Lett. 28, 598 (1976).

29) T.Kajimura, J. Appl. Phys. 51, 908 (1980).

30) T.Hayakawa, S.Yamamoto, T.Sakurai, and T.Hijikata, J. Appl. Phys. 52, 6068 (1981).

31) H.Imai, M.Morimoto, K.Hori, M.Takusagawa, and H.Saito, IEEE J. Quantum Electron. QE-16, 248 (1980).

32) W.T.Tsang and R.A.Logan, IEEE J. Quantum Electron. QE-15, 451 (1979).

33) D.Botez, Appl. Phys. Lett. 36, 190 (1980).

34) H.Kressel and J.K.Butler, Semiconductor Lasers and Hetero-junction LED's (Academic, New York, 1977) Chp.16.

35) T.Hayakawa, S.Yamamoto, H.Hayashi, N.Ohtsuka, K.Murata, J. Takagi, T.Sakurai, and T.Hijikata, IEDM Tech. Digest, 443 (1981).

36) R.L.Hartman, N.E.Schumaker, and R.W.Dixon, Appl. Phys. Lett. 31, 756 (1977).

37) M.Ettenberg, J. Appl. Phys. 50, 1195 (1979).

38) M.Ettenberg, J. Appl. Phys. 52, 3845 (1981).

IV. PROPERTIES OF VISIBLE LASERS EMITTING BELOW 750 nm

4-1. Introduction

A lot of efforts have been made in the research and development of semiconductor lasers emitting in the visible wavelength region.[1-10] Among several wide-band-gap mixed crystals, such as (GaAl)As,[1-6] (InGa)(AsP),[7-9] and Ga(AsP),[10] (GaAl)As is the most promising material for visible semiconductor lasers at present, since $Ga_{1-x}Al_xAs$ closely lattice matches to GaAs for the whole composition range x and does not have the miscibility gap, which has been reported in the (InGa)(AsP) system.[11] However, previously reported (GaAl)As visible lasers emitting below 750 nm suffer from the significant increase in the threshold current.[3-6] This fault results partly from the insufficient quality of the heterostructure interface[12,13] and the bulk (GaAl)As[14] especially when Al-rich (GaAl)As is used. Also for Al-rich (GaAl)As with the indirect band structure, it is difficult to obtain a highly conductive n-(GaAl)As layer using group IV dopants Si and Sn. Thus Te is usually used as the dopant for the n-type cladding layer of (GaAl)As visible lasers in order to obtain high carrier concentration.[3-5] The symmetric gain profile in the lateral direction resulting from the uniform and low resistive cladding layers is an important factor for the stable fundamental-mode operation in stripe-geometry lasers.[14,15] However, Te tends to form complex defects and to create terracing at the surface of the epitaxial layers in (GaAl)As,[16-18] which impairs the properties of (GaAl)As visible lasers as described in §3-4-1.

Another problem in (GaAl)As visible lasers emitting below 750 nm is the high threshold-temperature sensitivity.[19] The temperature dependence of the threshold current of DH lasers, especially at and above room temperature, is one of the most important characteristics and is desired to be as weak as possible for the stable operation in practical systems. (GaAl)As visible lasers

emitting below 750 nm also suffer from short lifetimes.[5,20,21] In general, the lifetime of (GaAl)As visible lasers decreases exponentially with decreasing emission wavelength.[20] It has been reported that one of the causes of the decrease in lifetime with decreasing emission wavelength is the increase in the active layer stress caused by the lattice mismatch between the (GaAl)As DH layers and the GaAs substrate.[21,22]

In this chapter, the author demonstrates the excellent performances of VSIS lasers emitting below 750 nm, where there have been a lot of problems to be solved as mentioned above. The basic structure and the fabrication process of the VSIS laser employed in this chapter are described in §3-2. First, low-current-threshold behavior in VSIS lasers emitting below 750 nm is presented. Threshold current variation of VSIS lasers with the lasing wavelength is compared with the calculated variation of the inverse of internal quantum efficiency η_i and previously reported experimental results. The causes of the increase in the threshold current of lasers emitting below 750 nm is discussed in connection with the influence of the Te-doped cladding layer upon laser properties. Secondly, the temperature dependence of the threshold current of VSIS lasers with emission wavelengths of 697-781 nm is measured and compared with the calculated results by a model of carrier leakage due to unconfined carriers in the active layer. The factors which determine the threshold-temperature sensitivity is examined on the basis of the calculated results. Finally, it is demonstrated that the lifetime of visible lasers emitting at 740 nm can be improved by setting the thickness of the cap layer and the substrate at the appropriate values to reduce the active layer stress caused by the bonding process.

4-2. Threshold Current

It is described in Chap.III that high reliability, comparable to that of infrared lasers, is realized in VSIS lasers emitting at 780 nm by growing the Te-doped cladding layer on top of the active layer using p-type GaAs as a substrate; whereas in conventional lasers fabricated on n-type substrates, the active layer is grown on top of the Te-doped cladding layer. Here, low threshold current of VSIS lasers emitting below 750 nm and cw operation below 700 nm ($\geqq$688 nm at the present time) are presented. These performances result from the reduced current spreading in the VSIS structure and the improved quality of the active layer by the above-mentioned reverse growth sequence of the active and Te-doped cladding layers.

4-2-1. Experimental results

VSIS lasers with emission wavelengths in the range of 790-688 nm were fabricated. The $Ga_{1-x}Al_xAs$ ($0.13 \leqq x \leqq 0.32$) active layer thickness was 0.06-0.1 μm. The difference in AlAs mole fraction between the active layer and the cladding layer was in the range of 0.31-0.41. The cavity length was 250 μm.

The threshold currents of VSIS lasers are plotted in Fig.1 as a function of the lasing wavelength measured at 5 mW/facet. Shown in Fig.1 are also the threshold currents for terraced substrate (TS) lasers[5] and the threshold current densities for channeled substrate planar (CSP) lasers[4] and the calculated variation of $1/\eta_i$, which will be described in §4-2-3. The threshold current of VSIS lasers is almost constant in the wavelength range of 790-720 nm and rapidly increases below 720 nm. The dependence of the threshold current on the lasing wavelength is slightly stronger for the TS laser and the CSP laser than for the VSIS laser. The other data of threshold previously reported for (GaAl)As DH lasers

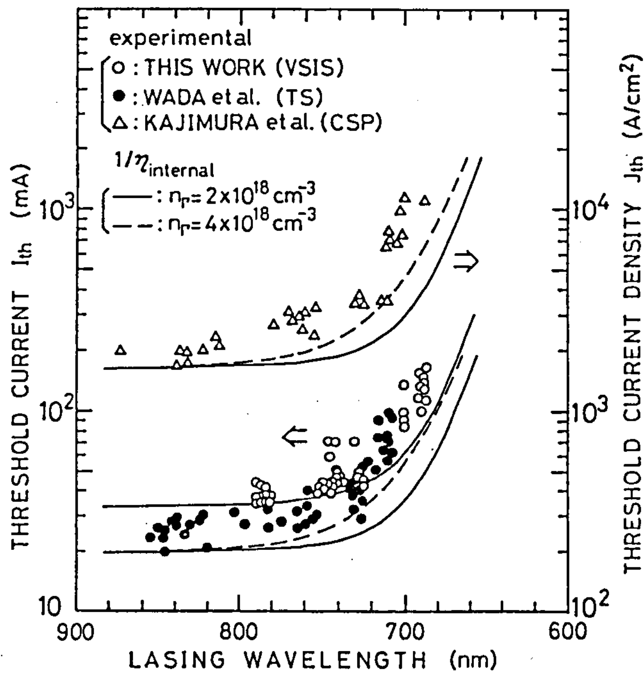

Fig. 1 The variation of room-temperature threshold current or current density with the lasing wavelength of the mode-stabilized (GaAl)As DH lasers. The solid and dashed lines are the inverse of the internal quantum efficiency calculated in §4-2-3.

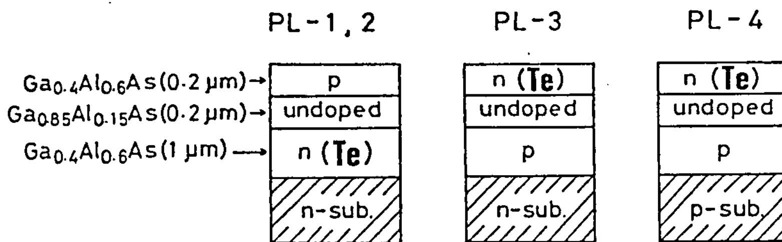

Fig. 2 Schematic representation of the samples used for Al-profile measurements.

grown by LPE[3,23] and molecular-beam epitaxy[6] are still more strongly dependent on the lasing wavelength below 750 nm than those shown in Fig.1. In addition, the VSIS lasers showed cw operation in the whole wavelength range (790-688 nm).

4-2-2. Influence of the Te-doped cladding layer

The author investigates the influence of the Te-doped cladding layer on the quality of the active layer and laser properties in §3-4-4. These results are summarized as follows. When the active layer is grown on top of the Te-doped cladding layer ($n>5\times10^{17}$ cm^{-3}), it is found that: (1) some kind of radiative recombination centers are formed in the active layer; (2) the band-edge luminescence spectrum is more than twice broader; (3) peak intensity of the band-edge luminescence spectrum is ∿5 times weaker than the samples in which the active layer is grown on top of the Mg-doped cladding layer, followed by the growth of the Te-doped cladding layer on the active layer. Moreover, (1) was not found when the active layer was grown on top of the Mg-doped cladding layer. (1) and (2) cause the broadening of the gain spectrum, and together with (3), result in the reduction of the gain peak and thus the increase in the threshold current.

In order to check for nonuniformity in the active layer on top of the Te-doped cladding layer, Al distribution in the active layer was measured. In this experiment, the identical samples which are used for photoluminescence study in §3-4-4 are used after a ∿0.57° angle lap (100 times magnification in thickness). Schematic structures of the samples denoted as PL-1, -2, -3, and -4, are shown in Fig.2. All samples are DH layers grown by LPE. In every sample, the p-$Ga_{0.4}Al_{0.6}As$ cladding layer was doped with Mg ($p\sim1\times10^{18}$ cm^{-3}), and the n-$Ga_{0.4}Al_{0.6}As$ cladding layer was doped with Te ($n\sim4\times10^{17}$ cm^{-3} in PL-1, $n\sim2\times10^{18}$ cm^{-3} in PL-2, and $n\sim1\times10^{18}$ cm^{-3} in PL-3 and -4). The growth sequence of the active and Te-doped cladding layers is reversed in PL-1, -2, and in PL-3, -4.

The Al profile was measured with a scanning Auger electron microscope by measuring the Ga LMM transition (1070 eV).

Growth terraces of the Te-doped cladding layer make the shape of the active layer irregular when the active layer is grown on top of the Te-doped cladding layer, as shown in Fig.3. The height of the growth terrace increases with the Te concentration and is more than 1500 Å in PL-2. These growth terraces obviously increase the threshold due to the scattering loss. The Al profiles for the sections indicated in Fig.3 are shown in Fig.4. It is clear that the compositional grading most severely occurs at the dip of the growth terrace (Fig.4, section 1). Angle laps were not taken normal to the growth terraces, so that the direction of measured sections does not accurately agree with the growth direction. For this reason, it was impossible to measure accurate Al profiles for PL-2, in which terracing of the Te-doped cladding layer is so severe that the cross section of the active layer is extremely irregular. Measured Al profiles revealed compositional grading at both sides of the active layer, as shown in Fig.5(a). By contrast, in PL-3 no irregularities were found in the active layer grown on top of the Mg-doped cladding layer, and thus both interfaces of the active layer are fairly abrupt, as shown in Fig.5(b), along the entire length of one wafer; Al profiles similar to PL-3 were obtained for PL-4 (not shown).

In addition to the light scattering by the growth terraces, above-mentioned Al distribution in the active layer grown on top of the Te-doped cladding layer causes the further increase in the scattering loss due to the abrupt change of the refractive index at the dip of the growth terrace. The observed broadening of the band-edge luminescence spectrum at least partly arises from the nonuniform Al distribution.

4-2-3. Theoretical calculation

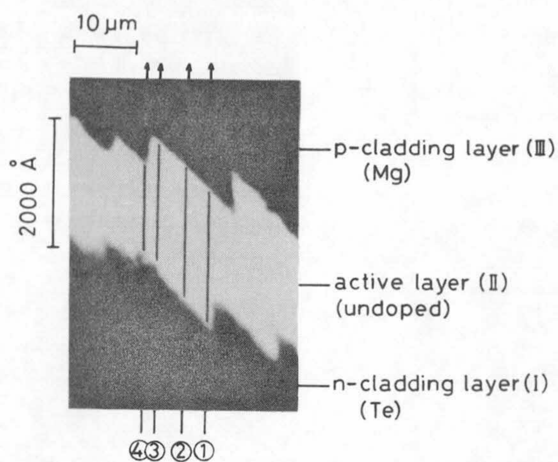

Fig.3 Absorbed electron image of angle-lapped (∿0.57°) cross section of PL-1. Numbered arrows indicate the sections where Al profiles are measured.

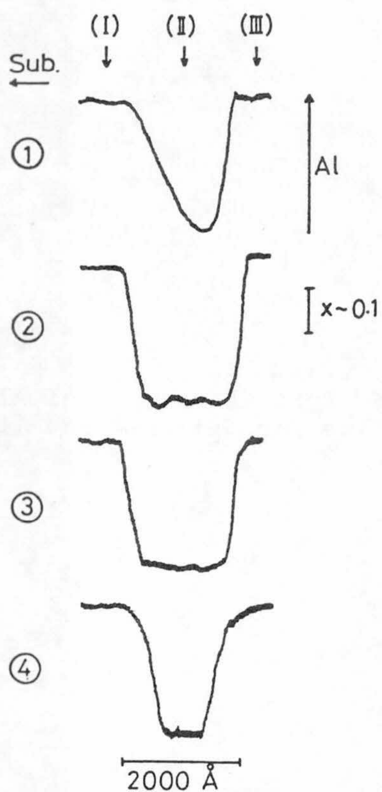

Fig.4 Al profiles for the sections in PL-1 indicated in Fig.3.

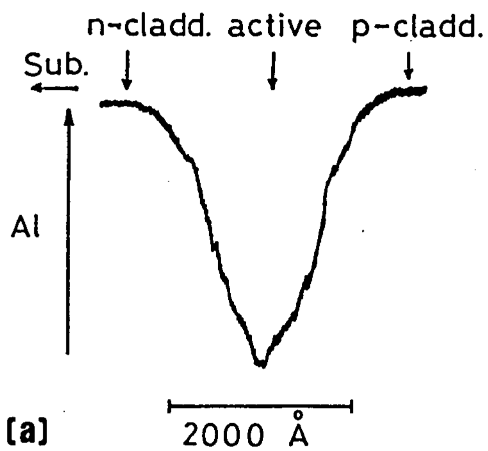

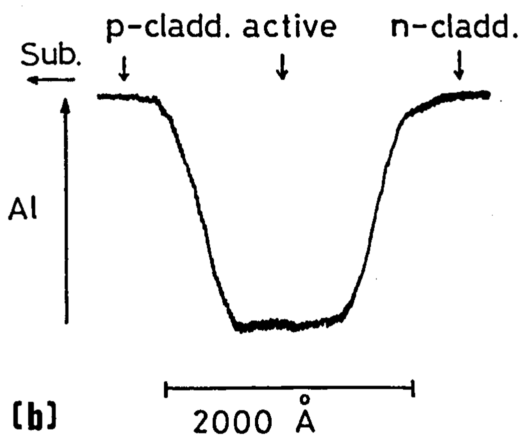

Fig. 5 Typical example of Al profiles for (a) PL-2 and (b) PL-3.

The threshold current is inversely proportional to $1/\eta_i$, which is proportional to the fraction γ of the total electrons in the direct conduction band

$$\gamma = n_\Gamma/(n_\Gamma + n_L + n_X). \tag{1}$$

In this equation, n_i (i=Γ, L, and X) is the electron density for the i conduction band and is written as

$$n_i = \frac{1}{2}\left(\frac{2m_e^i}{\hbar}\right)^{3/2}\int_0^\infty \frac{(E-E_c^i)^{1/2}dE}{1+\exp((E-F_c)/kT)} \tag{2}$$

where m_e^i and E_c^i are the effective density-of-states mass and the conduction-band energy level for the i conduction band (i=Γ, L, and X), respectively, and F_c is the quasi-Fermi level for the conduction band.

The internal quantum efficiency in the short-wavelength region strongly depends on the energy-band parameters used for the calculation. In the previous publications,[4-6,23] the energy-band parameters in Ref.24 where the indirect-direct crossover is assigned at the AlAs mole fraction of 0.37 or values near to these parameters were used to explain the experimentally obtained variation of the threshold current with the emission wavelength. The recent photoluminescence[25,26] and conductivity[27] measurements on (GaAl)As have assigned the indirect-direct crossover at ∿0.45. For the calculation of $1/\eta_i$, the author used the energy-band parameters in Ref.28, where the crossover is assigned at 0.45. Those calculated variation of $1/\eta_i$ with the lasing wavelength for n_Γ= 2×10^{18} cm^{-3} and T=297 K, which were obtained using the parameters in Refs. 24 and 28, are compared in Fig.6.[29] In the calculation, the lasing energy was taken to be the energy gap minus 20 meV, which was estimated from the calculated gain spectrum by Stern.[30] The $1/\eta_i$ also depends on the n_Γ through the change of F_c in Eq.(1), as shown in Fig.7. For a device without any excess losses except the free-carrier absorption and the mirror loss, n_Γ is estimated to be about 2×10^{18} cm^{-3}.[31] When there are excess losses, the in-

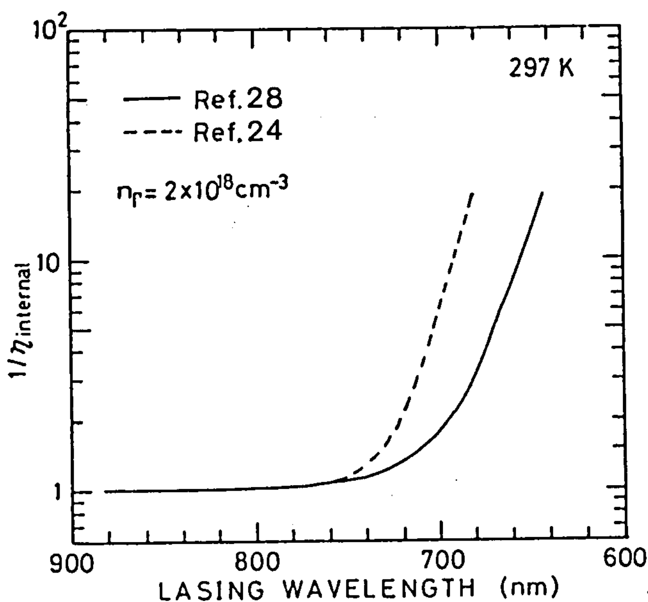

Fig.6 Comparison between the variation of $1/\eta_i$ with the lasing wavelength calculated using the energy-band parameters given in Refs.24 and 28.

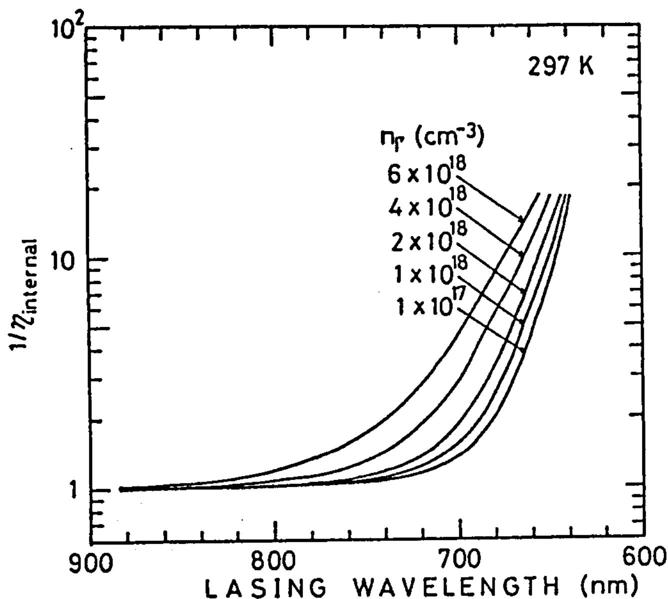

Fig.7 Dependence of $1/\eta_i$ on the electron density n_Γ in direct conduction band. $1/\eta_i$ was calculated using the energy-band parameters given in Ref.24.

crease in n_Γ results in the further increase in the threshold current below 750 nm.

4-2-4. Causes of the increase in threshold

The threshold variation of the VSIS laser with the lasing wavelength almost agrees with the calculated variation of $1/\eta_i$ for the indirect-direct crossover of 0.45 and $n_\Gamma=2\times10^{18}$ cm^{-3}, as shown in Fig.1. The other two lasers shown in the same figure, TS and CSP lasers, exhibit the slightly stronger dependence of the threshold on the lasing wavelength, which rather agrees with the caculated variation of $1/\eta_i$ for $n_\Gamma=4\times10^{18}$ cm^{-3}. Therefore, one possible cause of the increase in the threshold below 750 nm in conventional lasers grown on n-GaAs substrates is the increase in n_Γ, which arises from the excess loss and/or the decrease in the gain peak intensity indicated here: (1) the scattering loss due to the growth terraces and nonuniform Al distribution, and (2) the decrease in the peak intensity of the gain spectrum caused by the broadening and the decreased peak intensity of the band-edge luminescence spectrum. These drawbacks come from the Te-doped cladding layer, and thus can be improved by reducing the Te concentration in the n-cladding layer.

However, in that case, there arises another problem of lateral current spreading due to the high resistivity of the n-cladding layer. Current flows in nonplanar-substrate devices are schematically illustrated in Fig.8. In the devices grown on n-type substrates without lateral current confinement, the current tends to flow to the least resistive paths of the channel shoulder (Fig.8 (a)) or the mesa (Fig.8(b)). These features result from a highly resistive n-(GaAl)As grown over a highly conductive substrate. The laser structure grown over the substrate mesa, like a constricted double-heterojunction (CDH) laser,[32] has the advantage of the less lateral current spreading. On the other hand, the TS and CSP lasers both have similar topographical features like the de-

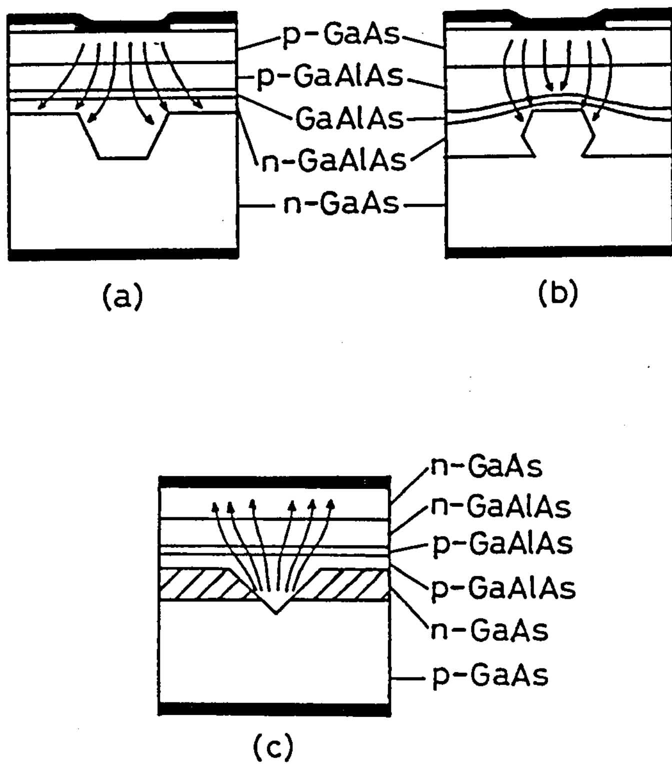

Fig.8 Schematic representation of current flow in (a) (GaAl)As structure grown over a channel of a highly conductive n-GaAs substrate, (b) (GaAl)As structure grown over a mesa of a highly conductive n-GaAs substrate, and (c) (GaAl)As VSIS structure grown over a channeled substrate where a current channel is formed on a p-GaAs substrate.

vice shown in Fig.8(a). Thus, when the Te concentration is decreased, lateral current spreading increases the threshold current in these devices. The decrease in Te concentration increases the lateral current spreading in the conventional stripe-contact devices grown over plain substrates, since the difference in resistivity between n and p cladding layers decreases; in general, $\sigma_n \gg \sigma_p$. The VSIS laser is also grown over a channeled substrate like the CSP laser. However, the great difference between these lasers is that the current stripe is formed in the channel in the VSIS laser and it is formed on the opposite side of the active layer from the channel in the CSP laser. As a result, the lateral current spreading in the VSIS laser is much less than the CSP-type devices on n-GaAs substrates. In addition, the use of the n-cladding layer with relatively high Te concentration ($n=1\times10^{18}$ cm^{-3}) further decreases the lateral current spreading, since it does not impair the laser properties in the VSIS structure.

When the p-GaAs current confining layer is incorporated into the channeled substrate structure shown in Fig.8(a) like the VSIS structure, the p-GaAs layer must be thicker than the electron diffusion length (>1 μm) for completely blocking the current flow outside the channeled region.[33,34] Actually, it is difficult to form the narrow channel (<5 μm) deeper than 1 μm by conventional chemical etching. In the actual device, the thin p-GaAs current confining layer could reduce the current spreading as a resistive layer, but is not enough effective to block the current flow. Thus, the combination of the p-type substrate and the n-type current confining layer in the VSIS structure is the simplest and most effective way to confine the current and reduce the current spreading in the cladding layer.

One of the outstanding feature of the VSIS laser is that cw operation has been realized in the devices emitting at as short as 688 nm, up to the present. This is achieved by improved lifetime[14] of the VSIS laser as well as low threshold current because devices must operate long enough to measure their properties for

cw operation. (GaAl)As visible lasers have shown exponential decrease in lifetime with decreasing emission wavelength[20] for example, extrapolation of data given in Ref.20 gives lifetimes less than 1 h at 690 nm.

4-3. Temperature Dependence of Threshold Current

4-3-1. Experimental results

Laser diodes used here are VSIS lasers emitting in the wavelength range of 781-697 nm. The difference of AlAs mole fraction Δx between the active and cladding layers was 0.3 and 0.4 for the devices emitting above and below 760 nm, respectively. The thickness of both the cap layer and the substrate of devices emitting below 760 nm was taken to be 50 μm in order to reduce the stress caused by the bonding process as described in §4-4. The pulsed threshold currents were determined in the temperature range of -110-80°C. The current pulses were 1-μs wide at a repetition rate of 1 kHz.

Examples of the measured temperature dependence of the threshold current are shown in Fig.9. The threshold-temperature characteristics of DH lasers are generally represented with the characteristic temperature T_0 in the form $I_{th} \propto \exp(T/T_0)$. VSIS lasers have different characteristic temperatures for three temperature ranges divided at two critical temperatures T_c; the low and high critical temperatures are denoted as T_{cl} and T_{ch}, respectively. Three characteristic temperatures are denoted as T_{0l}, T_{0m}, and T_{0h} for the low, middle, and high temperature ranges, respectively.

The variation of T_{cl} and T_{ch} with the lasing wavelength is shown in Fig.10. T_{ch} gradually decreases with decreasing the lasing wavelength,[5] whereas T_{cl} scatters and is almost independent of the lasing wavelength. Also with respect to the characteristic

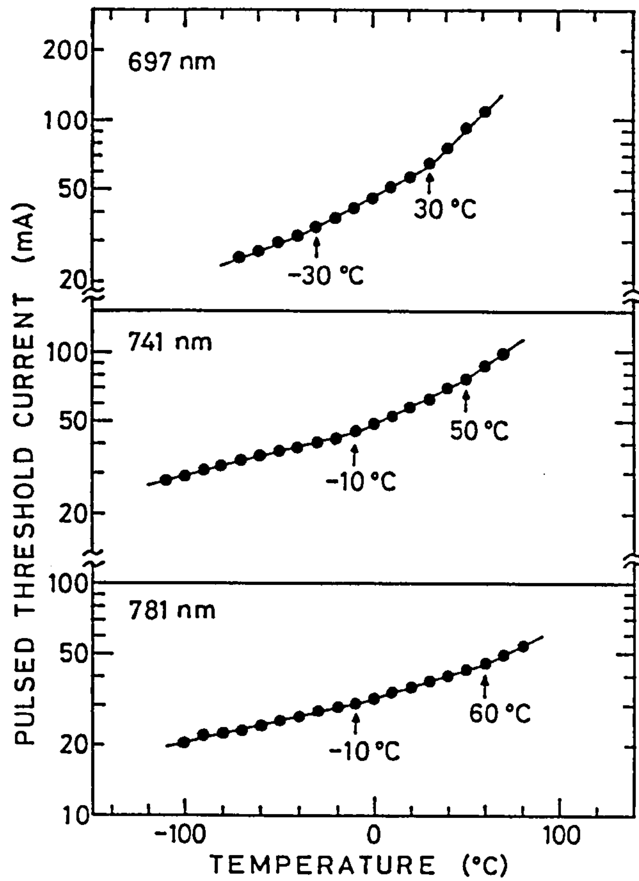

Fig.9 Temperature dependence of the threshold current of 697, 741, and 781 nm lasers.

temperatures, T_{0h} moderately decreases with decreasing the lasing wavelength, whereas T_{0m} and T_{0l} show considerable scatter and little or no dependence on the lasing wavelength, as depicted in Fig.11. These results demonstrate that T_0 and T_c do not necessarily characterize the temperature dependence of the threshold current, because the actual threshold-temperature sensitivity is represented by the combination of T_0 and T_c. Therefore, the threshold-temperature coefficient $I_{th}(T_1)/I_{th}(T_2)$ ($T_1 > T_2$) is a more appropriate and convenient measure for characterizing the threshold-temperature sensitivity than T_0 and T_c when the temperature range of $T_1 - T_2$ includes the critical temperature. Even when the temperature range under consideration includes one critical temperature, two characteristic temperatures as well as one critical temperature are required to represent the threshold-temperature characteristics completely. As shown in Fig.9, the temperature range which is important for many practical applications, for example 20-70°C, usually includes T_{ch}.

The temperature coefficient of $I_{th}(350\ K)/I_{th}(300\ K)$ is shown in Fig.12 as a function of the lasing wavelength. The datum of an oxide-stripe laser emitting at 830 nm (Δx=0.4), and the calculated results for Δx=0.4, which are described in §4-3-2 are also shown in the same figure. It should be noted that the threshold-temperature sensitivity increases below 750 nm with decreasing the lasing wavelength in spite of the fairly large Δx of 0.4. The temperature coefficient in the low temperature range $I_{th}(300\ K)/I_{th}(250\ K)$ is shown in Fig.13. $I_{th}(300\ K)/I_{th}(250\ K)$ has a tendency similar to $I_{th}(350\ K)/I_{th}(300\ K)$ dependence, although it scatters due to the scatter of the "background" threshold-temperature sensitivity which results from the temperature dependence of gain at the threshold in the case of without the loss of carrier confinement in the active layer; in the low temperature range, the threshold-temperature coefficient is mainly determined by the background temperature sensitivity, since the carrier leakage is negligible.

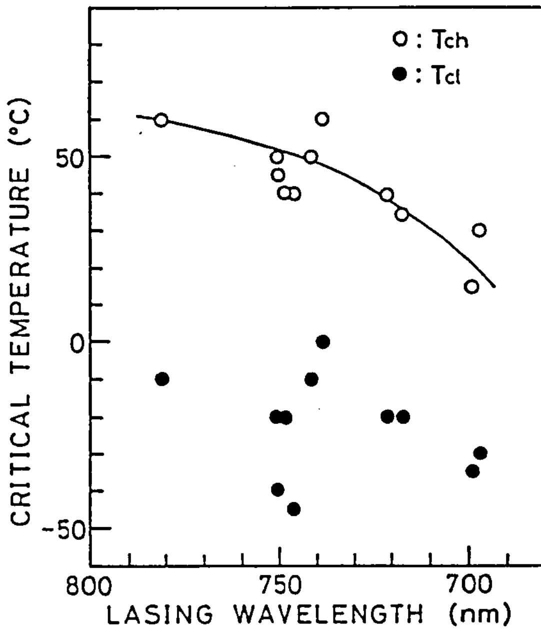

Fig.10 Relation between the lasing wavelength and the high and low critical temperatures T_{ch} and T_{cl}.

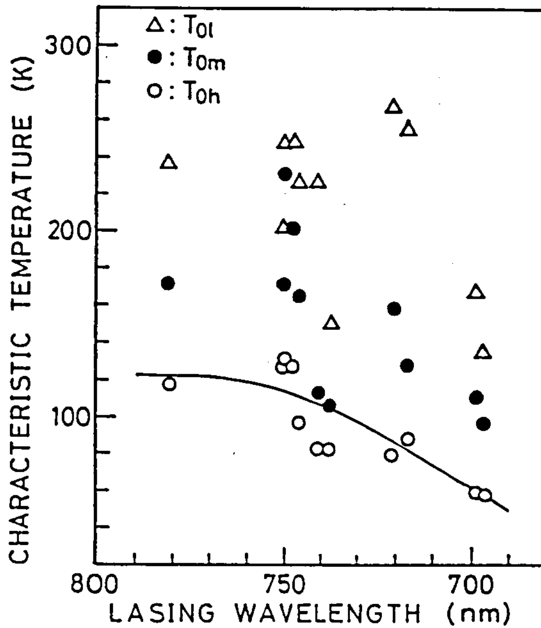

Fig.11 Variation of the characteristic temperature T_0 with the lasing wavelength. T_0's for the high, middle, and low temperature ranges are denoted as T_{0h}, T_{0m}, and T_{0l}, respectively.

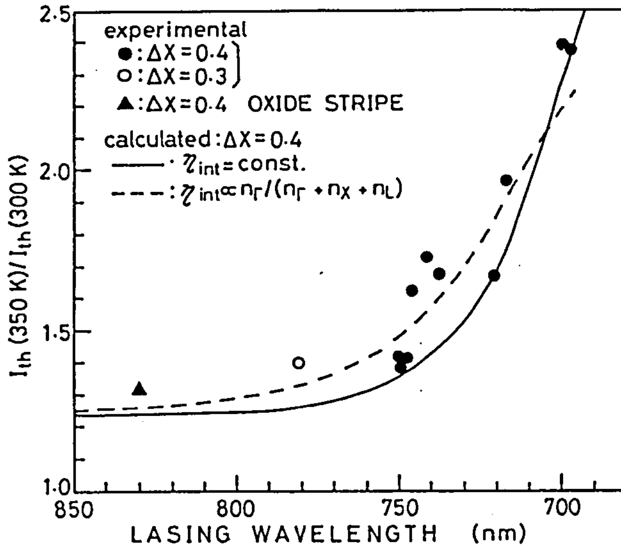

Fig.12 Experimental and calculated threshold-temperature coefficient I_{th} (350 K)/I_{th}(300 K) for the high temperature range as a function of the lasing wavelength.

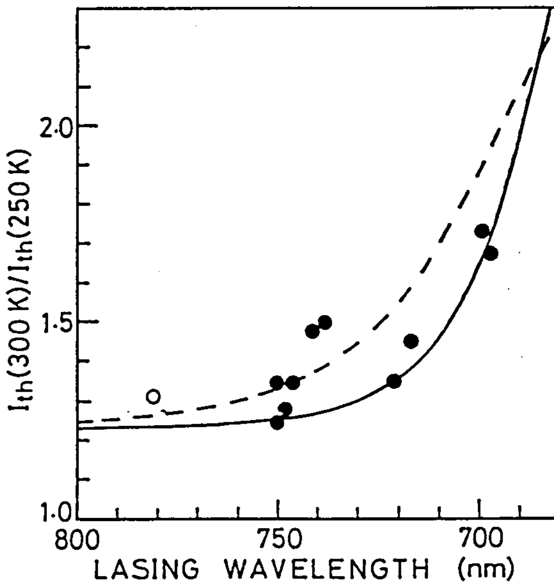

Fig.13 Experimental and calculated threshold-temperature coefficient I_{th}(300 K)/I_{th}(250 K) for the low temperature range as a function of the lasing wavelength. Notations are the same as those indicated in Fig.12.

4-3-2. Theoretical calculation

In order to explain the increase in the threshold-temperature sensitivity below 750 nm, the threshold-temperature coefficient was calculated using the model in which the diffusive leakage current due to unconfined carriers in the active layer was considered. Models for electron and hole leakage currents in the $Ga_{1-x}Al_xAs$/$Ga_{1-y}Al_yAs$ double heterostructure were given by Goodwin et al.[35] and Casey.[36] Both models described the leakage currents which were determined by minority-carrier diffusion in the cladding layers. Goodwin et al. considered electrons in the Γ direct conduction-band and the X indirect conduction-band, and holes in the valence band, and the difference in mobility of each carrier was taken into consideration. They calculated the temperature dependence of the threshold current density J_{th} on the assumption that the threshold current density J_{th_0} for no carrier leakage was expressed in the form $J_{th_0} \propto \exp(T/T_0)$. Casey considered the energy gaps for the direct conduction-band at Γ and the indirect conduction-bands at both X and L, and also assigned the carrier density of states effective masses for the conduction bands at Γ, X, and L, and for the valence band. However, he did not consider the difference in mobility for the different conduction bands. In the present calculation, the leakage currents have been calculated, on the basis of Casey's model, by considering the difference in mobility.

In order to calculate the temperature dependence of the leakage currents, expressions for the temperature dependence of the electron and hole concentrations in the active layer are necessary. It was assumed that the injected electron (minority carrier) concentration n_Γ in the direct conduction band of the active layer at the threshold can be expressed as[31]

$$n_\Gamma = 2\times10^{18} \exp\left(\frac{T-300}{2T_0}\right) \ \text{cm}^{-3}. \quad (3)$$

n_Γ was assumed to be proportional to the square root of the

threshold current density $J_{th_0\Gamma}$ for the direct-conduction-band electrons with no carrier leakage, which was taken to be

$$J_{th_0\Gamma} = 1000 \exp\left(\frac{T-300}{T_0}\right) \text{ A/cm}^2. \qquad (4)$$

The hole concentration in the active layer at the threshold can be obtained by using the charge neutrality condition in the active layer and thus it equals to the sum of the injected electron concentration and the hole concentration due to doping for the p-type active layer considered here. The carrier concentration in the active layer obtained in this manner determines the positions of the quasi-Fermi levels in the active layer.

The energy band diagram for the double heterostructure n-$Ga_{1-y}Al_yAs$/p-$Ga_{1-x}Al_xAs$/p-$Ga_{1-y}Al_yAs$ at forward bias is shown in Fig.14. In the case of the electron leakage in the p-$Ga_{1-y}Al_yAs$ layer, the electron concentration N_P^i for the i conduction band at the edge of the p-$Ga_{1-y}Al_yAs$ layer adjacent to the active layer is written in terms of the quasi-Fermi levels for electrons and holes in the active layer $F_n-E_{c_2}$ and $F_p-E_{v_2}$, respectively, as

$$N_P^i = (N_{cP}^i N_{vP}/P)\exp\{-(\Delta E_g+(F_p-E_{v_2})-(F_n-E_{c_2}))/kT\} \qquad (5)$$

for $i=\Gamma$, X, and L, where P is the hole concentration in the p-cladding layer outside the space charge region and ΔE_g is the difference of the energy gaps of p-$Ga_{1-x}Al_xAs$ and p-$Ga_{1-y}Al_yAs$. The quantities N_{cP}^i and N_{vP}^i are the effective densities of states in the conduction and valence bands of the p-$Ga_{1-y}Al_yAs$, respectively. In Eq.(5), P is assumed to be expressed by the Boltzmann form $P=N_{vP}\{-(F_p-E_{v_1})/kT\}$. The effective densities of states N_{cP}^Γ N_{cP}^X, and N_{cP}^L for the Γ, X, and L conduction bands, respectively, are given by

$$N_{cP}^\Gamma = 2(2\pi kT/h^2)^{3/2}(m_e^\Gamma)^{3/2}, \qquad (6)$$

$$N_{cP}^X = 2(2\pi kT/h^2)^{3/2}(m_e^X)^{3/2}\exp(-\Delta E^{X-\Gamma}/kT), \qquad (7)$$

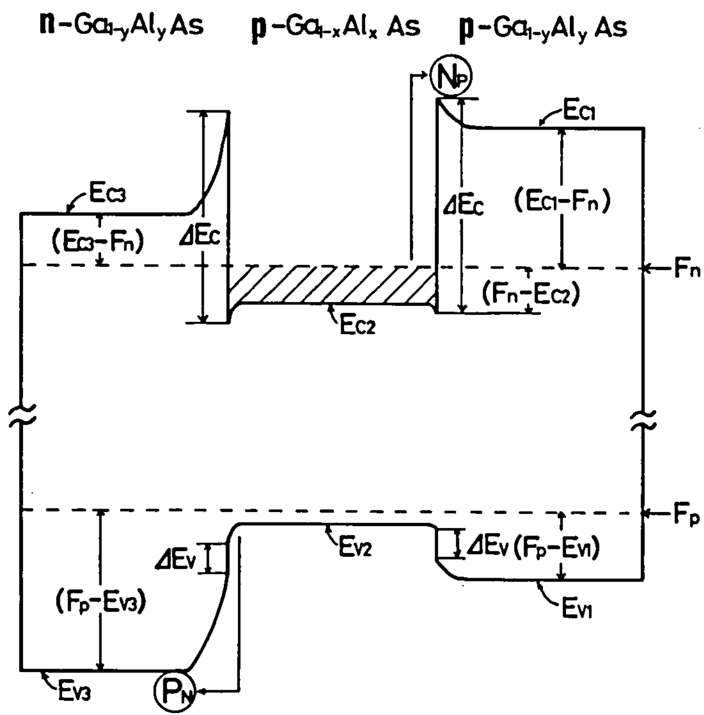

Fig.14 Energy-band diagram for a double heterostructure n-$Ga_{1-y}Al_yAs$/p-$Ga_{1-x}Al_xAs$/p-$Ga_{1-y}Al_yAs$ ($x<y$) at forward bias.

and

$$N_{cP}^{L} = 2(2\pi kT/h^2)^{3/2}(m_e^L)^{3/2}\exp(-\Delta E^{L-\Gamma}/kT) \quad (8)$$

where, $\Delta E^{X-\Gamma}=E_g^X-E_g^\Gamma$, and $\Delta E^{L-\Gamma}=E_g^L-E_g^\Gamma$. In these equations, m_e^i is the effective density of states mass and E_g^i is the energy gap for the i conduction band, where i=Γ, X, and L. The energy gaps and effective density of states masses have been given in Table II of Ref.36 as a function of x for the $Ga_{1-x}Al_xAs$. The diffusive electron leakage current density J_e^i, due to the electrons in the i conduction band in the p-$Ga_{1-y}Al_yAs$ layer adjacent to the active layer is given by

$$J_e^i = \frac{eD_e^iN_P^i}{L_e\tanh(w/L_e)}. \quad (9)$$

In Eq.(9), D_e^i is the electron diffusivity for the i conduction-band electrons in the p-$Ga_{1-y}Al_yAs$ layer, w is the p-cladding layer thickness, and L_e is the diffusion length for the electrons in the p-cladding layer. Eq.(9) is simplified as

$$J_e^i = \frac{eD_e^iN_P^i}{L_P} \quad (10)$$

where L_P is the effective diffusion length of the electrons in the p-cladding layer, and $L_P=w$ for $w<L_e$, and $L_P=L_e$ for $w>L_e$.

The Fermi level in the degenarated case is approximated by Joyce and Dixon[37] as

$$\begin{aligned}F_c-E_c = kT(&\ln(n/N_c) + 3.53553\times10^{-1}(n/N_c)\\ &-4.95009\times10^{-3}(n/N_c)^2 + 1.48386\times10^{-4}(n/N_c)^3\\ &-4.42563\times10^{-6}(n/N_c)^4) \end{aligned} \quad (11)$$

for the conduction band, where n is the electron concentration and N_c is the effective density of states for the conduction band. An expression similar to Eq.(11) can be written for the valence band.

Putting thus obtained quasi-Fermi levels into Eq.(5), and using Eqs.(6)-(8) and (10) give the electron leakage currents for the Γ, X, and L conduction bands in the p-$Ga_{1-y}Al_yAs$ layer. Expressions similar to Eqs.(5), (6), and (10) can be written for the hole leakage current J_h in the n-$Ga_{1-y}Al_yAs$ layer.

In the present calculation, only the diffusive leakage current is taken into consideration, but recently, Dutta has repoted that the drift leakage current in the p-cladding layer is important in determining the temperature dependence of the threshold current, especially when the p-cladding layer is resistive; that is, $p<4\times10^{17}$ cm^{-3}.[38] The drift in the p-cladding layer can be neglected in the VSIS laser because p is as high as 1×10^{18} cm^{-3}. For stripe-geometry lasers, lateral current spreading and carrier diffusion significantly affect the threshold.[39] However, the small change in the ratio of these current components to the total threshold current is neglected as being done in Ref.38.

The electron and hole diffusivities are required for the calculation of the threshold temperature dependence. The diffusivity D can be written in terms of the mobility μ by the relation $D=\mu kT/e$. The electron mobility μ_Γ of the Γ conduction band is affected by the concentration of the impurities due to the scattering by the ionized impurities. Pitt and Lees[40] have repoted that μ_Γ increases from 1850-8400 cm^2/V s with decreasing the carrier concentration from 4.6×10^{18} to 1.49×10^{13} cm^{-3} in GaAs at room temperature. Since the carrier concentration of the p-$Ga_{1-y}Al_yAs$ cladding layer was 1×10^{18} cm^{-3} in the lasers used in this study, μ_Γ was taken as 3000 cm^2/V s from Table I of Ref.40. The electron mobilities μ_X and μ_L of the X and L conduction bands were taken as $\mu_X=300$ and $\mu_L=700$ cm^2/V s, respectively, from data for $Ga_{0.77}Al_{0.23}As$ by Saxena.[41] Aspnes[42] has also obtained $\mu_X=300$ and $\mu_L=920$ cm^2/V s for GaAs, and these values are equal or close to the Saxena values. The electron diffusivities of respective conduction bands were thus obtained to be $D_e^\Gamma=78$, $D_e^X=8$, and $D_e^L=18$ cm^2/s at 300 K. The hole diffusivity D_h was taken as 4 cm^2/s from

Ref.36. The effective diffusion lengths of electrons and holes were assumed to be 1 μm, which is equal to the cladding layer thickness. Since the dependence of leakage carrier density on temperature is extremely great, the comparatively small variation of the diffusivities and diffusion lengths with temperature was neglected and they were treated as constants, independent of temperature.

The total threshold current density for no carrier leakage J_{th_0} is expressed as $J_{th_0} = J_{th_0\Gamma}/\eta_i$, where η_i is the internal quantum efficiency. η_i decreases below 750 nm since the separation between the direct and the indirect conduction-band-minima decreases with increasing AlAs mole fraction of the active layer. Two cases are considered here for the variation of η_i with the lasing wavelength. In one case, η_i is constant independent of the lasing wavelength. In another case, η_i is proportional to the fraction γ of the total electrons in the direct conduction band, which is given by Eq.(1) in §4-2-3. In this case, the decrease in η_i with temperature also increases the threshold-temperature sensitivity. Calculated results are shown for both cases in Figs.12 and 13. The background T_0 in Eqs.(3) and (4) was taken to be 240 K. This value is a typical T_{0_1} for the devices emitting above 700 nm, as shown in Fig.11. The lasing photon energy was taken to be the energy gap at 300 K minus 20 meV.[44]

4-3-3. Discussion

The calculated results agree with experimental ones fairly well, as demonstrated in Figs.12 and 13, especially in Fig.12 for the high temperature range. This agreement confirms that the increase in the threshold-temperature sensitivity below 750 nm principally results from the increase in the leakage current due to unconfined carriers in the active layer. In the case of constant Δx of 0.3-0.4, the electron leakage in the indirect conduction bands in the p-cladding layer and the hole leakage in the n-clad-

ding layer rapidly increase with decreasing the lasing wavelength below 750 nm. This is caused by the increase in the effective density of states of the conduction band and the decrease in the difference of the energy gaps ΔE_g of the active and cladding layers.

In the case of constant Δx, ΔE_g decreases with decreasing the lasing wavelength when the energy gap of the cladding layer is indirect, because the X indirect energy gap increases more slowly with the AlAs mole fraction than the Γ direct energy gap. When ΔE_g is kept constant, the leakage current density is maximum at the indirect-direct crossover of the cladding layer, where energy gaps for the Γ, X, and L conduction bands are almost the same, and thus the effective density of states of the conduction band is maximum. Therefore, the threshold-temperature coefficient $I_{th}(350\ K)/I_{th}(300\ K)$ in the case of constant ΔE_g should take the maximum at the lasing wavelength corresponding to the indirect-direct crossover of the cladding layer, as shown in Fig.15.

Finally, the effect of the change of η_i on the threshold-temperature sensitivity is examined. Calculated $I_{th}(350\ K)/I_{th}(300\ K)$ is shown in Figs.16(a) and 16(b) for the cases of η_i=constant and $\eta_i \propto \gamma$, respectively. Figure 16(a) demonstrates that in the case of constant η_i, the leakage current decreases with Δx, and thus the temperature coefficient decreases with Δx, especially below 750 nm. However, the experimental variation of I_{th} with the lasing wavelength in (GaAl)As DH lasers so far reported[44-47] indicates that η_i is almost proportional to γ, which has considerable temperature dependence in the short wavelength range; the broken line in Fig. 16(b) for no leakage current represents the temperature dependence of γ. Therefore, in the real case, the threshold-temperature sensitivity is limited by the temperature dependence of γ, even when Δx is large enough for preventing the carrier leakage ($\Delta x > \sim 0.6$). Comparison of Figs.16(a) and 16(b) also indicates that $I_{th}(350\ K)/I_{th}(300\ K)$ is almost determined by the leakage current when Δx is smaller than ~ 0.4.

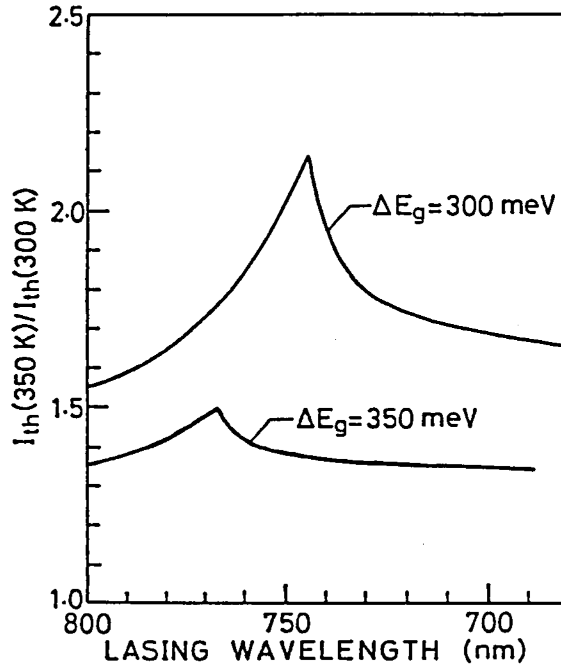

Fig.15 Calculated $I_{th}(350\ K)/I_{th}(300\ K)$ for ΔE_g=constant and η_i=constant. In the case of ΔEg=350 meV, the shortest wavelength is limited by the AlAs mole fraction of unity in the cladding layer.

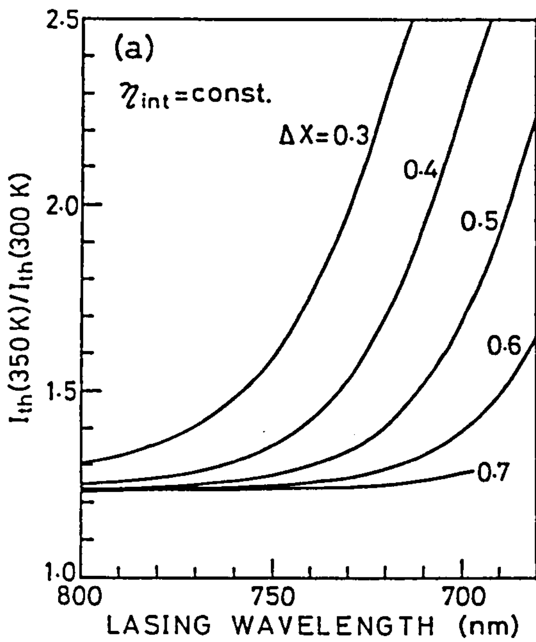

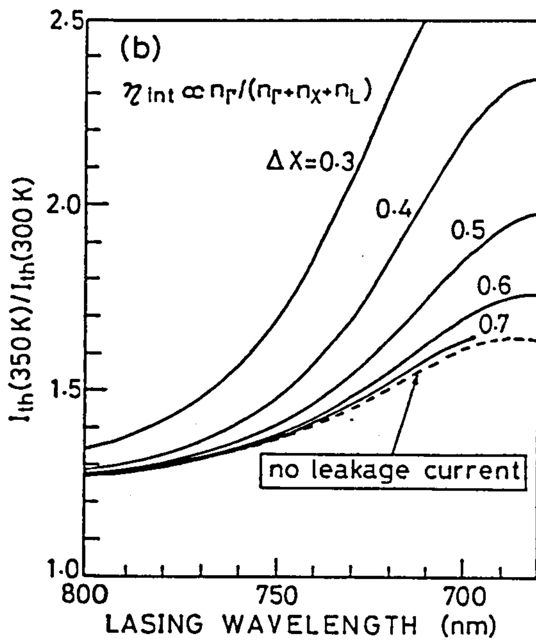

Fig.16 Calculated I_{th}(350 K)/I_{th}(300 K) for (a) η_i=constant, and $\eta_i \propto n_\Gamma/(n_\Gamma+n_X+n_L)$. The shortest wavelength for x=0.7 corresponds to the AlAs cladding layer.

4-4. Lifetime

The variation of the active layer stress with the external force was calculated using the cylindrically bending six-layer structure shown in Fig.17. The external layer, which acts as the solder and the heat sink , contracts and causes the bonding stress in the active layer. The active layer stress σ_3 was calculated using the closed form solution obtained by Olsen and Ettenberg,[48] which is expressed as

$$\sigma_3 = E\left(\sum_{i=1}^{6}\left(\frac{t_i \varepsilon_{i3}}{t} + \frac{t_i \kappa_i}{2R}\right)\right), \qquad (12)$$

where
$$\begin{cases} \kappa_i = +1 & i<3 \\ = 0 & i=3 \\ = -1 & i>3 \end{cases},$$

$$t = \sum_{i=1}^{6} t_i , \qquad (13)$$

and
$$R = t^3\left(6\sum_{i=1}^{6}\sum_{i>j}^{6} t_i t_j \varepsilon_{ij}\right)^{-1}. \qquad (14)$$

In Eqs.(12) and (14), $\varepsilon_{ij}=\varepsilon_i-\varepsilon_j$ is the difference between strains ε_i for ith layer in Fig.17. The elastic modulus E was assumed to be equal for all layers and 1×10^{12} dyn cm^{-2}. ε_i caused by the temperature change of 780°C from the growth temperature to room temperature was assumed.

When the external force is not imposed, that is, $t_6=0$, the compressive stress in the active layer increases as the AlAs mole fraction x in the active layer is increased above 0.03 as depicted in Fig.18. However, the stress in the active layer does not increases so rapidly as the lasing wavelength is decreased from 780 nm(x=0.15) to less than 750 nm(x<0.2). Actually lifetime of laser diodes decreases rapidly in the short wavelength region below 750 nm.[14,20] Therefore, it is not likely that the slight increase in

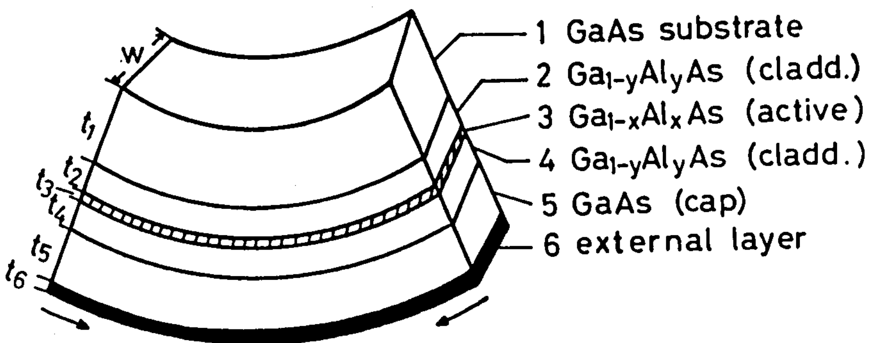

Fig.17 Multilayered structure used for stress calculation.

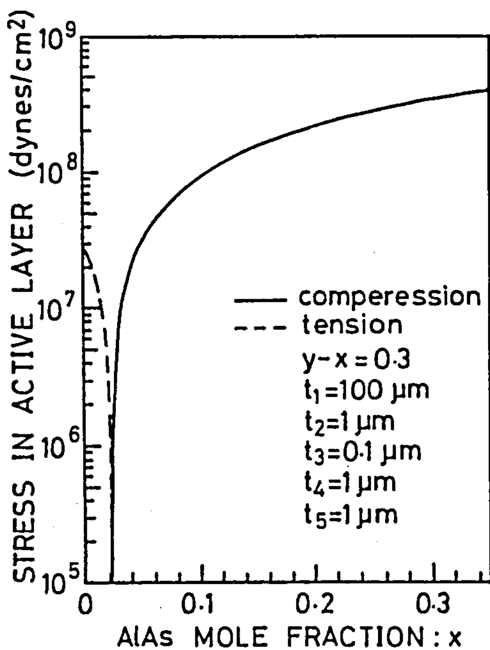

Fig.18 Variation of the active layer stress with the AlAs mole fraction, x in the active layer in the case of no external force ($t_6=0$). Heterojunction step height $\Delta x=y-x$ is kept constant at 0.3.

the stress strongly causes the degradation.

The variation of the active layer stress with the external force is shown in Fig.19 for x=0.2 and y=0.5 (λ=750 nm). The thicknesses of the substrate t_1 and the cap layer t_5 are varied under the condition t_1+t_5=100 μm; therefore the position of the double heterostructure in the wafer is changed. In the case of conventional junction-down bonding (t_1, t_5=1, 99 μm), the active layer stress increases rapidly with the external force. The active layer stress caused by the external force decreases with an increase in the thickness of the cap layer t_5. In the case of junction-up bonding with small t_1, however, the compressive stress decreases to zero and then the tensile stress increases with an increase in the external force. The tensile stress degrades the laser device more strongly than the compressive stress.[48] When In solder (3 μm thick) and Cu heat sink (1 mm thick) are used, the external force caused by a temperature change of 130°C was estimated to be in the range of 10^6-10^7 dyn/cm. This range includes the uncertainty of the plastic deformation of the In solder. In actual devices, the active layer stress can be reduced by fabricating the double heterostructure in the appropriate region in the wafer.

The effect of the "buffer layer"[21,22] was also examined when the external force is imposed onto the wafer. The cladding layer itself acts as the buffer layer as shown in Fig.20. The stress in the active layer considerably decreases with increasing t_2 or t_4 to the appropriate values in the case of no external force (t_6=0). The variation of the active layer stress with the external force for different thicknesses of the cladding layer t_4 is shown in Fig.21. The active layer stress considerably decreases with increasing t_4 when the external force is small. When the external force is greater than 10^6 dyn/cm, the effect of the buffer layer is weak. In this case, the thick cap layer and the thinned substrate are more effective than the buffer layer for reducing the active layer stress.

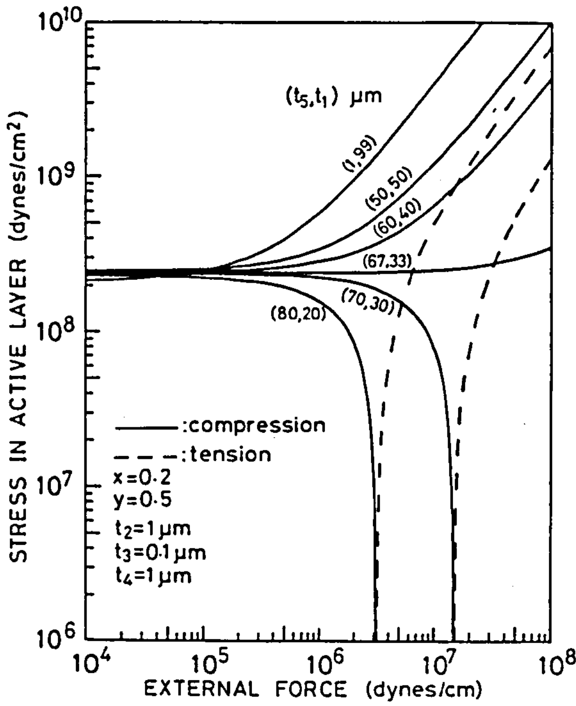

Fig. 19 Stress in the active layer as a function of external force per unit length. The thicknesses of the active and cladding layers are 0.1 and 1 μm, respectively, and the thicknesses of the substrate and the cap layer are varied as parameters. AlAs mole fractions in the active and cladding layers are 0.2 and 0.5, respectively.

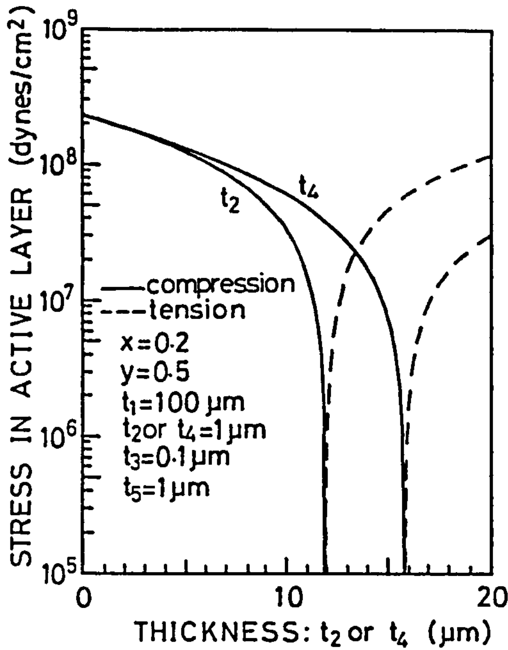

Fig. 20 Stress in the active layer as a function of the cladding layer thickness t_2 and t_4 in the case of no external force (t_6=0).

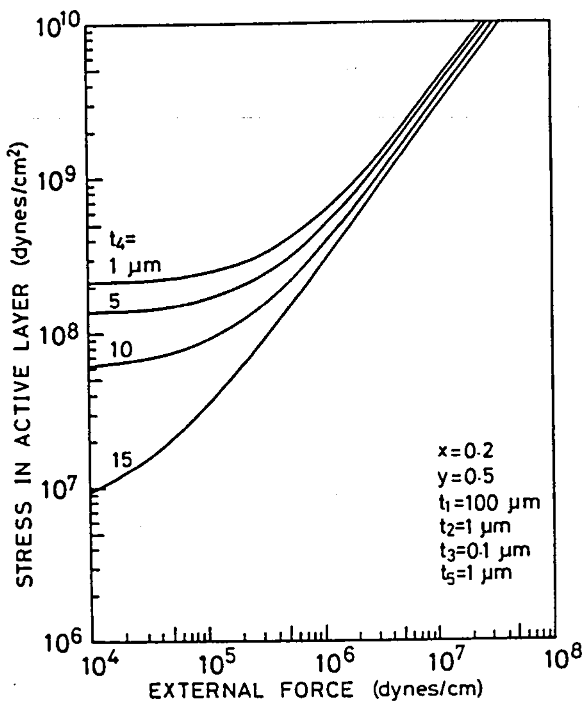

Fig. 21 Stress in the active layer as a function of external force for different thicknesses of the cladding layer t_4.

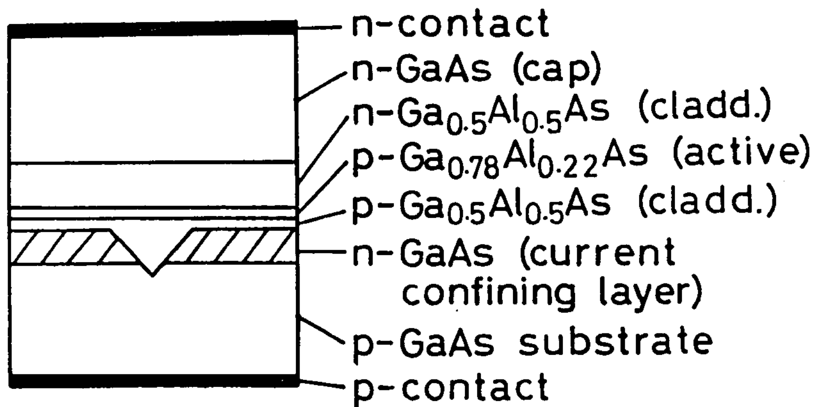

Fig. 22 Schematic cross section of v-channeled substrate inner stripe laser.

VSIS lasers emitting at 740 nm with the thick cap layer and the thinned substrate were fabricated. The device structure is schematically illustrated in Fig.22. Two types of devices were prepared: Type I with the thin cap layer and type II with the thick cap layer. For both types, the thicknesses of the active layer and n-cladding layer were 0.08 and 1 μm, respectively, and that of the p-cladding layer was 0.15 μm outside the channeled region and ∿1 μm at the center of the channel. The thicknesses of the cap layer and the substrate were 3 and ∿120 μm for type I and ∿40 and ∿80 μm for type II, respectively; type II device is not optimized with respect to the bonding stress. The VSIS structure is favorable for fabricating the device with the thick cap layer, since the inner current stripe prevents the current from laterally spreading in the cap layer. Therefore, electro-optical characteristics were the same in both types of devices. In addition, the thick cap layer also has the advantage of reducing the stress caused by the alloying process of the n-contact (AuGe/Ni/Au).

Al_2O_3 facet coating was made to both mirror surfaces with electron beam evaporation. Laser chips were bonded on Mo/Au coated Cu heat sinks (1 mm thick) with In solder (∿3 μm thick) n-side down; the n-contact was also coated with Mo/Au. These cares were taken to eliminate the deterioration of In solder.[49]

Type I devices from three lots and type II devices from two lots were life tested at an output power of 5 mW/facet in the 50°C laboratory ambient. Aging results shown in Fig.23 clearly demonstrate that the degradation rate is dramatically decreased by the introduction of the thick cap layer and the thinned substrate. The median degradation rate is more than one order of magnitude smaller for type II than type I.

4-5. Summary

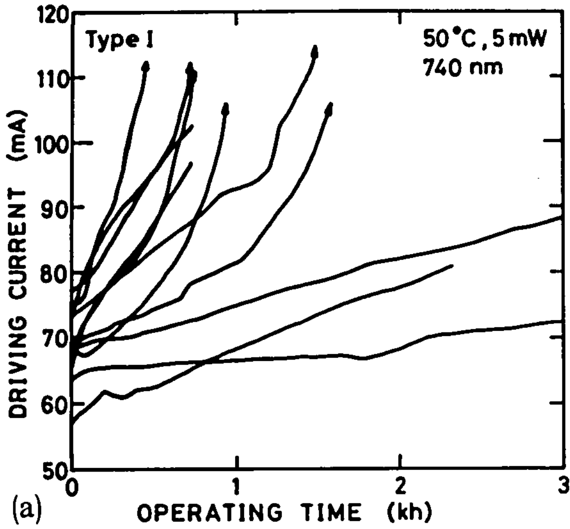

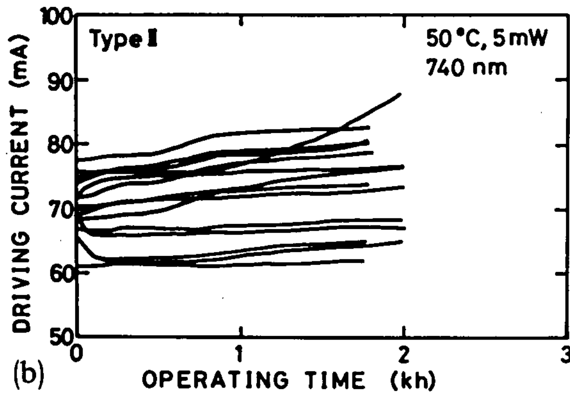

Fig.23 Aging results of VSIS lasers emitting at 740 nm (a) with the thin cap layer (type I) and (b) with the thick cap layer (type II).

Fundamental properties of VSIS lasers emitting below 750 nm have been studied. The variation of the low-current-threshold of VSIS lasers with the lasing wavelength agrees with that of $1/\eta_i$ calculated using the energy-band parameters where the indirect-direct crossover is assigned at the AlAs mole fraction of 0.45. cw operation has been achieved at as short as 688 nm. The cause of the increase in the threshold current of conventional stripe lasers on n-type substrate has been discussed based on the results of photolumunescence, Al-profiles in the active layer, and the lateral current spreading, which depends on the device structure. The temperature dependence of the threshold current has been measured for VSIS lasers emitting in the wavelength range of 781-697 nm. The threshold-temperature coefficient $I_{th}(350\ K)/I_{th}(300\ K)$ was found to increase below 750 nm with decreasing the lasing wavelength in spite of the fairly large heterojunction step height of 0.4. This tendency was well explained by the model of carrier leakage due to unconfined carriers in the active layer, and is inherent in the indirect band-gap (GaAl)As cladding layers. The factors which determine the threshold-temperature sensitivity have been examined on the basis of the calculated results. It has been demonstrated that lifetimes of VSIS lasers emitting at 740 nm can be improved by setting the thicknesses of the cap layer and the substrate at the appropriate values to reduce the active layer stress caused by the bonding process according to the calculation.

References

1) H.Kressel and F.Z.Hawrylo, Appl. Phys. Lett. 17, 169 (1970).
2) B.I.Miller, J.E.Ripper, J.C.Dyment, E.Pinkas, and M.B.Panish, Appl. Phys. Lett. 18, 403 (1971).
3) H.Kressel and F.Z.Hawrylo, Appl. Phys. Lett. 28, 598 (1976).
4) T.Kajimura, T.Kuroda, S.Yamashita, M.Nakamura, and J.Umeda, Appl. Opt. 18, 1812 (1979).
5) M.Wada, K.Itoh, H.Shimizu, T.Sugino, and I.Teramoto, IEEE J.

Quantum Electron. QE-17, 776 (1981).

6) W.T.Tsang, J. Appl. Phys. 51, 917 (1980).

7) R.Chin, N.Holonyak, Jr., R.M.Kolbas, J.A.Rossi, D.L.Rossi, D.L.Keune, and W.O.Groves, J. Appl. Phys. 49, 2551 (1978).

8) S.Mukai, H.Yajima, and J.Shimada, Jpn. J. Appl. Phys. 20, L729 (1981).

9) M.Shimura, A.Fujimoto, H.Yasuda, and S.Yamashita, Jpn. J. Appl. Phys. 21, L338 (1982).

10) H.Kressel, G.H.Olsen, and C.J.Nuese, Appl. Pjys. Lett. 30, 249 (1977).

11) G.B.Stringfellow, J. Cryst. Growth 58, 194 (1982).

12) P.M.Petroff and R.A.Logan, J. Vac. Sci. Technol. 17, 1113 (1980).

13) W.T.Tsang and J.A.Ditzenberger, Appl. Phys. Lett. 39, 193 (1980).

14) T.Hayakawa, N.Miyauchi, S.Yamamoto, H.Hayashi, S.Yano, and T.Hijikata, J. Appl. Phys. 53, 7224 (1982).

15) C.Y.Chen and S.Wang, J. Appl. Phys. 52, 614 (1981).

16) H.Kressel, F.Z.Hawrylo, M.S.Abrahams, and C.J.Buiocchi, J. Appl. Phys. 39, 5139 (1968).

17) W.R.Wagner, J. Appl. Phys. 49, 173 (1978).

18) R.A.Logan, N.E.Schumaker, C.H.Henry, and F.R.Merritt, J. Appl. Phys. 50, 5970 (1979).

19) T.Hayakawa, S.Yamamoto, H.Hayashi, T.Sakurai, and T.Hijikata, IEEE J. Quantum Electron. QE-17, 2205 (1981).

20) T.Kajimura, J. Appl. Phys. 51, 908 (1980).

21) H.Shimizu, K.Itoh, M.Wada, T.Sugino, and I.Teramoto, IEEE J. Quantum Electron. QE-17, 763 (1981).

22) I.Ladany, T.R.Furman, and D.P.Marinelli, Electron. Lett. 15, 342 (1979).

23) K.Itoh, M.Wada, T.Sugino, and H.Shimizu, Nat. Tech. Rep. (Japan) 25, 1098 (1979) (in Japanese).

24) H.Kressel and J.K.Butler, Semiconductor Lasers and Heterojunction LED's (Academic, New York, 1977), p.418.

25) R.Dingle, R.A.Logan, and J.R.Arther, Jr., Proceedings of the 6th International Symposium on Gallium Arsenide and Related Compounds, IOP Conf. Ser. No.33a (IOP, London, 1977), p.210.

26) R.Dingle, R.A.Logan, and R.J.Nelson, Solid State Commun. 29, 171 (1979).

27) H.Temkin and V.G.Keramidas, J. Appl. Phys. 51, 3269 (1980).

28) H.C.Casey, Jr. and M.B.Panish, Heterostructure Lasers, Part A

(Academic, New York, 1978), p.192.

29) Effective masses were also taken from Refs.24 and 28 for each calculation. In these calculations, n_Γ was taken to be 2×10^{18} cm^{-3}, although n_Γ was taken to be 1.5×10^{18} cm^{-3} in Ref.24. However, the assignment of the indirect-direct crossover more strongly affects the calculated $1/\eta_i$ than n_Γ.

30) F.Stern, J. Appl. Phys. 47, 5382 (1976).

31) C.J.Hwang and J.C.Dyment, J. Appl. Phys. 44, 3240 (1973).

32) D.Botez, IEEE J. Quantum Electron. QE-17, 2290 (1981).

33) L.Figueroa and S.Wang, Appl. Phys. Lett. 31, 45 (1977).

34) S.Yamamoto, H.Hayashi, S.Yano, T.Sakurai, and T.Hijikata, Appl. Phys. Lett. 40, 372 (1982).

35) A.R.Goodwin, J.R.Peters, M.Pion, G.H.B.Thompson, and J.E.A. Whiteaway, J. Appl. Phys. 46, 3126 (1975).

36) H.C.Casey, Jr., J. Appl. Phys. 49, 3684 (1978).

37) W.B.Joyce and R.W.Dixon, Appl. Phys. Lett. 31, 354 (1977).

38) N.K.Dutta, J. Appl. Phys. 52, 70 (1981).

39) W.B.Joyce, J. Appl. Phys. 51, 2394 (1980).

40) G.D.Pitt and J.Lees, Phys. Rev. B 2, 4144 (1970).

41) A.K.Saxena, Appl. Phys. Lett. 36, 79 (1980).

42) D.E.Aspnes, Phys. Rev. B 14, 5331 (1976).

43) This value was estimated from the calculated gain spectrum by Stern: F.Stern, J. Appl. Phys. 47, 5382 (1976).

44) S.Yamamoto, H.Hayashi, T.Hayakawa, N.Miyauchi, S.Yano, and T.Hijikata, Appl. Phys. Lett. 41, 796 (1982).

45) T.Hayakawa, S.Yamamoto, H.Hayashi, N.Miyauchi, S.Yano, and T.Hijikata, J. Appl. Phys. 54, 2209 (1983).

46) R.D.Burnham, D.R.Scifres, and W.Streifer, Appl. Phys. Lett. 41, 228 (1982).

47) S.W.Kirchoefer, K.Meehan, N.Holonyak, Jr., D.A.Gulino, H.G. Drickamer, R.D.Burnham, and D.R.Scifres, Appl. Phys. Lett. 41, 406 (1982).

48) G.H.Olsen and M.Ettenberg, J. Appl. Phys. 48, 2543 (1977).

49) T.Hayakawa, S.Yamamoto, S.Matsui, T.Sakurai, and T.Hijikata, Jpn. J. Appl. Phys. 21, 725 (1982).

V. MODE CHARACTERISTICS OF LARGE-OPTICAL-CAVITY V-CHANNELED SUBSTRATE INNER STRIPE LASERS

5-1. Introduction

Semiconductor lasers are classified into gain-guided lasers and index-guided lasers from the viewpoint of the waveguiding mechanism. In general, gain-guided lasers oscillate on multi-longitudinal modes and fairly stable with optical feedback, whereas index-guided lasers show a single longitudinal-mode and instability with optical feedback.[1-4] For physical understanding of semiconductor lasers, it is interesting to investigate what factor determines mode characteristics. For practical applications, it is desirable that above properties can be seperately controlled by changing device parameters.

It is described in §3-3 that v-channeled substrate inner stripe (VSIS) lasers show multimode oscillating behavior slightly above the threshold in spite of their index-guiding structure, and also these longitudinal-mode characteristics vary with the magnitude of the built-in effective-index difference parallel to the junction plane.

In this chapter, the author further studies on mode characteristics of VSIS lasers in which the built-in refractive-index difference is varied by the introduction of the large-optical-cavity (LOC) structure.[5-7] The longitudinal mode and noise properties of these devices have been investigated. The effect of the current distribution upon the transverse mode has been examined by measuring the temperature dependence of the far-field pattern. These experiments reveal that the transverse mode and the longitudinal mode have different dependence on the waveguiding parameter, that is, the built-in refractive-index difference parallel to the

junction plane.

5-2. Design and Fabrication

The confinement factor Γ in the four-layer slab waveguide was calculated in order to obtain the condition for the fundamental transverse mode operation in the direction perpendicular to the junction plane.[8] Figure 1 depicts the four-layer slab waveguide for the LOC laser emitting at 780 nm considered here. The AlAs mole fraction of the cladding layer adjacent to the active layer is taken to be higher than that of the cladding layer adjacent to the optical guide layer in order to suppress the oscillation of the higher-order transverse mode. In the caculation, no approximation was employed and the refractive index of $Ga_{1-x}Al_xAs$ was assumed to follow 3.648-0.633x from data in Ref.9.

The variation of Γ with the thickness of the guide layer g is shown in Fig.2 for different AlAs mole fraction x of the guide layer. The thickness of the active layer d is 0.08 μm, which is employed in the present experiments. When g is smaller than a certain value g_0, Γ of the first-order transverse mode is smaller than that of the fundamental mode or the first-order mode is cutoff. As x is increased, g_0 becomes larger, and therefore the fundamental transverse mode oscillation is expected in the wider range of g. x is taken to be 0.35 for obtaining the fundamental mode in the fairly wide range of g. Figure 3 shows Γ in the case of x=0.35 for different d's. The scatter of d does not affect g_0 and slightly changes the cutoff thickness for the first-order mode oscillation. In this case, g_0 less than ∿0.6 μm could support the fundamental mode.

Regular VSIS lasers without a guide layer and two types of LOC-VSIS lasers were fabricated for varying the magnitude of the

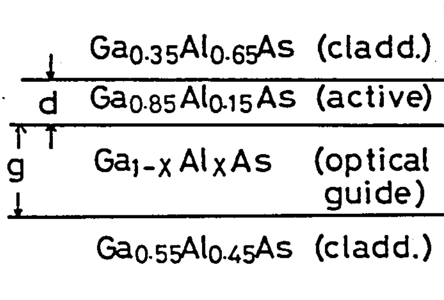

Fig.1 Representation of the four-layer slab waveguide for the 780 nm LOC laser considered in the present study.

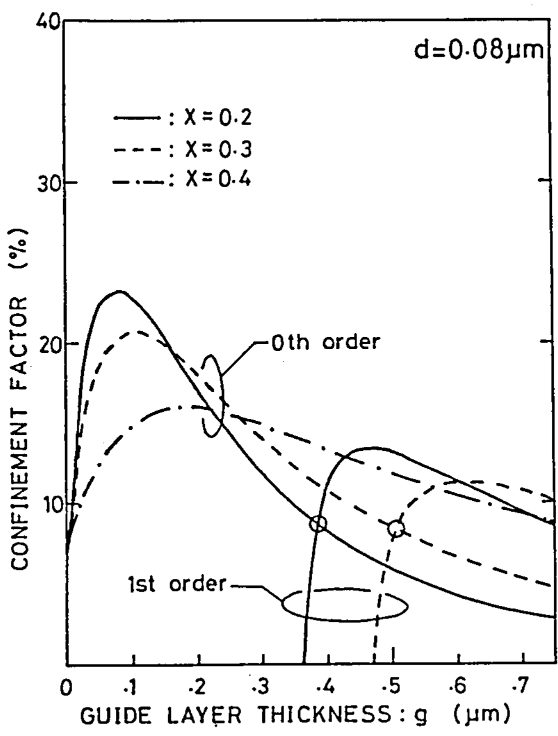

Fig.2 Confinement factor Γ as a function of guide layer thickness. The AlAs mole fraction in the guide layer is given by x. Open circles indicate that Γ is equal for the fundamental and the first order transverse modes and thus give g_0.

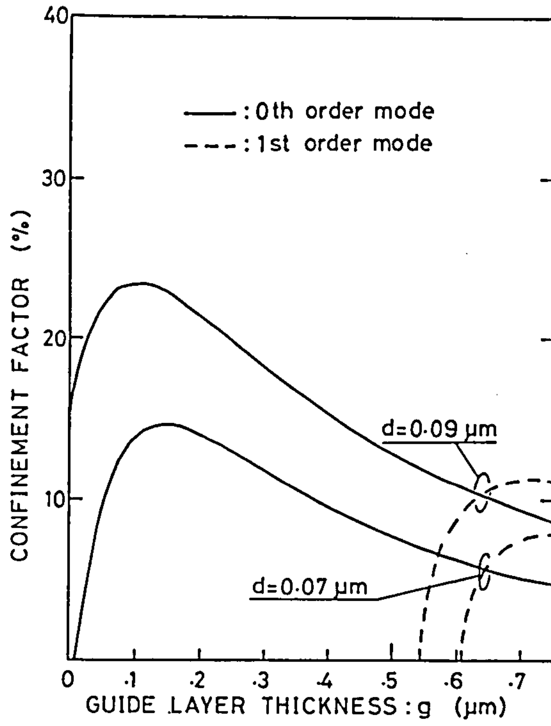

Fig. 3 Confinement factor as a function of guide layer thickness for active layer thicknesses d of 0.07 and 0.09 μm. The AlAs mole fraction in the guide layer is 0.35.

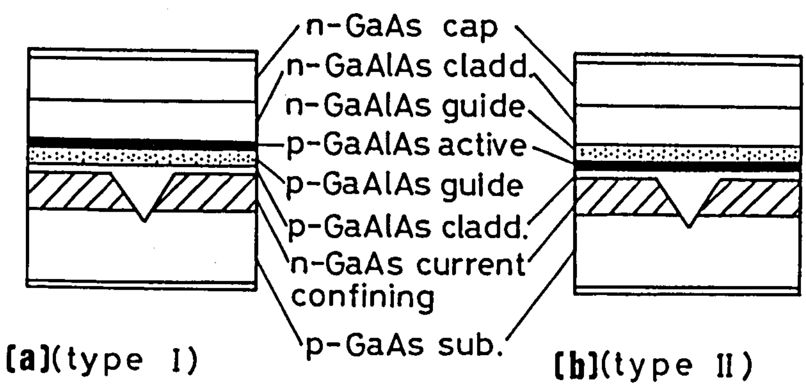

Fig. 4 Schematic cross section of (a) type I and (b) type II LOC-VSIS laser.

built-in refractive-index difference. Regular devices have the symmetric three-layer slab waveguide, which consists of a p-$Ga_{0.85}Al_{0.15}As$ active layer and $Ga_{0.55}Al_{0.45}As$ cladding layers as described in §3-2. Both types of LOC-VSIS lasers have the asymmetric four-layer slab waveguide shown in Fig.1. In type I devices shown in Fig.4(a), the slab waveguide consists of a p-$Ga_{0.55}Al_{0.45}As$ cladding layer (0.15 μm thick outside the v-channel), a p-$Ga_{0.65}Al_{0.35}As$ optical guide layer (0.14, 0.27, or 0.52 μm thick), a p-$Ga_{0.85}Al_{0.15}As$ active layer (0.08 μm thick), and an n-$Ga_{0.35}Al_{0.65}As$ cladding layer (1 μm thick). In type II devices shown in Fig.4(b), the slab waveguide is constructed in the reverse order against type I devices and consists of a p-$Ga_{0.35}Al_{0.65}As$ cladding layer (0.15 μm thick outside the v-channel), a p-$Ga_{0.85}Al_{0.15}As$ active layer (0.08 μm thick), an n-$Ga_{0.65}Al_{0.35}As$ optical guide layer (0.32 μm thick), and an n-$Ga_{0.55}Al_{0.45}As$ cladding layer (1 μm thick). The v-shaped channel was 4 μm wide and 1 μm deep in all types of devices.

In a wafer of type I devices nominally with g=0.52 μm, some devices probably with g thicker than 0.6 μm operated on the first-order transverse mode as expected from Fig.3. The devices showing the fundamental transverse mode oscillation were selected for the present experiments.

In the VSIS structure, built-in refractive-index difference is caused by the fact that outside the channeled region, the evanescent tails of the lasing light reach the current confining layer, which is absorptive and has higher refractive index than slab waveguide layers. Thus, it is possible to control the built-in refractive-index difference by varying the shape of evanescent tails on the side of the current confining layer. Figure 5 illustrates the variation of the optical intensity distribution in the four-layer slab waveguide shown in Fig.1 (x=0.35) with the thickness of the guide layer g. As g is increased, more of the light intensity is inside the guide layer, and less of the light spreads to the cladding layer adjacent to the guide layer. Therefore, in

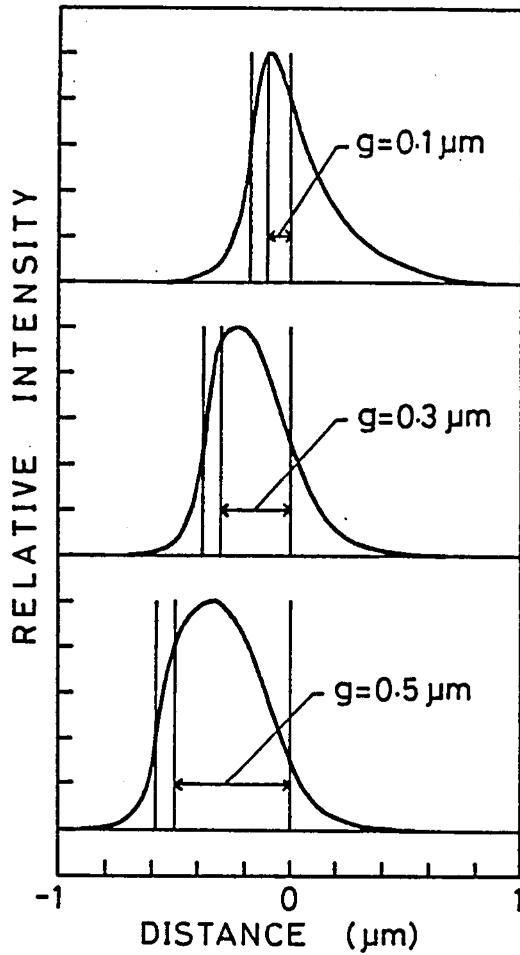

Fig.5 Square of the electric field as a function of position within the slab waveguide for the guide layer thicknesses of 0.1, 0.3 and 0.5 µm.

type I LOC-VSIS lasers, the built-in refractive-index difference decreases, as g is increased. The calculated optical intensity distribution indicates that in the range of $\sim 0.1\ \mu m < g < \sim 0.5\ \mu m$, the built-in refractive-index difference would be smaller for type II LOC devices and larger for regular VSIS lasers than type I LOC-VSIS devices.

Major characteristics of the devices employed in this study are summarized in Table I. In the regular VSIS and type I LOC-VSIS lasers, threshold current I_{th} increases with g since the lateral current spreading in the guide layer increases and the built-in refractive-index difference increases, that is, the spot size increases as g is increased. The threshold current of type II LOC-VSIS laser with g=0.32 μm is smaller than that of type I LOC-VSIS laser with g=0.52 μm due to tight current confinement of type II LOC devices like the regular VSIS laser. The differential quantum efficiency η_d also tends to increase with decreasing the built-in refractive-index difference. This is attributed to the fact that the decrease in the built-in refractive-index difference is always accompanied by the decrease in the built-in loss difference in the devices like the channeled substrate planar (CSP) laser.[10)]

5-3. Mode Characteristics

In this section, the effect of the change in built-in refractive-index difference upon the transverse and longitudinal mode behaviors is studied in detail. The VSIS laser belongs to a "weakly" index-guided lasers like a CSP laser[10,11)] and a separated multiclad layer (SML) stripe laser.[12)] Because these structures utilize the optical coupling outside the channeled region of the active layer and another GaAs layer which are separated by the thin cladding layer. Thus the refractive-index difference is not so large as that in lasers with a buried active layer[13,16)] or

Table I Threshold currents I_{th} and differential quantum efficiensies η_d of VSIS and LOC-VSIS lasers.

Type	g µm	I_{th} mA	η_d %
VSIS	0	35-45	41-47
Type I LOC-VSIS	0.14	59-81	41-48
	0.27	70-90	35-44
	0.52	154-200	40-70
Type II LOC-VSIS	0.32	116-130	60-79

with the large thickness variation of the active or waveguide layer parallel to the junction plane.[6,17] Moreover, the current is strongly confined in the VSIS laser with an internal current channel. These features lead to the multimode oscillation slightly above the threshold as described in §3-3. In the CSP-like structure, it is rather easy to vary the magnitude of the built-in refractive-index difference by changing the thickness of the active, guide, or cladding layer or varying the AlAs mole fraction of the guide or cladding layer.

The VSIS structure is considered to be suitable for reducing the built-in refractive-index difference while maintaining the fundamental transverse mode parallel to the junction plane, since an internal current confining channel is self-aligned with a built-in optical waveguide. When the built-in refractive-index difference is decreased, the gain distribution which is miss-aligned with the built-in optical waveguide could disturb the fundamental mode oscillation in the lasers in which a narrow stripe contact is formed on a wafer after the waveguide formation using a mask alignment process as reported by Chen and Wang.[18] The near-field intensity profile was observed at several output powers below 10 mW at 20°C using the setup similar to that described in Ref.18. The near-field patterns showed that all the devices stably operate in the fundamental transverse mode at least below 10 mW and the mixture of the first-order transverse mode caused by the nonuniform current distribution discussed in Ref.18 was not found.

Figure 6 shows the dependence of the longitudinal spectral envelope full-width half-maximum (FWHM) on the light output power measured at 20°C. In this figure, devices are listed in the order of smaller built-in refractive-index difference; that is, from VSIS to type II LOC-VSIS lasers. Except in the type II LOC-VSIS laser, the longitudinal mode is stabilized to a single mode as the light output is increased. The longitudinal mode stabilization occurs at higher light outputs for the devices with smaller built-

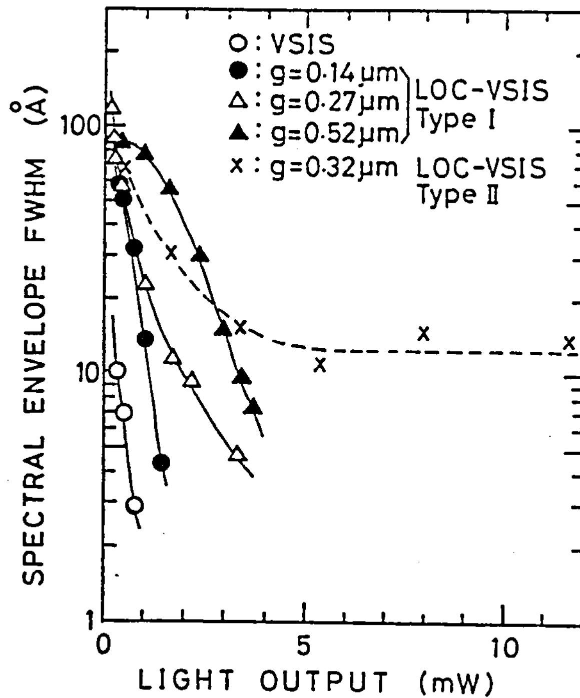

Fig.6 Spectral envelope width (FWHM) of VSIS and LOC-VSIS lasers as a function of light output power. Devices are listed in the order of smaller built-in refractive-index difference.

in refractive-index difference, as expected from the study in §3-3. The type II LOC-VSIS laser, which has the smallest refractive-index difference, stably operates on multimodes like conventional gain-guided lasers.[1,19,20] These results demonstrate that the longitudinal mode gradually varies from a single mode to multimodes, as the built-in refractive-index difference is decreased.

The intensity of intrinsic spectral noise as a function of dc current, shown in Fig.7 supports the longitudinal mode behaviors mentioned above. In the single mode devices, that is, regular VSIS lasers and type I LOC-VSIS lasers, two noise peaks appear at and slightly above the threshold as described in §3-3. In particular, the second noise peak slightly above the threshold is due to the mode competition which occurs just prior to gain suppression in nonlasing resonant modes, and it appears at higher light outputs in the devices with smaller built-in refractive-index difference. This tendencey accords with the longitudinal mode characteristics shown in Fig.6; gain suppression occurs at higher light outputs in the devices with smaller built-in refractive-index difference. The second noise peak does not appear in the type II LOC device, since it operates on multimodes and thus gain suppression does not occur in it. In addtion, in the type II LOC-VSIS laser, the noise power increases above the first noise peak, although no kink in the light output-current curve and no deformation of the far-field pattern with increasing the light output were observed in this device. This behavior is much different from conventional gain-guided lasers reported so far, in which the total noise power takes clear muximum around the threshold due to the quantum shot noise and then decreases.[1,21,22] The cause of this difference is not clear at present. It should be noted, however, that two major structural factors listed below are different in the present type II LOC-VSIS laser from those in conventional gain-guided lasers: (1) Asymmetric four-layer slab waveguide structure: (2) There is a possibility that the small built-in refractive-index difference may still remain in the present device.

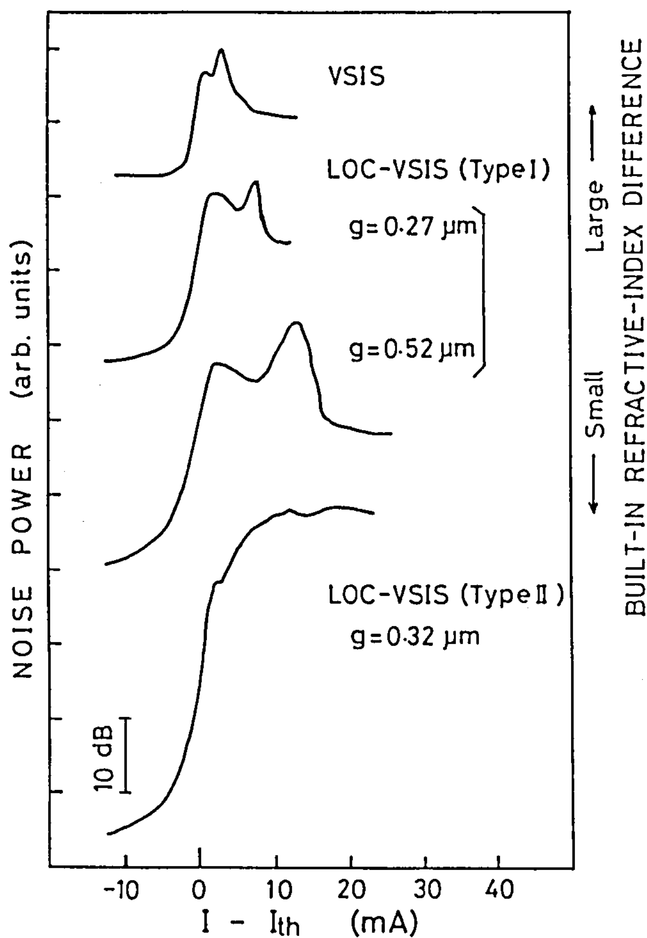

Fig. 7 Noise-power-versus-current characteristics of different types of devices. Noise power was measured at 100 MHz with a bandwidth of 30 kHz.

The temperature dependence of the far-field pattern was measured at an output power of 5 mW/facet. In the regular VSIS laser and the type I LOC-VSIS lasers with g=0.14 and 0.27 μm, the far-field pattern, which indicates the fundamental transverse mode, does not change with temperature in the measured temperature range of -100-60°C, as illustrated in Fig.8(a). By contrast, the far-field pattern gradually changes with temperature in the type II LOC-VSIS laser, as illustrated in Fig.8(b). At high temperatures (>-50°C), the width of the far-field pattern increases with decreasing temperature, and the far-field pattern splits into two peaks at low temperatures (<-50°C). This double-peaked far-field pattern indicates the first-order transverse mode in index-guided lasers or the "leaky" mode due to index antiguiding in the gain-guided lasers. The longitudinal-mode spectra of the type II LOC device measured at low temperatures below -50°C showed stable multimode oscillation with a single envelope. These spectra and the stable fundamental transverse mode at 20°C exclude the possibility of the first-order transverse-mode oscillation. Therefore, the double-peaked far-field pattern observed at low temperatures means the "leaky" mode in the gain-guided lasers with narrow current distribution as described in Refs.19, 20, 23, and 24 due to index antiguiding.[25] It was also observed that double peaks in the far-field pattern grew with increasing injection current as in the gain-guided lasers.[19,20,23,24] The change in the far-field pattern of the type II device results from narrowing of the current distribution with decreasing temperature, which would arise from the change in the resistivity of the Al-rich p-cladding layer.

The FWHM of the far-field pattern as a function of temperature is plotted in Fig.9 for the type I LOC-VSIS laser with g=0.27 and 0.52 μm and the type II LOC-VSIS laser. In the case of the type I LOC-VSIS laser with g=0.27 μm, the FWHM of the far-field pattern does not change with temperature; thus, the transverse mode is completely determined by built-in refractive-index difference. By contrast, in the type II LOC-VSIS laser, the FWHM of the far-

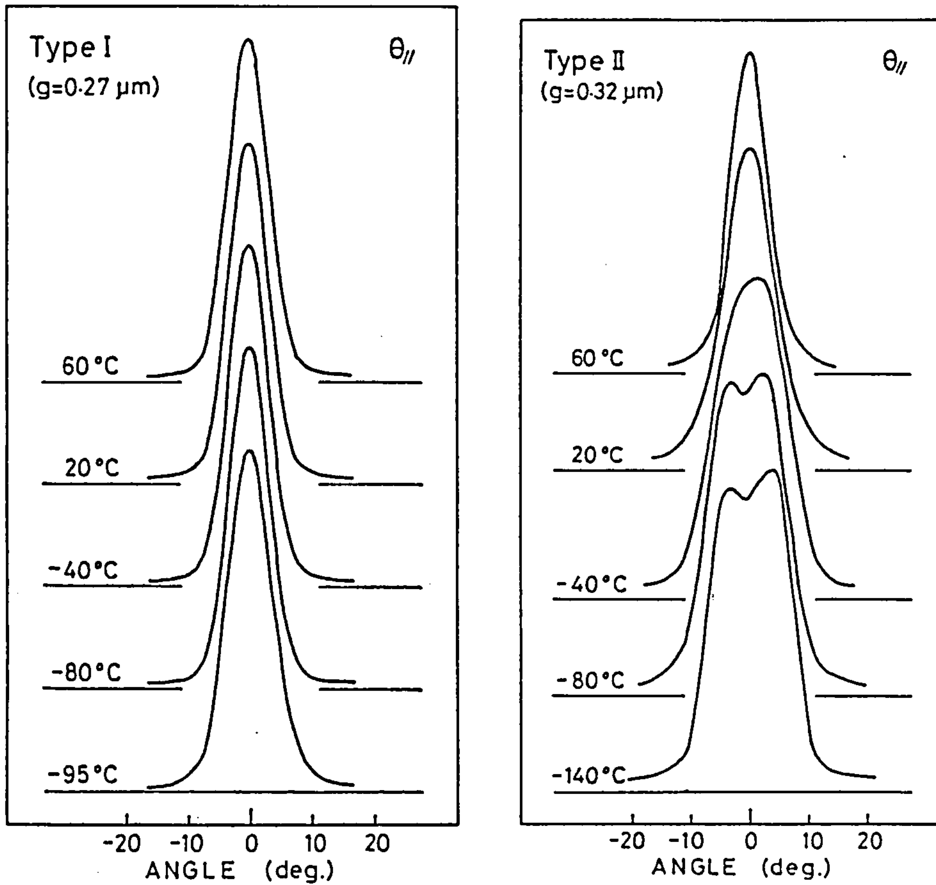

Fig. 8 Temperature dependence of the lateral far-field pattern of (a) the type I LOC-VSIS lasers with g=0.27 μm and (b) the type II LOC-VSIS laser.

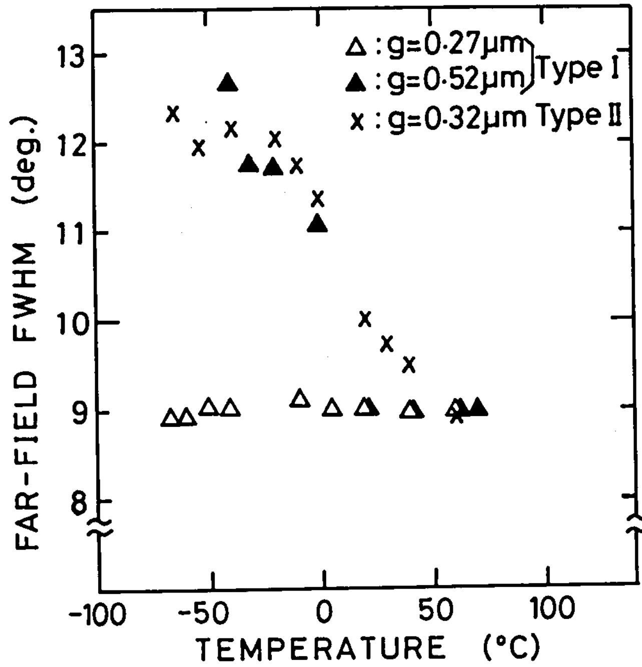

Fig.9 FWHM of the lateral far-field pattern as a function of temperature.

field pattern rapidly increases with decreasing temperature until the far-field pattern splits into two peaks, and then it increases slowly. In this case, the transverse mode is determined by the current distribution parallel to the junction plane. To put the above-mentioned results in another way, the former corresponds to index guiding and the latter corresponds to gain guiding. The most interesting case is the type I LOC-VSIS laser with g=0.52 μm, in which the built-in refractive-index difference is intermediate between those in the above two types of devices. In this case, as the temperature is decreased, the far-field pattern does not change at high temperatures (>∿10°C), suddenly broadens at ∿10°C, and splits into two peaks at low temperatures (<∿-20°C). This result indicates that the waveguiding mechanism changes from index guiding to gain guiding at ∿10°C with decreasing temperature, which means that there exists a rather clear boundary between these two waveguiding mechanisms. In addition, the multimode spectrum with a single envelope was obtained below -50°C, which confirms stable gain guiding at low temperatures.

The "leaky" mode observed in the type I LOC device with g=0.52 μm and type II LOC device at low temperatures results from the index antiguiding due to the charge-induced bulk index depression,[25)] and thus depends on the current distribution along the junction plane. This effect has been closely studied on proton-implanted stripe-geometry lasers as a function of stripewidth by Scifres et al.[21)] They demonstrated that the FWHM of the far-field pattern broadens and splits into two peaks as the stripewidth is decreased. However, Streifer et al. showed by the calculation that the charge-induced bulk index depression did not so strongly affect the transverse mode behavior in index-guided lasers[26,27)] as in gain-guided lasers.[25)] In fact, the type I LOC-VSIS laser with g=0.27 μm, which has the smaller built-in refractive-index difference than the regular VSIS laser, still exhibited stable fundamental transverse mode with changing temperature, whereas the same temperature variation strongly affects the transverse mode of type II LOC device, which is gain guided, as

shown in Figs. 8 and 9. The charge-induced index depression may disturb index guiding and enhance gain guiding when the built-in refractive-index difference is so small as the decrease in the real refractive index by the charge injection. The present results, especially the far-field variation of type I LOC device with g=0.52 μm shown in Fig.9, indicate that the mixture of index guiding and gain guiding does not exist in the wide range of device parameters, such as the magnitude of the built-in refractive-index difference and the current distribution. Only the rather anomalous variation of the spectral envelope FWHM and the intrinsic spectral noise with the light output of the type I LOC device with g=0.52 μm, which are shown in Figs.6 and 7 respectively, may represent the mixing effect since the temperature (20°C) where these measurements were carried out is in the vicinity of the transient region (∿10°C) of the temperature variation of the far-field pattern. It is considered to be usual that gain guiding and index guiding do not mix each other; the charge-induced index depression acts as a perturbation in index-guided lasers and so does the built-in refractive-index difference in gain-guided lasers.

Chen and Wang have been carried out the experiments similar to the present study;[28] they varied the magnitude of the built-in refractive-index difference in the double-current-confinement channeled-substrate planar (DCC-CSP) laser[31] by changing the thickness t of the first cladding layer which is sandwiched by the active layer and the substrate. They claimed that the distance D from the facet to the virtual beam waist increases with t and thus the waveguiding mechanism gradually varies from index guiding to gain guiding, which seems to be inconsistent with the present results. Their DCC-CSP lasers are, however, different from the present VSIS laser in dimensions and some basic characteristics, which would lead to somewhat different results. The smallest t= 0.33 μm in DCC-CSP lasers is still rather large and therefore, the built-in refractive-index difference is very small ($\sim 10^{-3}$).[29] This feature resulted in a wide beam width (FWHM∿2.5 μm) and a large astigmatism (D=9 μm) although its channel width was as nar-

row as 2 μm.[29,30] In the regular VSIS laser, which has a 4 μm wide channel and t=0.15 μm, the beam width is narrow (FWHM∿2 μm) and the astigmatism is small (D<3 μm). Astigmatism is also small in the type I LOC device with g=0.27 μm. The very small channel width (2 μm) in DCC-CSP lasers than the diffusion length of carriers (∿3 μm) would provide a fairly uniform carrier distribution in the channeled region.[30] By contrast, the rather wide channel width (4 μm) in VSIS lasers makes the sharp gain variation in the channeled region especially at low temperatures. It is also suggested from the unchanged beam width (FWHM∿3 μm) and the beam waist position (D∿11 μm) with varying the injection current from $1.1\times I_{th}$ to $3\times I_{th}$[28] that the "built-in loss" acts more effectively in DCC-CSP lasers than VSIS lasers. In addition, it should be noted that the DCC-CSP laser with t∿0.5 μm operated on a single longitudinal mode[29] although astigmatism of the DCC-CSP laser with similar dimension (t=0.55 μm) is very large (d=23 μm),[28,30] which is unexpected from the simple calculation.[31]

In contrast to the fairly abrupt change in the transverse mode, the longitudinal mode characteristics vary rather gradually with the change of built-in refractive-index difference in LOC-VSIS lasers. The results shown in Fig.6 suggest that at high light outputs, index-guided lasers tend to oscillate on a single mode and gain-guided lasers tend to oscillate on multimodes, which is consistent with the general trend reported so far.[31]

5-4. Summary

Dependence of mode characteristics upon the built-in refractive-index difference in VSIS and LOC-VSIS lasers has been studied. These devices belong to the weakly index-guided lasers with a narrow current distribution in the direction parallel to the junction plane.

Temperature dependence of the far-field pattern has indicated that when the temperature is decreased, the waveguiding mechanism which determines the transverse mode abruptly changes from index guiding to gain guiding in the device with the second smallest built-in refractive-index difference among all the devices employed in this study. In the device with the smallest built-in refractive-index difference, the transverse mode is determined by the lateral current distribution at all temperatures; thus gain guiding. In the other devices which have larger built-in refractive-index difference than above two devices, the transverse mode is determined by the built-in refractive-index difference and it does not change with temperature; thus index guiding. These results indicate that the waveguiding mechanism can be clearly classified into index guiding and gain guiding and the mixture of these mechanisms does not occur in the wide range of device parameters.

With regard to the longitudinal mode characteristics, index-guided lasers oscillate on a single mode and gain-guided lasers oscillate on multimodes at high light outputs. In the case of index-guidied lasers, however, the mode stabilization on a single mode occurs at higher light outputs in the lasers with smaller built-in refractive-index difference. This observation is supported by the variation of the intrinsic spectral noise with the light output.

References

1) K.Peterman and G.Arnold, IEEE J. Quantum Electron. QE-18, 543 (1982).
2) K.Peterman, Proc. 7th Eur. Conf. Opt. Commun. 10.1-1 (1981).
3) G.Arnold, Proc. 7th Eur. Conf. Opt. Commun. 10.4-1 (1981).
4) R.O.Miles, A.Dandridge, A.B.Tveten, T.Giallorenzi, and H.F. Taylor, Appl. Phys, Lett. 38, 848 (1981).

5) H.F.Lockwood, H.Kressel, H.S.Sommers, Jr., and F.Z.Hawrylo, Appl. Phys. Lett. 17, 499 (1970).

6) R.D.Burnham, D.R.Scifres, W.Streifer, and S.Peled, Appl. Phys. Lett. 35, 734 (1979).

7) D.Botez, Appl. Phys. Lett. 36, 190 (1980).

8) J.K.Butler and D.Botez, IEEE J. Quantum Electron. QE-18, 952 (1982).

9) H.C.Casey Jr., D.D.Sell, and M.B.Panish, Appl. Phys. Lett. 24 63 (1974).

10) T.Kuroda, M.Nakamura, K.Aiki, and J.Umeda, Appl. Opt. 17, 3264 (1978).

11) K.Aiki, M.Nakamura, T.Kuroda, R.Ito, N.Chinone, and M.Maeda, IEEE J. Quantum Electron. QE-14, 89 (1978).

12) H.Ishikawa, K.Hanamitsu, N.Takagi, T.Fujiwara, and M. Takusagawa, IEEE J. Quantum Electron. QE-17, 1226 (1981).

13) R.D.Burnham and D.R.Scifres, Appl. Phys. Lett. 27, 510 (1975).

14) P.A.Kirby and G.H.Thompson, J. Appl. Phys. 47, 4578 (1976).

15) K.Saito and R.Ito, IEEE J. Quantum Electron. QE-16, 205 (1980).

16) K.Shima, K.Hanamitsu, and M.Takusagawa, IEEE J. Quantum Electron. QE-18, 1688 (1982).

17) L.Figueroa and S.Wang, Appl. Phys. Lett. 31, 45 (1977).

18) C.Y.Chen and S.Wang, J. Appl. Phys. 52, 614 (1981).

19) D.R.Scifres, W.Streifer, and R.D.Burnham, IEEE J. Quantum Electron. QE-17, 2310 (1981).

20) T.Kobayashi, H.Kawaguchi, and Y.Furukawa, Jpn. J. Appl. Phys. 16, 601 (1977).

21) T.L.Paoli, IEEE J. Quantum Electron. QE-11, 276 (1975).

22) T.Ito, S.Machida, K.Kawata, and T.Ikegami, IEEE J. Quantum Electron. QE-13, 574 (1977).

23) P.M.Asbeck, D.A.Cammack, J.J.Daniele, and V.Klebanoff, IEEE J. Quantum Electron. QE-15, 727 (1979).

24) C.Wolk, H.Gottsmann, P.Marschall, K.Petermann, W.Pfrister, and H.-P.Vollmer, IEEE J. Quantum Electron. QE-17, 756 (1979).

25) W.Streifer, R.D.Burnham, and D.R.Scifres, IEEE J. Quantum Electron. QE-18, 856 (1982).

26) W.Streifer, R.D.Burnham, and D.R.Scifres, IEEE J. Quantum Electron. QE-17, 736 (1981).

27) W.Streifer, D.R.Scifres, and R.D.Burnham, IEEE J. Quantum Electron. QE-17, 1521 (1981).

28) C.Y.Chen and S.Wang, Appl. Phys. Lett. 37, 257 (1980).

29) C.Y.Chen and S.Wang, Appl. Phys. Lett. 36, 634 (1980).

30) S.Wang, C.Y.Chen, A.S.H.Liao, and L.Figueroa, IEEE J. Quantum Electron. QE-17, 453 (1981).

31) W.Streifer, D.R.Scifres, and R.D.Burnham, Appl. Phys. Lett. 40, 305 (1982).

VI. CONCLUSION

In this thesis, studies have been carried out on the fundamental properties, reliability and mode characteristics of (GaAl)As stripe-geometry DH lasers emitting in the visible wavelength region. With the aid of many characterizations, the structure and fabrication procedure of devices have been improved and highly reliable and mode-stabilized visible semiconductor lasers have been realized. Variation of fundamental properties with the emission wavelength and controllability of mode characteristics in these devices have been studied.

In Chapter II, long-term reliability and degradation phenomena depending on the emission wavelength and the operating ambient have been studied by using conventional oxide-defined stripe-geometry DH lasers. The degradation mechanisms are classified into two mechanisms; that is, the dark defects formation in the vicinity of the mirror facet ($\gtrsim$820 nm) and the facet oxidation ($\lesssim$820 nm). The facet oxidation, which proceeds faster with shortening the wavelength, has been examined in detail with a scanning Auger electron microscope, and it is effectively suppressed with Al_2O_3 facet coatings. It is also shown that the degradation due to the facet oxidation is affected by the humidity of the operating ambient. The reaction of In solder with GaAs crystal is eliminated by using Mo as a barrier metal, and the intermetallics formation between In solder and Au electrode during the aging test, which results in the increase in the thermal resistance, is minimized by reducing the amount of Au evaporated on Mo. As a result of these improvements, long-term stable operation has been realized in infrared lasers: the mean time to failure at 25°C is estimated to be 1.9×10^6 h.

In Chapter III, the VSIS lasers on p-GaAs substrates emitting in the visible spectrum range have been developed. In consequence of the simple structure that has a built-in optical waveguide self-aligned with an internal current confining channel, VSIS lasers

reproducibly provide a stable fundamental transverse and single longitudinal mode operation up to 20 mW/facet cw. The threshold current is in the range of 40±5 mA. In the VSIS laser, lasing starts on multimodes and stabilizes to a single longitudinal mode with increasing current more than a few percent above the threshold. Thus the intrinsic spectral noise intensity shows two peaks at and slightly above the threshold. These characteristics are considered to result from the unique structure of the VSIS laser with small built-in refractive-index difference and narrow current distribution along the junction plane. Tellurium in the n-type cladding layer is found to have the effect of lowering the reliability of conventional oxide-defined stripe-geometry lasers, in which the active layer is grown on top of the Te-doped cladding layer. This deleterious effect of the Te-doped cladding layer on the quality of the active layer is eliminated by the reverse growth sequence of the active and Te-doped cladding layers using p-type GaAs as a substrate for the first time. Accelerated life tests and the statistical characterization of the reliability have been performed on the lasers emitting at 780 nm. From these results, the median lifetime has been estimated to be 1.1×10^{6} h for 5 mW/facet, 4.8×10^{4} h for 10 mW/facet, and 1.3×10^{4} h for 15 mW/facet operations at 25°C. Photoluminescence study on DH layers has revealed that the Te-doped cladding layer "under" the active layer impairs the quality of the active layer and that the quality of the active layer is improved when it is grown upon a p-type cladding layer followed by the growth of the Te-doped cladding layer "on" the active layer.

In Chapter IV, fundamental properties of VSIS lasers emitting below 750 nm have been studied. The low threshold currents of VSIS lasers below 750 nm are presented. The threshold current of a device emitting at 690 nm is as low as 100 mA. The variation of the threshold current of these devices with the lasing wavelength agrees with the variation of the inverse of internal quantum efficiency calculated using the energy band parameters where the indirect-direct crossover is assigned at the AlAs mole fraction of 0.45. cw operation has been obtained at as short as 688 nm. The

cause of the increase in the threshold current of conventional lasers on n-type substrate is examined based on the results of photoluminescence, Al-profile in the active layer, and the device structure. It is considered that the increase in the threshold current arises from the excess loss and/or the decrease in the gain peak intensity caused by the Te-doped cladding layer "under" the active layer. These faults can be improved by reducing the Te concentration in the n-type cladding layer. However, the reduction in the Te concentration is the tradeoff of increasing the lateral current spreading in many types of conventional laser structures fabricated on n-type substrates. In the VSIS laser, since the highly conductive Te-doped cladding layer is grown "on top of" the active layer, it does not impair the laser properties and reduces the lateral current spreading. The temperature dependence of the threshold current has been measured for devices with emission wavelengths of 781-697 nm. The threshold-temperature coefficient defined as $I_{th}(350\ K)/I_{th}(300\ K)$ is found to increase below 750 nm with decreasing the lasing wavelength in spite of the fairly large difference in the AlAs mole fraction Δx of 0.4 between the active and cladding layers. This tendencey is well explained by the model of carrier leakage due to unconfined carriers in the active layer, and is inherent in the indirect band-gap (GaAl)As cladding layer used in the short wavelength visible lasers. In order to improve the reliability of lasers emitting below 750 nm, the stress in the active layer has been reduced. It has been shown by the calculation that the active layer stress caused by the bonding process can be reduced by setting the thicknesses of the cap layer and the substrate at appropriate values. The life test of VSIS lasers emitting at 740 nm under the constant light output condition of 5 mW/facet at 50°C have demonstrated that the lifetime is considerably improved by the introduction of the thick cap layer ($\sim$40 μm) and the thinned substrate ($\sim$80 μm). The improved lifetime is expected to be more than several thousand hours at 50°C.

In Chapter V, dependence of mode characteristics on the built-in refractive-index difference has been studied for VSIS lasers

emitting at 780 nm by the introduction of a large-optical-cavity structure. Temperature dependence of the far-field pattern indicates that the waveguiding mechanism can be clearly classified into index guiding and gain guiding. At high outputs, index-guided devices operate on a single longitudinal mode and gain-guided devices operate on multimodes. In the index-guided lasers, the mode stabilization occurs at higher light outputs in the lasers with the smaller built-in refractive-index difference.

LIST OF PUBLICATION

I. Full Papers

1) "Facet Degradations in $Ga_{1-x}Al_xAs/Ga_{1-y}Al_yAs$ Double-Heterostructure Lasers," T.Hayakawa, S.Yamamoto, T.Sakurai, and T.Hijikata, J. Appl. Phys. 52, 6068 (1981).

2) "Temperature Dependence of Threshold Current in (GaAl)As Double-Heterostructure Lasers with Emission Wavelengths of 0.74-0.9 μm," T.Hayakawa, S.Yamamoto, H.Hayashi, T.Sakurai, and T.Hijikata, IEEE J. Quantum Electron. QE-17, 2205 (1981).

3) "Long-Lived (GaAl)As DH Lasers Bonded with In Produced by Eliminating Deterioration of In Solder," T.Hayakawa, S.Yamamoto, S.Matsui, T.Sakurai, and T.Hijikata, Jpn. J. Appl. Phys. 21, 725 (1982).

4) "Highly Reliable and Mode-Stabilized Operation in V-Channeled Substrate Inner Stripe Lasers on p-GaAs Substrate Emitting in the Visible Wavelength Region," T.Hayakawa, N.Miyauchi, S.Yamamoto, H.Hayashi, S.Yano, and T.Hijikata, J. Appl. Phys. 53, 7224 (1982).

5) "Low-Current-Threshold (GaAl)As Visible Lasers with Emission Wavelengths below 750 nm," T.Hayakawa, S.Yamamoto, H.Hayashi, N.Miyauchi, S.Yano, and T.Hijikata, J. Appl. Phys. 54, 2209 (1983).

6) "Threshold-Temperature Characteristics in (GaAl)As Visible Laser Diodes Emitting below 750 nm," T.Hayakawa, T.Suyama, S.Yamamoto, H.Hayashi, S.Yano, and T.Hijikata, J. Appl. Phys. 54, 2983 (1983).

7) "Mode Charcteristics of Large-Optical-Cavity V-Channeled Substrate Inner Stripe Injection Lasers," T.Hayakawa, T.Suyama, H.Hayashi, S.Yamamoto, S.Yano, and T.Hijikata,

IEEE J. Quantum Electron. QE-19, 1530 (1983).

II. Letters

1) "Multimode-Oscillating Behavior in Index-Guiding V-Channeled Subatrate Inner Stripe Lasers Depending on Structural Factor," T.Hayakawa, S.Yano, and T.Hijikata, Jpn. J. Appl. Phys. 21, L624 (1982).

2) "Improved Lifetimes of (GaAl)As Visible (740 nm) Lasers by Reducing Bonding Stress," T.Hayakawa, N.Miyauchi, S.Yamamoto, H.Hayashi, S.Yano, and T.Hijikata, Appl. Phys. Lett. 42, 23 (1983).

III. International Conference

1) "Highly Reliable and Mode-Stabilized (GaAl)As Double-Heterostructure Visible Lasers on p-GaAs substrate," T.Hayakawa, S.Yamamoto, H.Hayashi, N.Ohtsuka, K.Murata, J.Takagi, T.Sakurai, and T.Hijikata, International Electron Devices Meeting, Washington, D.C., U.S.A., December, 1981, 18.3.